UNIVERSITA' DEGLI STUDI DI MILANO
FACOLTA' DI SCIENZE MATEMATICHE, FISICHE E NATURALI
DOTTORATO DI RICERCA IN
FISICA, ASTROFISICA E FISICA APPLICATA

THE CALCULATION OF ATMOSPHERIC MUON FLUX USING THE FLUKA MONTE CARLO CODE

FIS/04 - Fisica Nucleare e Subnucleare

Coordinatore: Prof. Gianpaolo Bellini
Tutore: Dott. Giuseppe Battistoni

Tesi di Dottorato di:
Silvia Muraro
Ciclo XIX
Matr: R05674

Anno Accademico 2005-2006

Contents

Introduction

Reliable calculations of flux of secondary particles in atmosphere, produced by the interactions of primary cosmic rays, are essential for the correct interpretation of the large amount of experimental data produced by experiments in the field of astroparticle physics. The increasing accuracy of modern experiments demands also an improved quality of the calculation tools. The most important example in this field is the analysis of the experimental results on atmospheric neutrinos from Super-Kamiokande , which gave the first robust evidence in favor of neutrino oscillations.
Since muons are produced in the decay of the same mesons that are the source of neutrinos, the muon fluxes correlate directly to the hadronic interactions. Thus a reliable production of atmospheric muon spectra can also provide important information to improve accuracy of atmospheric neutrino calculations.
In order to improve the accuracy of the predictions, a detailed understanding of hadronic interactions, as well as precise information of primary cosmic-ray fluxes, is indispensable. A lot of parameters have to be taken into account as solar modulation effect on primary fluxes, atmospheric models, the Earth's magnetic field effect and others.
The FLUKA code is designed to make use of the best possible available models in respect to theory. Regarding hadronic physics, the so called "microscopic" models are used (i.e. those based on the physics of hadron constituents). These models, which usually have a limited number of parameters, are tuned using data only from experiments performed under well controlled conditions, as experiments at accelerators (particularly the thin target experiments). This is a strict requirement for the FLUKA development. For these reasons FLUKA is often quoted as an example of accurate simulation tool.
The aim of this thesis is to check the reliability of FLUKA to simulate the production of secondary particles by primary cosmic rays interacting with the Earth's atmosphere. This is a typical situation in which is not easy to have full control on every condition. In particular there is no mono-energetic beam, but an energy spectrum of uncertain composition and that spans many orders of magnitude in energy. For this purpose we have concentrated our efforts on the simulation of the production of atmospheric muons and its comparison with experimental data.
This permits not only to evaluate how reliable FLUKA is in "cosmic" interaction, but also to qualify the code for applications like space radiation calculations and for dosimetry in long duration flights in civil aviation.

In the first Section approximate analytic solutions for the flux of cosmic rays through the atmosphere are presented.
In the second Section is given a description of the experiments that detected muons (and protons and helium nuclei) that are used for the comparison with simulations.
The FLUKA Monte Carlo code is presented in the third Section with a detailed description of the cosmic rays package and of the "ingredients" used to accomplish the simulations shown in Section 4.
Section 4 contains simulations and comparisons with different sets of experimental data, taking into account different atmospheric models and primary spectra. Simulations and comparisons are also performed, using two interaction models, at small atmospheric depths with data from a balloon flight. For energies up to 2 TeV another simulation and comparison is accomplished for different zenith angle bins, showing a good agreement with experimental data.

1 Cosmic rays fluxes in the Earth's atmosphere

1.1 Primary spectra

The cosmic radiation incident at the top of the terrestrial atmosphere includes all stable charged particles and nuclei with lifetimes of order 10^6 years or longer. *Primary* cosmic rays are those particles accelerated by astrophysical sources and *secondaries* are those particles produced in interaction of the primaries with interstellar gas. Thus electrons, protons and helium, as well as carbon, oxygen, iron, and other nuclei synthesized in stars, are primaries. Nuclei such as lithium, beryllium, and boron (which are not abundant end-products of stellar nucleosynthesis) are secondaries. Antiprotons and positrons are also in large part secondary, whether a small fraction of these particles may be primary is a question of current interest.
Apart from particles associated with solar flares, the cosmic radiation mostly comes from outside the solar system. The incoming charged particles are "modulated" by the solar wind, the expanding magnetized plasma generated by the Sun, which decelerates and partially excludes the lower energy galactic cosmic rays from the inner solar system. There is a significant anticorrelation between solar activity (which has an eleven-year cycle) and the intensity of the cosmic rays with energies below about 10 GeV. In addition, the lower-energy cosmic rays are affected by the geomagnetic field, which they must penetrate to reach the top of the atmosphere. Thus the intensity of any component of the cosmic radiation in the GeV range depends both on the location and time. There are different ways to describe the spectra of the components of the cosmic radiation:

(1) By particles per unit rigidity. Propagation (and probably also acceleration) through cosmic magnetic fields depends on *magnetic rigidity, R*:

$$R = \frac{pc}{Ze} = r_L B. \tag{1}$$

(2) By particles per energy-per-nucleon. Fragmentation of nuclei propagating through the interstellar gas can be safely described in terms of energy per nucleon, since that quantity is approximately conserved when a nucleus breaks up on interaction with the gas.

(3) By nucleons per energy-per-nucleon. Production of secondary cosmic rays in the atmosphere depends on the intensity of nucleons per energy-

per-nucleon, approximately independently of whether the incident nucleons are free protons or bound in nuclei.

(4) By particles per energy-per-nucleus. Air shower experiments that use the atmosphere as a calorimeter generally measure a quantity that is related to total energy per particle.

The units of differential intensity I for the four different choice are: $[cm^{-2}s^{-1}sr^{-1}\varepsilon^{-1}]$, where ε represents the units of one of the four variables listed above.
Choosing the nucleons per energy per nucleon representation, the intensity of primary nucleons in the wide energy range from several GeV to somewhat beyond 100 TeV is given approximately by

$$I_N(E) \approx 1.8E^{\alpha}\frac{nucleons}{cm^2\ s\ sr\ GeV} \tag{2}$$

where E is the energy-per-nucleon (including rest mass energy) and α is related to the integral spectral index γ by $\alpha(\equiv \gamma + 1) = 2.7$. About 79% of the primary nucleons are free protons and about 70% of the remaining part are nucleons bound in helium nuclei. The fractions of the primary nuclei are nearly constant over this energy range (possibly with small but interesting variations). Fractions of both primary and secondary incident nuclei are listed in Table 1 and Fig. 1 [13] shows the major components as a function of energy at a particular epoch of the solar cycle.
Up to energies of at least 10^{15} eV, the composition and energy spectra of nuclei are typically interpreted in the context of "diffusion" or "leaky box" models, in which the sources of the primary cosmic radiation are located within the galaxy [21]. The ratio of secondary to primary nuclei is observed to decrease approximately as $E^{-0.5}$ with increasing energy, showing that the lifetime of cosmic rays in the galaxy decreases with energy.

1.2 Cosmic rays in the atmosphere

Fig.2 shows the vertical fluxes of the major cosmic ray components in the atmosphere in the energy region where the particles are most numerous (except for electrons, which are most numerous near their critical energy, which is about 81 MeV in air). Except for protons and electrons near the top of the atmosphere, all particles are produced in interactions of the primary cosmic rays in the air. Muons and neutrinos are produced by the decay of charged mesons, while electrons and photons originate in decays of neutral mesons.

Z	*Element*	*F*
1	H	540
2	He	26
3-5	Li-B	0.40
6-8	C-O	2.20
9-10	F-Ne	0.30
11-12	Na-Mg	0.22
13-14	Al-Si	0.19
15-16	P-S	0.03
17-18	Cl-Ar	0.01
19-20	K-Ca	0.02
21-25	Sc-Mn	0.05
26-28	Fe-Ni	0.12

Table 1: Relative abundances F of cosmic-ray nuclei at 10.6 GeV/nucleon normalized to oxygen ($\equiv 1$) [20]. The oxygen flux at kinetic energy of 10.6 GeV/nucleon is 3.26×10^{-6} cm^{-2} s^{-1} sr^{-1} (GeV/nucleon)$^{-1}$. Abundances of hydrogen and helium are from Ref. [17], [18].

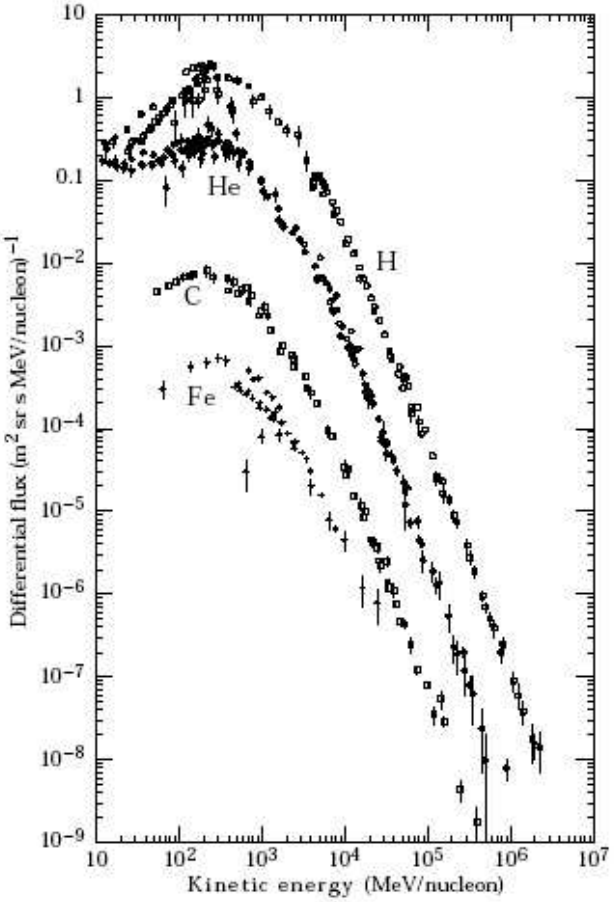

Figure 1: Major components of the primary cosmic radiation (from Ref. [13]).

Most measurements are made at ground level or near the top of the atmosphere, but there are also measurements of muons and electrons from airplanes and balloons.

The flux of cosmic rays through the atmosphere is described by a set of coupled cascade equations with boundary conditions at the top of the atmosphere to match the primary spectrum. Numerical or Monte Carlo calculations are needed to account accurately for decay processes,for energy-loss processes, and for the energy-dependences of the cross sections and of the primary spectral index γ. Approximate analytic solutions are, however, useful in limited regions of energy [1].

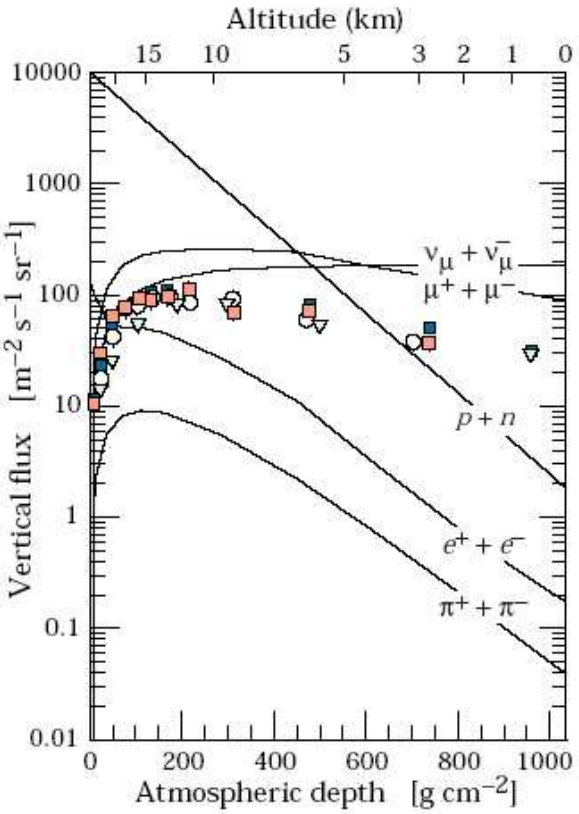

Figure 2: Vertical fluxes of cosmic rays in the atmosphere with E > 1 GeV estimated from the nucleon flux of Eq. 2. The points show measurements of negative muons with E > 1 GeV [16], [36]-[38].

The atmosphere

The Earth's atmosphere is an extremely thin sheet of air extending from the surface of the Earth to the edge of space, about 1000 km above the surface of the Earth. Within the atmosphere, very complex chemical, thermodynamic, and fluid dynamics effects occur. The atmosphere is not uniform; fluid properties are constantly changing with time and place.
Variations in air properties extend upward from the surface of the Earth. The Sun heats the surface of the Earth, and some of this heat goes into warming the air near the surface. The heated air is then diffused or convected up through the atmosphere. Thus the air temperature is highest near the surface and decreases as altitude increases. The speed of sound depends on the temperature and also

decreases with increasing altitude. The pressure of the air can be related to the weight of the air over a given location.
Air pressure decreases as we increase altitude. The air density depends on both the temperature and the pressure and also decreases with increasing altitude. The major species in the upper atmosphere are N_2, O, O_2, H, He. According to temperature variation we can differentiate the strata of the atmosphere as follows:
the troposphere (from the surface of the Earth up to ∼12 km), where the temperature decreases,
the stratosphere (from ∼12 km up to ∼45 km), where the temperature increases,
the mesosphere (from ∼45 km up to ∼95 km), where the temperature decreases again,
the thermosphere (from ∼95 km up to ∼400 km), where the temperature decreases again,
and the exosphere (above ∼400 km), where the temperature is constant.

For these calculations, we'll take into account an approximate atmospheric model.
The relation between altitude and depth in atmosphere is shown in Fig. 3.

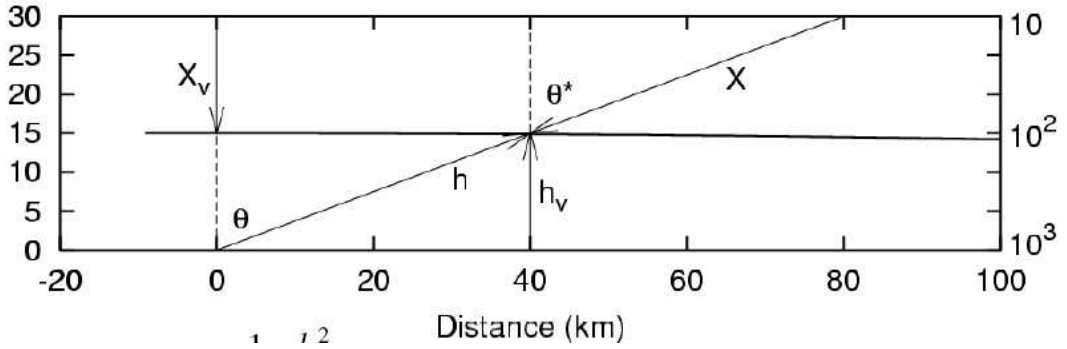

Figure 3: Definition of variables to describe the atmosphere.

The pressure at vertical depth X_v in the atmosphere is $p = X_v$, and the density is $\rho = dX_v/dh_v$. Since specific volume is inversely proportional to density,

$$\frac{p}{\rho} = \frac{X_v}{dX_v/dh_v} \propto T. \tag{3}$$

So for an isothermal atmosphere, the ratio in Eq. 3 is equal to a constant scale height, h_0. Then

$$X_v = X_0 e^{-h_v/h_0}, \tag{4}$$

where $X_0 \cong 1030$ g/cm^2.
The temperature and hence the scale height decrease with increasing altitude until the tropopause (12-16 km). At sea level $h_0 \cong 8.4$ km, and for $X_v < 200$ g/cm^2, $h_0 \cong 6.4$ km.
In general, the relation between vertical altitude (h_v) and distance up the trajectory (h) (for $h/R_\oplus \ll 1$) is expressed by

$$h_v \cong \cos\theta + \frac{1}{2}\frac{h^2}{R_\oplus}\sin^2\theta, \tag{5}$$

where $R_\oplus$ is the radius of the Earth. For zenith angle $\theta < 60^\circ - 70^\circ$ we have

$$h_v \cong h\cos\theta \quad (\theta < 60^\circ - 70^\circ). \tag{6}$$

The corresponding "slant depth" is given by

$$X = \int_{h=h_v/\cos\theta}^{\infty} \rho(l)dl. \tag{7}$$

1.2.1 Nucleon flux in the atmosphere: a simple approach

Propagation of particles through the atmosphere can be described analytically by transport or cascade equations depending both on the properties of the particles and their interactions and on the structure of the atmosphere. Since nucleons are stable compared to their transit time through the atmosphere, they obey a particularly simple cascade equation.

For the sake of simplicity we present the one-dimensional version of this equation:

$$\frac{dN(E,X)}{dX} = -\frac{N(E,X)}{\lambda_N(E)} + \int_E^\infty \frac{N(E',X)}{\lambda_N(E')}F_{NN}(E',E)\frac{dE'}{E}. \tag{8}$$

Here $N(E,X)dE$ is the flux of nucleons (neutrons plus protons) with energies in the interval E to $E+dE$ at depth X in the atmosphere.
The nucleon interaction length in air is given by

$$\lambda_N(E) = \frac{Am_N}{\sigma_N^{Air}(E)}. \tag{9}$$

For a calculation of the atmospheric cascade we can take the target nucleus to be an average "air" nucleus with mass number $A \approx 14.5$. For $\sigma_N^{Air}(E) \sim 300mb$ (appropriate for nucleons interacting with air in the TeV range), $\lambda_N(E) \approx 80g/cm^2$.

The transport Eq. 8 for nucleons is only valid to the extent that production of nucleons by other types of particles (e.g. pions) can be neglected. In general, fluxes of particles in the atmosphere are governed by a set of coupled cascade equations.
We assume that incident nuclei of mass A and total energy E_0 can be treated as A independent nucleons each of energy $E = E_0/A$. This is called the "superposition approximation".
With this assumptions is possible to find *elementary solutions* in which the dependence on energy and depth factorizes:

$$N(E, X) = A(X)E^{-\gamma}. \tag{10}$$

With the substitution in Eq. 8 of the factorized form Eq. 10 we get

$$\begin{aligned} \frac{dA(X)}{dX}E^{-\gamma} &= -\frac{A(X)E^{-\gamma}}{\lambda_N(E)} + \int_E^\infty \frac{N(A(X)E'^{-\gamma}}{\lambda_N(E')}F_{NN}(E', E)\frac{dE'}{E} = \\ &= -\frac{A(X)E^{-\gamma}}{\lambda_N(E)}\left(1 - \int_E^\infty \left(\frac{E'}{E}\right)^{-\gamma} F_{NN}(E', E)\frac{dE'}{E}\right). \end{aligned} \tag{11}$$

If the function $F_{ij}(E_i, E_j)$ is the dimensionless inclusive cross section for an incident particle i of energy E_i to collide with an air nucleus and produce an outgoing particle j of energy E_j, in general we define

$$F_{ij}(E_i, E_j) = E_j\frac{dn_j(E_i, E_j)}{dE_j}, \tag{12}$$

where dn_j is the number of particle of type j produced on average in the energy bin dE_j per collision of an incident particle of type i.
For high energy interactions, the Feynman scaling hypothesis [1] states that $F_{ij}(E_i, E_j)$ can be expressed with a single variable $\xi = \frac{E_j}{E_i}$.
So, we can write $\int \ldots F(E_i, E_j)\frac{dE_j}{E_i} \to \int \ldots F(\xi)\frac{d\xi}{\xi^2}$.

With the introduction of the exact Feynman scaling hypothesis into Eq. 11

we get

$$\begin{aligned}\frac{dA(X)}{dX}E^{-\gamma} &= -\frac{A(X)E^{-\gamma}}{\lambda_N}\Big(1-\int_0^1\Big(\xi\Big)^{\gamma}F_{NN}(\xi)\frac{d\xi}{\xi^2}\Big) = \\ &= -\frac{A(X)E^{-\gamma}}{\lambda_N}\Big(1-\int_0^1\Big(\xi\Big)^{\gamma}\xi\frac{dn}{d\xi}\frac{d\xi}{\xi^2}\Big) = \\ &= -A(X)E^{-\gamma}\frac{1}{\lambda_N}\Big(1-\int_0^1\Big(\xi\Big)^{\gamma-1}\frac{dn}{d\xi}d\xi\Big) = \\ &= -A(X)E^{-\gamma}\frac{1}{\lambda_N}\Big(1-Z_{NN}\Big), \end{aligned} \tag{13}$$

where Z_{NN} is called the "spectrum weighted moment" and determines the uncorrelated fluxes of energetic particles in the atmosphere.

The "effective attenuation length" Λ_N is related to the spectrum weighted moment by

$$\frac{1}{\lambda_N}\Big(1-Z_{NN}\Big) = \Lambda_N. \tag{14}$$

Thus, the solution of the differential Eq. 13 is given by:

$$N(E,X) = A_0 e^{-\frac{X}{\Lambda}}E^{-\gamma}. \tag{15}$$

1.2.2 Coupled cascade equations: π flux

Since all types of hadrons can be produced when an energetic hadron interacts, a set of coupled transport equations is needed to describe hadron fluxes in the atmosphere in full detail.
In practice, the simplest way to handle a detailed treatment of particle fluxes is mainly a Monte Carlo simulation or a numerical integration of the transport equations. A study of analytic solutions is useful for qualitatively understanding and checking the numerical results. For this purpose, it is sufficient to neglect nucleon-antinucleon production as well as the coupling to other channels, and look at the pion-nucleon sector.
With the initial condition of $\Pi(X=0,E)=0$, we have

$$\left\{\begin{array}{rcll} \frac{dN(E,X)}{dX} &=& -\frac{N(E,X)}{\lambda_N} & + \int_0^1 \frac{N(\frac{E}{\xi})}{\lambda_N}F_{NN}(E_N,\frac{E}{\xi})\frac{d\xi}{\xi^2} \\ \frac{d\Pi(E,X)}{dX} &=& -\Big(\frac{1}{\lambda_\pi}+\frac{1}{d_\pi}\Big)\Pi & + \int_0^1 \frac{\Pi(\frac{E}{\xi})}{\lambda_\pi}F_{\pi\pi}(E_\pi,\frac{E_\pi}{\xi})\frac{d\xi}{\xi^2} \\ & & & + \int_0^1 \frac{N(\frac{E}{\xi})}{\lambda_N}F_{N\pi}(E_\pi,\frac{E_\pi}{\xi})\frac{d\xi}{\xi^2}. \end{array}\right.$$

Particle	$c\tau_0$ (cm)	ε (GeV)
$\mu^{\pm}$	6.59 10^4	1.0
$\pi^{\pm}$	780	115
π^0	2.5 10^{-6}	3.5 10^{10}
$K^{\pm}$	371	850
K_S	2.68	1.2 10^6
K_L	1554	205
$D^{\pm}$	0.028	4.3 10^7
D^0	0.013	9.2 10^7

Table 2: Decay constants.

(16)

The decay term is

$$d_\pi = \rho\gamma c\tau_\pi, \tag{17}$$

where ρ is the atmospheric density. So

$$d_\pi = \rho\gamma c\tau_\pi = \frac{Xcos\theta}{h_0}\gamma c\tau_\pi = \frac{Xcos\theta}{h_0}\frac{E}{m_\pi c^2}c\tau_\pi = \frac{EXcos\theta}{\varepsilon_\pi}, \tag{18}$$

where $\frac{\cos\theta}{h_0}$ is the distance covered by the particle in the atmosphere, θ is the zenith angle and the *critical energy* $\varepsilon_\pi = \frac{m_\pi c h_0}{\tau_\pi}$ is the energy where both processes (interaction and decay process) have the same magnitude.
For $E < \varepsilon_\pi$ decay becomes important. Decay or interaction dominates depending respectively on whether $1/d_\pi$ or $1/\lambda_\pi$ is larger in Eq. 16. This in turn depends on the relative size of ε_π and E, and similarly for other particles. We summarize the decay constants for various particles in Table 2.

In the limit that $E \gg \varepsilon_\pi$, decay can be neglected. Then, the scaling limit solution of Eq. 16 is

$$\Pi(E, X) = A_0 E^{-\gamma}\frac{Z_{N\pi}}{1 - Z_{NN}}\frac{\Lambda_\pi}{\Lambda_\pi - \Lambda_N}\left(e^{-\frac{X}{\Lambda_\pi}} - e^{-\frac{X}{\Lambda_N}}\right). \tag{19}$$

The solution for charged kaons is the same as for charged pions with subscript π replaced by subscript K. Attenuation lengths in the 100 GeV range are tabulated in Table 3, based on the values of Z_{ij} and interactions lengths from

Λ_N (nucleons)	Λ_π (pions)	Λ_K (kaons)
120	160	180

Table 3: Atmospheric attenuation lengths (g/cm^2).

accelerator data. The pion flux shown in Fig. 2 and given by Eq. 19 rises from zero at the top of the atmosphere to a maximum value at a depth

$$X = \ln(\Lambda_\pi/\Lambda_N) \times (\Lambda_N\Lambda_\pi)/(\Lambda_\pi - \Lambda_N) \sim 140 g/cm^2.$$

In the low energy limit $Ecos\theta \ll \varepsilon_\pi$, where pion decay cannot be neglected, the transport equation for charged pions becomes

$$\Pi(E, X) = A_0 E^{-\gamma} \frac{Z_{N\pi}}{\lambda_N} e^{-\frac{X}{\Lambda_N}} \frac{X E cos\theta}{\varepsilon_\pi} \tag{20}$$

1.2.3 Muon and neutrino fluxes in the atmosphere

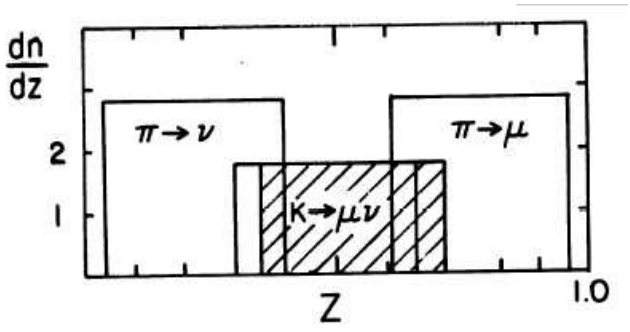

Figure 4: Decay distributions of π-decay and K-decay into $\mu\nu_\mu$ for 200 MeV/c parent mesons. z is the ratio of the total laboratory energy of the decay product to that of the parent.

The most important π and K decay channels and their branching ratios

are

$$\begin{aligned} \pi^{\pm} \to \mu^{\pm} + \nu_{\mu}(\bar{\nu}_{\mu}) \quad (\sim 100\%), \\ \pi^{0} \to 2\gamma \quad (\sim 98.8\%), \\ K^{\pm} \to \mu^{\pm} + \nu_{\mu}(\bar{\nu}_{\mu}) \quad (\sim 63.5\%). \end{aligned}$$

For the first and third process (two body decay $M \to \mu\nu$) and in case of relativistic mesons decay,

$$\frac{dn}{dE_{\nu}} = \frac{dn}{dE_{\mu}} = \frac{1}{1 - r_{\pi,K}} \frac{1}{E_{\pi,K}}, \tag{21}$$

where $r_{\pi,K} = \frac{m_{\mu}^2}{M_{\pi,K}^2}$ and m_{μ}, $M_{\pi,K}$ represent the respective particle masses. The kinematic limits on the laboratory energies of the secondaries are

$$E \frac{m_{\mu}^2}{M_{\pi,K}^2} \leq E_{\mu} \leq E \tag{22}$$

and

$$0 \leq E_{\nu} \leq \Big(1 - \frac{m_{\mu}^2}{M_{\pi,K}^2}\Big) E, \tag{23}$$

where E is the laboratory energy of the decaying meson. The energy fractions of the decay products from π and K decays ($\pi \to \mu\nu$ and $K \to \mu\nu$) are given respectively by

$$\begin{aligned} \frac{\langle E_{\mu} \rangle}{E_{\pi}} \sim 0.79 \quad \text{and} \quad \frac{\langle E_{\nu} \rangle}{E_{\pi}} \sim 0.21 \\ \frac{\langle E_{\mu} \rangle}{E_{K}} \sim 0.52 \quad \text{and} \quad \frac{\langle E_{\nu} \rangle}{E_{K}} \sim 0.48 \ . \end{aligned}$$

Note that when one of the decay products has a mass comparable to the parent, it will carry most of the energy, as follows from kinematics considerations.

From Eq. 25 we have

$$P_{\mu}(E, X) = \sum_{\pi,K} \int_{E_{min}}^{E_{max}} dE' \frac{dn_{\pi,K \to \mu}(E, E')}{dE} D_{\pi,K}(E', X) =$$

$$\frac{\varepsilon_{\pi}}{X cos\theta (1 - r_{\pi})} \int_{E_{\mu}}^{\frac{E_{\mu}}{r_{\pi}}} \frac{\Pi(E, X)}{E} \frac{dE}{E} + \frac{0.635 \varepsilon_{K}}{X cos\theta (1 - r_{K})} \int_{E_{\mu}}^{\frac{E_{\mu}}{r_{K}}} \frac{K(E, X)}{E} \frac{dE}{E}. \tag{24}$$

Eq. 24 applies for angles small enough ($< 60°$) so that the curvature of the Earth can be neglected. The limits on the integrals give the range of parent energies that can produce a muon of energy E_μ.

At the typical production energy, due to μ lifetime, the secondary μ does not decay in the atmosphere and can safely reach the detectors as stable particles.
Since they have a small interaction cross section, they are very penetrating. Indeed, muons are traditionally called the "penetrating component" of cosmic rays.
The production spectrum of muons is calculated from the differential (in energy and depth) spectrum of the decaying mesons (π and K):

$$\begin{aligned} D_\pi(E,X) &= \frac{\varepsilon_\pi}{EXcos\theta}\Pi(E,X), \\ D_K(E,X) &= \frac{\varepsilon_K}{EXcos\theta}K(E,X). \end{aligned} \tag{25}$$

So, the double differential spectrum of μ or ν from π and K decay is given by

$$P_{\mu,\nu}(E,X) = \sum_{\pi,K}\int_{E_{min}}^{E_{max}} dE' \frac{dn_{\pi,K\to\mu,\nu}(E,E')}{dE} D_{\pi,K}(E',X), \tag{26}$$

where $\frac{dn_{\pi,K\to\mu,\nu}(E,E')}{dE}$ is the inclusive spectrum of μ or ν from π and K decay with energy E'. In Eq. 26, E_{min} and E_{max} are the minimum and maximum energies of the parent that can give rise to the secondaries.

When $E_\mu \gg \varepsilon_\mu$, both muons decay and energy loss in the atmosphere can be neglected. Then the differential muon energy spectrum at depth X is

$$\frac{dN_\mu}{dE_\mu} = \int_0^X P_\mu(E,X')dX' \tag{27}$$

and the final result is

$$\frac{dN_\mu}{dE_\mu} = \frac{A_0 E_\mu^{-\gamma}}{1-Z_{NN}}\left\{ A_{\pi\mu}\frac{1}{1+B_{\pi\mu}\frac{E_\mu\cos\theta}{\varepsilon_\pi}} + 0.635 A_{K\mu}\frac{1}{1+B_{K,\mu}\frac{E_\mu\cos\theta}{\varepsilon_K}}\right\}. \tag{28}$$

Here

$$A_{\pi\mu} = \frac{Z_{N\pi}\left(1-r_\pi^\gamma\right)}{(1-r_\pi)\gamma}$$

and

$$B_{\pi\mu} = \frac{\gamma+1}{\gamma}\Big(\frac{1-r_\pi^\gamma}{1-r_\pi^{\gamma+1}}\Big)\frac{\Lambda_\pi - \Lambda_N}{\Lambda_\pi \ln\frac{\Lambda_\pi}{\Lambda_N}}.$$

$A_{K\mu}$ and $B_{K\mu}$ are defined in analogous way, with the pion mass replaced by the kaon mass. Substituting typical numerical values for the various quantities one gets:

$$\frac{dN_\mu}{dE_\mu} \approx \frac{0.14E_\mu^{-2.7}}{cm^2\ s\ sr\ GeV} \times \left\{ \frac{1}{1+\frac{1.1E_\mu\cos\theta}{115GeV}} + \frac{0.054}{1+\frac{1.1E_\mu\cos\theta}{850GeV}} \right\}. \tag{29}$$

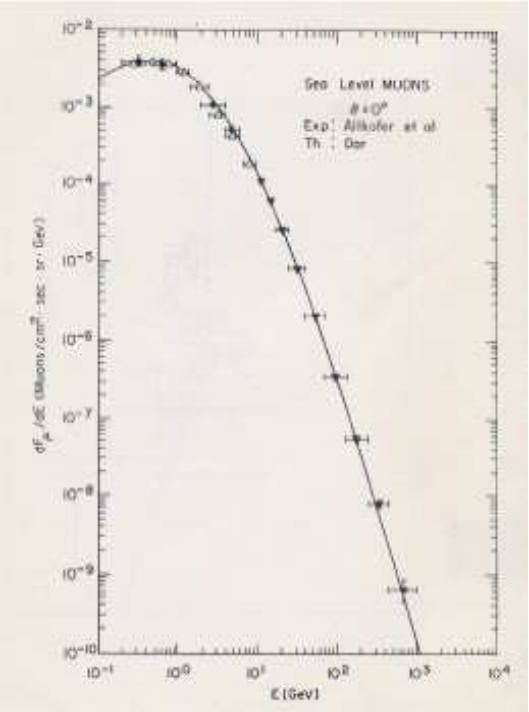

Figure 5: Comparison between measured vertical muon flux at sea level and calculated one from [40]

Taking into account muon decay and energy loss in the atmosphere is possible to obtain more accurate results [40]. Comparison with the measured muon flux at sea level is shown in Fig. 5.
Note that the relative contribution from kaons increases substantially with energy. At low energy, about 5% of vertical muons come from kaons. This

increases to 8% at $E_\mu \sim 100$ GeV, 19% at 1000 GeV and 27% asymptotically. For high energy values we have:

$$\frac{dN_\mu}{dE_\mu} \propto E_\mu^{-(\gamma+1)}. \tag{30}$$

The angular dependence is given by:

$$\frac{dN_\mu}{d\cos\theta_\mu} \propto \sec\theta_\mu \equiv \frac{1}{\cos\theta_\mu} \tag{31}$$

For the small fraction of μ produced by charmed mesons, the prompt decay mechanism leads to an angular distribution

$$\frac{dN_\mu}{d\cos\theta_\mu} = constant\ . \tag{32}$$

A result analogous to Eq. 28 for neutrinos from π and K is:

$$\frac{dN_\nu}{dE_\nu} = \frac{A_0 E_\nu^{-\gamma}}{1 - Z_{NN}} \left\{ A_{\pi\nu} \frac{1}{1 + B_{\pi\nu}\frac{E_\nu \cos\theta}{\varepsilon_\pi}} + 0.635 A_{K\nu} \frac{1}{1 + B_{K,\nu}\frac{E_\nu \cos\theta}{\varepsilon_K}} \right\}, \tag{33}$$

with

$$A_{\pi\nu} = \frac{Z_{N\pi}(1 - r_\pi)^\gamma}{\gamma}, \tag{34}$$

and

$$B_{\pi\nu} = \frac{\gamma + 1}{\gamma} \Big(\frac{1}{1 - r_\pi} \Big) \frac{\Lambda_\pi - \Lambda_N}{\Lambda_\pi \ln \frac{\Lambda_\pi}{\Lambda_N}}\ . \tag{35}$$

As told at the beginning, these are useful approximate analytic solutions. For a better understanding of experimental fluxes we need to take into account a lot of other parameters.
The atmospheric model used is different from the reality. We are not taking into account the three-dimensional development of the shower in the atmosphere nor the bending due to the Earth's geomagnetic field. Moreover both the effects of solar modulation and geomagnetic cut-off on the primary spectrum are disregarded.
All these parameter will be taken into account in the simulations and comparison with experimental data that are presented in this work.

2 Experiments

2.1 BESS experiment

Atmospheric muons observed in the deep atmosphere are carrying information on the interaction of primary and secondary cosmic-ray particles in the atmosphere. Since decay probability and energy loss rate depend on energy, high-statistics measurement of spectral shape can provide useful knowledge to understand propagation process of cosmic-ray particles through the atmosphere. For a more detailed study of neutrino oscillation phenomena observed in atmospheric neutrinos it is essentially important to reduce the systematic errors in the predicted energy spectra of neutrinos. In order to improve the accuracy of the predictions, a detailed understanding of hadronic interactions, as well as precise information of primary cosmic-ray fluxes, is indispensable. As for absolute fluxes of cosmic-ray protons and helium nuclei below 100 GeV, a very precise measurement was carried out by using the BESS detector [50]. Two independent experiments, the AMS [51, 52] and the BESS, show extremely good agreement with each others in their results. Since production and decay process of muons are accompanied by neutrino productions, the muons fluxes correlate directly to the hadronic interactions. Thus the precise measurement of atmospheric muon spectra can also provide important information to improve accuracy of atmospheric neutrino calculations.

2.1.1 BESS detector

The BESS (Balloon-borne Experiment with a Superconducting Spectrometer) detector [54]-[58] is a high-resolution spectrometer with a large acceptance to perform highly sensitive searches for rare cosmic-ray components, and precise measurement of the absolute fluxes of various cosmic rays. Fig. 6 shows a schematic cross-sectional view of the BESS instrument. In the central region, a uniform magnetic field of 1 Tesla is provided by using a thin superconducting solenoidal coil. A magnetic-rigidity ($R \equiv Pc/Ze$) of an incoming charged particle is measured by a tracking system, which consists of a jet-type drift chamber (JET) and two inner-drift-chambers (IDCs) inside the magnetic field. The deflection (R^{-1}) and its error are calculated for each event by applying a circular fitting using up-to 28 hit points, each with a spatial resolution of 200 μm. The maximum detectable rigidity (MDR) was estimated to be 200 GV. Time-of-flight (TOF) hodoscopes provide the velocity (β) and energy loss (dE/dx) measurements. A $1/\beta$ resolution of 1.6% was achieved in this

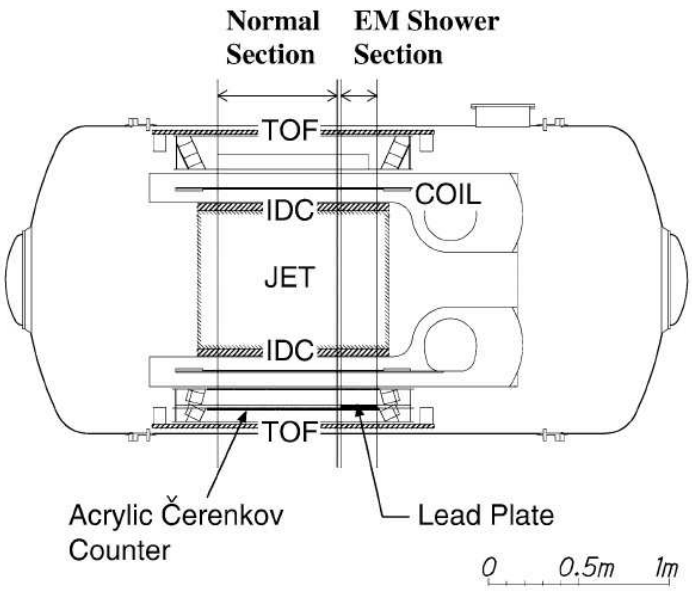

Figure 6: Schematic cross-sectional view of the BESS instrument.

experiment.
Particle identification was made by requiring proper $1/\beta$ as well as dE/dx as a function of the rigidity. An electromagnetic shower counter has been equipped for electron/muon separation. It consists of a 2 X_0 thick lead plate and an acrylic Cerenkov counter. The lead plate covers about 1/5 of the total acceptance. The simple cylindrical shape and the uniform magnetic field make it simple and reliable to determine the geometrical acceptance precisely. The live data-taking time was measured exactly by counting 1 MHz clock pulses with a scaler system gated by a "ready" status that controls the first-level trigger. The resultant live-time ratio was as high as 98.8% through the measurement.

2.1.2 Particle identification

In order to select singly and doubly charged particles, particles were required to have proper dE/dx as a function of rigidity inside both the upper and lower TOF hodoscopes. The distribution of dE/dx inside the TOF counter and the selection boundaries are shown in Fig. 7.

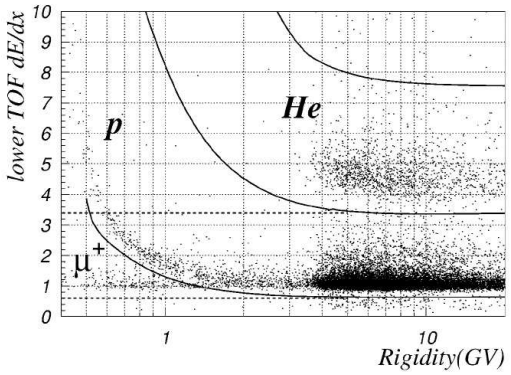

Figure 7: Distribution of dE/dx inside the lower TOF counters. Solid lines show selection boundaries for protons and helium nuclei. Dashed lines show those for muons.Analysis from the BESS-2001 balloon flight carried out at Ft. Sumner, New Mexico, USA on 24th September 2001. See Section 2.1.5.

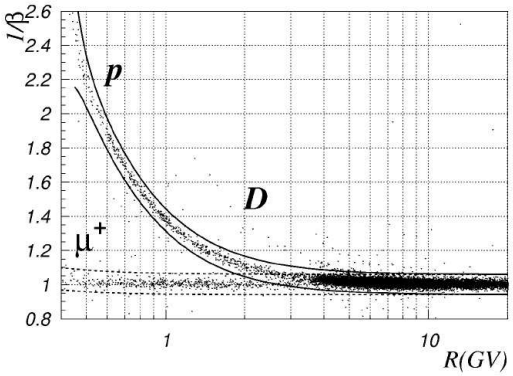

Figure 8: Distribution of $1/\beta$ for Z = 1 particles. Solid lines show the selection boundaries for protons. Dashed lines show those for muons.Analysis from the BESS-2001 balloon flight carried out at Ft. Sumner, New Mexico, USA on 24th September 2001. See Section 2.1.5.

In order to estimate efficiencies of the dE/dx selections for protons and helium nuclei, was used another data sample selected by independent information of energy loss inside the JET chamber. The estimated efficiency in the dE/dx selection at 1 GeV was 98.3 ± 0.4% and 97.2 ± 0.5% for protons and helium nuclei, respectively. The accuracy of the efficiency for protons and helium

nuclei was limited by statistics of the sample events. Since muons could not be distinguished from electrons by the JET chamber, the dE/dx selection efficiency for muons was estimated by the Monte Carlo simulation to be 99.3 ± 1.0%. The error for muons comes from the discrepancy between the observed and simulated dE/dx distribution inside the TOF counters. The dE/dx selection efficiencies were almost constant in the whole energy region discussed here.
Particle mass was reconstructed by using the relation of $1/\beta$, rigidity and charge, and was required to be consistent with protons, helium nuclei or muons. An appropriate relation between $1/\beta$ and rigidity for each particle was required as shown in Fig. 8. Since the $1/\beta$ distribution is well described by Gaussian and a half-width of the $1/\beta$ selection band was set at 3.89 σ, the efficiency is very close to unity (99.99% for pure Gaussian).

2.1.3 Precise measurements of atmospheric muon fluxes at sea level with the BESS spectrometer

The muon flux at sea level has been measured by many groups. However, there are large discrepancies among those measurements much larger than the statistical error quoted in each publication. Therefore it is conceivable that the difference comes from systematic effects such as uncertainties in momentum determination, geometrical factor, exposure time, particle identification, trigger efficiency and normalization procedure.
Here are precise measurements of the absolute flux of atmospheric muons at sea level at Tsukuba (36.2° N, 140.1° E), Japan and Lynn Lake (56.5° N, 101.0° W), Canada by using the BESS spectrometer. The data were collected in 1995 (at Tsukuba) and in 1997-1999 (at Lynn Lake). The cutoff rigidities are 11.4 GV (at Tsukuba) and 0.4 GV (at Lynn Lake).

Data samples

The 1995 ground experiment was carried out at KEK, Tsukuba (36.2° N, 140.1° E), Japan, from December 23-28 [41]. KEK is located at 30 m above sea level. The vertical cutoff rigidity is 11.4 GV [45] ($\lambda = 26.6°$ N geomagnetic latitude [46]). The mean atmospheric pressure in this experiment was 1010 hPa (1030 g/cm^2). The scientific data were taken for a live time period of 291,430 s and 9,148,104 events were recorded on magnetic tapes.
The 1997-1999 ground experiments were carried out in Lynn Lake (56.5° N, 101.0° W), Canada, on July 22, August 16 and July 26, respectively. The

experimental site in Lynn Lake is located at 360 m above sea level. The vertical cutoff rigidity is 0.4 GV [45] ($\lambda = 65.5^\circ$ N geomagnetic latitude [46]). The mean atmospheric pressures in Lynn Lake experiments in 1997-1999 were 980.6 hPa (1000 g/cm^2), 990.5 hPa (1010 g/cm^2) and 964.9 hPa (983.9 g/cm^2), respectively. The total scientific data were obtained for a period of 21,304 s (7011 s, 3949 s and 10,344 s) of live time and 242,934, 137,629 and 354,869 events were recorded on the magnetic tapes, respectively.
The trigger was provided by a coincidence between the top and the bottom scintillators of TOF counters. All triggered events were gathered in the magnetic tapes. The core information (momentum, TOF, etc.) was composed and extracted from the original data. There were two kinds of efficiencies so as to gather atmospheric cosmic-ray data; trigger efficiency ($\varepsilon_{trigger}$), track reconstruction efficiency ($\varepsilon_{reconstruction}$).

Data analysis

Among the factors necessary to obtain the flux, the geometrical acceptance can be calculated reliably by Monte Carlo (MC) methods due to the simple geometry and the uniform magnetic field of the BESS spectrometer. The geometrical acceptance for the vertical muons ($\cos\theta \geq 0.98$) taken in Tsukuba (1995) was about 0.03 m^2sr above 2 GeV/c and decreased gradually at lower momentum. Because east and west effect is not important at high latitude, was analyzed the data taken at Lynn Lake (1997-1999), in a range of $\cos\theta \geq 0.90$ (0.09 m^2sr). The systematic error caused by the east-west effect in Tsukuba was estimated to be 1.0% by comparison with the experimental data and the isotropic MC calculation, and to be negligible in Lynn Lake. The mean value of zenith angle distribution of muon flux was $\cos\theta = 0.990$ for Tsukuba data ($\cos\theta \geq 0.98$), and $\cos\theta = 0.955$ for Lynn Lake data ($\cos\theta \geq 0.90$). The total systematic error of the geometrical acceptance was estimated 0.4%.
The efficiencies used in deriving the muon flux were trigger efficiency ($\varepsilon_{trigger}$), track reconstruction efficiency ($\varepsilon_{reconstruction}$), single track efficiency (ε_{single}) and muon selection efficiency ($\varepsilon_{\mu-select}$). The total efficiency was found to be 98.9%
Summation of all the estimated systematic errors were 2.4% for positive muons and 2.2% for negative muons in Tsukuba and 2.2% for positive muons and 1.9% for negative muons in Lynn Lake.

Atmospheric effect

Variations in cosmic-ray flux by the change of the atmospheric conditions

is called "atmospheric effect". It has been known that there are two main sources of this effect [47] due to variations of the atmospheric pressure and temperature.
The barometric effect has a negative correlation, such that the flux decreases if the atmospheric pressure increases. A specific negative correlation due to the increases of the μ-e decay is expected dominant below 2 GeV/c and another specific negative effect due to the absorption by the ionization loss becomes dominant above 2 GeV/c. The effect at the 25 hPa pressure-difference in two sets of 1995 experimental data on the muon flux amounts to 2.5% below 1 GeV/c and <1% above 5 GeV/c.
In order to analyse the temperature effect, was used two data sets which were taken at different temperature at the 1995 experiment. The observed variation seemed to be consistent with the calculated variation. The variation of muon flux due to the temperature effect in the period of this experiment was $< 1\%$.

Solar modulation

Is necessary to take into account an effect of the solar modulation. The solar activity varies globally with the 11 year solar cycle and the solar minimum was 1996-1997 and the solar maximum happened between 2000 and 2001 according to observations of sunspot numbers [48]. However, this effect appears about one year later in neutron monitor data [49]. Not only the muon flux, but also muon charge ratios (μ^+/μ^-) decrease below 3.5 GV if the low energy primary proton flux decreases by the solar modulation. These charge ratios of 1997-1999 experiments in this energy region (0.58-3.44 GeV/c) were 1.258±0.017, 1.235±0.022 and 1.218±0.014. These decreases were consistent to decreases of the muon flux. The decrease of charge ratios and muon fluxes are caused by decreasing of primary proton flux, therefore the effect of solar modulation were observed. The variations of primary proton flux show about 20% decrease at 2 GeV/c from 1997 to 1999 and the difference of these fluxes becomes much smaller at higher momentum.
The difference of muon flux were 3% around 1 GeV/c.

Results

Fig.9 shows the resultant positive and negative muon fluxes. It is clearly seen that the muon flux measured in Tsukuba and in Lynn Lake were different in lower momentum ranged below 3.5 GeV/c, but were in good agreement in higher momentum beyond 3.5 GeV/c. This is because the cutoff rigidity for

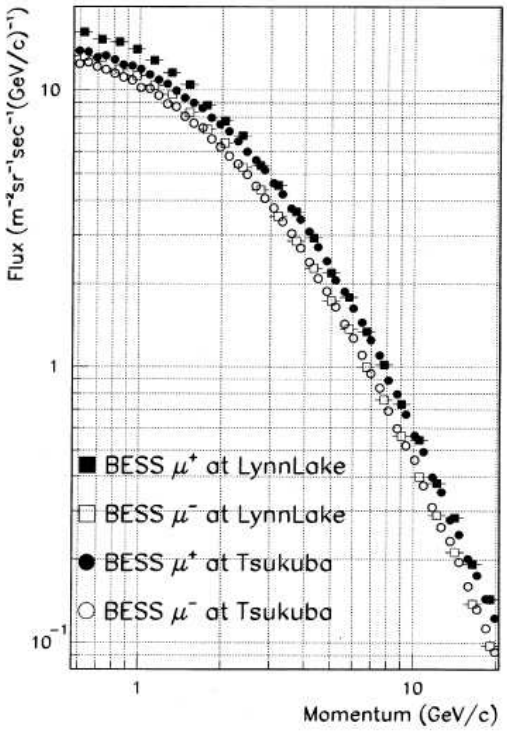

Figure 9: BESS results for vertical differential momentum spectra of the positive and negative muons at sea level.

primary cosmic-rays does not affect the higher momenta.
The vertical absolute fluxes of atmospheric muons have been precisely measured with systematic errors of 2.4% or smaller. Was observed the geomagnetic effect by comparing the muon fluxes observed at Tsukuba, Japan and Lynn Lake, Canada.

2.1.4 Measurements of atmospheric muon spectra at mountain altitude

BESS experiment measured absolute fluxes of atmospheric muons at the top of Mt. Norikura, Japan with the BESS detector, which was the same apparatus that was utilized to measure sea-level muons [53] as well as the primary protons and helium nuclei [50]. These measurements provide fundamental and very useful information about hadronic interactions and geomagnetic effects.

Data samples

The atmospheric cosmic-ray events were observed at Norikura Observatory, ICRR, the University of Tokyo, Japan [42, 43]. It is located at $36°06'N$, $137°33'E$, which is about 40 km southeast of Kamioka. The altitude is 2 770 m above sea level. The vertical geomagnetic cutoff rigidity is 11.2 GV [10]. The experiment was performed during two periods of 17th-19th and 21st-23th of September 1999. During the observation, the atmospheric pressure and temperature varied. The mean (root-meansquare) atmospheric pressure and temperature were 742.4(2.9) g/cm^2 and 10.9 (1.1) °C, respectively. The total live data-taking time was about 4 days.

Corrections

In order to determine the atmospheric muon spectra at the mountain altitude, the following corrections are required; (i) exposure factor, (ii) ionization energy loss, and (iii) interaction loss.
The exposure factor is a product of geometrical acceptance and live-time. The geometrical acceptance defined for this analysis was calculated by simulation technique [59] to be 0.0214 m^2sr for energetic particles which have straight track inside the tracking volume. It was almost constant over the whole momentum range.
In the simulation isotropic trajectories were generated to obtain the geometrical acceptance, however, the flux of atmospheric muons has a zenith angle dependence. In a low momentum region, the dependence might be significant even in the so near vertical direction as $cos\theta_z \geq 0.98$. The discrepancy was included in the systematic errors. The systematic error associated with this discrepancy was estimated to be 3.5% at 0.6 GeV/c and decreased with increasing momentum. The live data-taking time was measured exactly to be 339,874 seconds.
The energy of each particle at the top of the instrument was calculated by summing up the ionization energy losses inside the instrument with tracing back the event trajectory.
In order to estimate the interaction loss probabilities inside the BESS detector, Monte Carlo simulations with the GEANT code [60] were performed. The Monte Carlo simulation of the BESS detector well reproduced the observed event profile. It was concluded that a discrepancy between the observed and simulated event shapes was no more than ±1.6% in the whole momentum range discussed here.

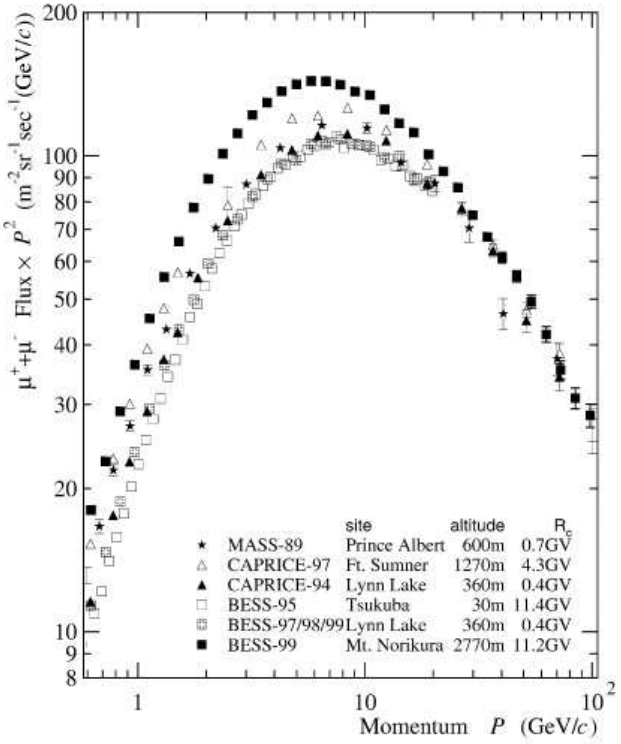

Figure 10: Absolute differential momentum spectra of atmospheric muons. Vertical axis shows the sum of μ^+ and μ^- fluxes multiplied by P^2.Only statistical errors are included. The geomagnetic cutoff rigidity at each site is shown as R_c. The difference among the fluxes is mainly due to the difference in altitudes

The overall errors are less than $\pm 10\%$.
The **results** are shown in Fig. 10 and compared with other absolute flux measurements [53, 61, 62]. A discrepancy between the observed muon fluxes is mainly due to the difference in altitudes.

2.1.5 Measurements of proton, helium and muon spectra at small atmospheric depths with the BESS spectrometer

At small atmospheric depths below a few ten g/cm^2, production process of muons is predominant over decay process, thus we can clearly observe a feature of the hadronic interactions.

In spite of their importance, only a few measurements have been performed with modest statistics because of strong constraints of short observation time of a few hours during balloon ascending periods from the ground to the balloon floating altitude.

Balloon flight

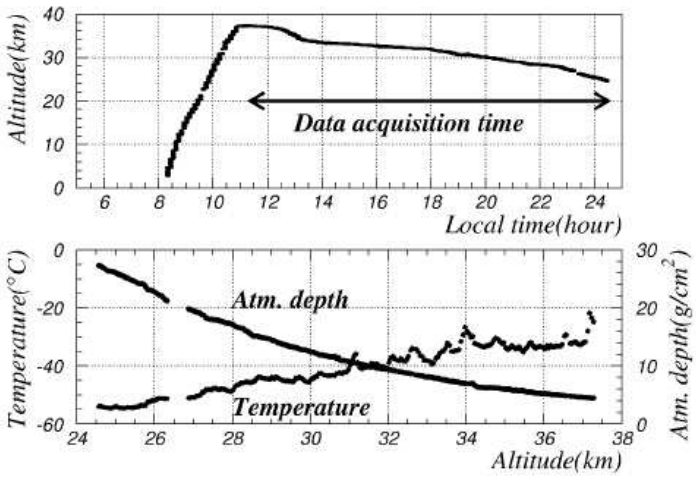

Figure 11: Altitude during the BESS-2001 balloon flight experiment (top). Temperature and residual atmosphere as a function of altitude (bottom).

The BESS-2001 balloon flight was carried out at Ft. Sumner, New Mexico, USA ($34°49'N, 104°22'W$) on 24th September 2001 [44]. Throughout the flight, the vertical geomagnetic cut-off rigidity was about 4.2 GV. The balloon reached at a normal floating altitude of 36 km at an atmospheric depth of 4.5 g/cm^2. After a few hours, the balloon started to lose the floating altitude and continued descending for more than 13 hours until termination of the flight. During the descending period, data were collected at atmospheric depths between 4.5 g/cm^2 and 28 g/cm^2. The atmospheric depth was measured with accuracy of ± 1 g/cm^2, which comes mainly from an error in absolute calibration of an environmental monitor system. Fig. 11 shows a balloon flight profile during the experiment.

Data analysis

The fiducial volume of the detector was limited to the central region of the JET chamber for a better rigidity measurement. The zenith angle (θ_z) was limited within $cos\theta_z \geq 0.90$ to obtain nearly vertical fluxes. For the muon analysis, was used only the particles which passed through the lead plate to estimate electron contaminations. For the proton and helium analysis, particles were required not to pass through the lead plate so as to keep the interaction probability inside the detector as low as possible.

Contamination estimation

Protons

Protons were clearly identified without any contamination below 1.7 GV by the mass selection, as shown in Fig. 8. Above 1.7 GV, however, light particles such as positrons and muons contaminate proton's $1/\beta$-band, and above 4 GV deuterons (D's) start to contaminate it.

Since the geomagnetic cut-off rigidity is 4.2 GV, most of deuterons contaminating proton candidates above 4 GV are considered to be primary cosmic-ray particles. The D/p ratio was found to be 2% at 3 GV. No subtraction was made for deuteron contamination because there is no reliable measurement of the deuteron flux above 4 GV. Therefore, above 4 GV hydrogen nuclei selected which included a small amount of deuterons. The D/p ratio at higher energy is expected to decrease [63] due to the decrease in escape path lengths of primary cosmic-ray nuclei [64] and the deuteron component is as small as the statistical error of the proton flux.

Helium nuclei

Helium nuclei were clearly identified by using both upper and lower TOF dE/dx as shown in Fig. 7. Landau tail in protons dE/dx might contaminate the helium dE/dx band, however this contamination from protons was as small as 3×10^{-4}. No background subtraction was made for helium. Obtained helium fluxes include both ^{3}He and ^{4}He.

Muons

Electrons and pions could contaminate muon candidates. To estimate electron contamination, was used the dE/dx information inside the lower TOF counters covered with the lead plate.

The electron contamination was about 10% of muon candidates at 0.5 GV, and less than 1% above 1 GV. Since in the lower-energy region, the difference between the dE/dx distributions for electrons and muons are small, rejection

power of dE/dx selection are lower. The error was estimated during the fitting procedure to be about 5% at 0.5 GV and 0.1% at 8.0 GV. Accuracy of the electron subtraction was limited by poor statistics of electron events. For the pion contamination was made no subtraction, thus the observed muon fluxes include pions. According to a theoretical calculation [65], the π/μ ratio at a residual atmosphere of 3 g/cm^2 through 10 g/cm^2 was less than 3% at 1 GV and less than 10% at 10 GV.
Between 1.6 and 2.6 GV, protons contamination in the positive muon candidates and its error were estimated by fitting the $1/\beta$ distribution with a double-Gaussian function. The estimated ratio of proton contamination in muon candidates was less than $3.3 \pm 1.3\%$.

Corrections

In order to determine the proton, helium and muon spectra, ionization energy loss inside the detector material, live-time and geometrical acceptance need to be estimated.
The energy of each particle at the top of the instrument was calculated by summing up the ionization energy losses inside the instrument with tracing back the event trajectory. The total live data-taking time was measured exactly to be 40,601 seconds. The geometrical acceptance defined for this analysis was calculated as a function of rigidity by using simulation technique [66]. In the high rigidity region where a track of the particle is nearly straight, the geometrical acceptance is 0.097 m^2sr for protons and helium nuclei, and 0.030 m^2sr for muons. The acceptance for muons is about 1/3 of that for protons and helium nuclei, because is required muons to pass through the lead plate while protons and helium nuclei were required not to pass through the lead plate. The simple cylindrical shape and the uniform magnetic field make it simple and reliable to determine the precise geometrical acceptance. The error which arose from uncertainty of the detector alignment was estimated to be 1%.

Results and discussions

The proton and helium fluxes in energy ranges of 0.5-10 GeV/n and muon flux in 0.5-10 GeV/c, at small atmospheric depths of 4.5 g/cm^2 through 28 g/cm^2, have been obtained from the BESS-2001 balloon flight. The statistical errors were calculated as 68.7% confidence interval. The overall errors including both statistic and systematic errors are less than 8, 10 and 20% for protons, helium nuclei and muons, respectively. The obtained proton and helium spectra are

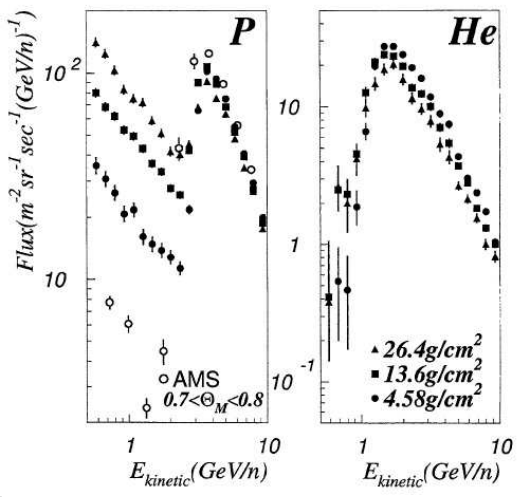

Figure 12: The observed proton and helium spectra. The error bars include statistical error only. In the proton spectra, atmospheric secondary components are clearly observed below 2.5 GeV in the BESS results.

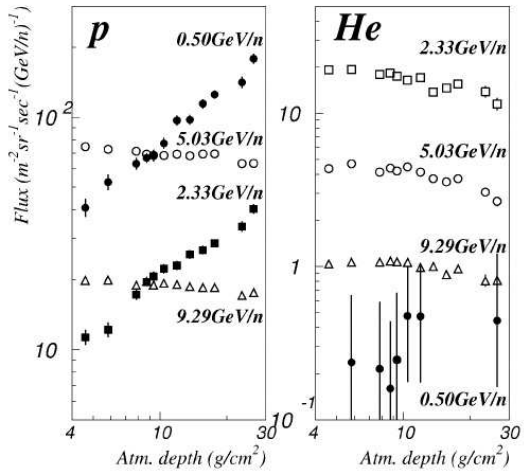

Figure 13: The observed proton and helium fluxes as a function of atmospheric depth.

shown in Fig. 12. Around at 3.4 GeV for protons and 1.4 GeV/n for helium nuclei, a geomagnetic cut-off effect is clearly observed in their spectra.

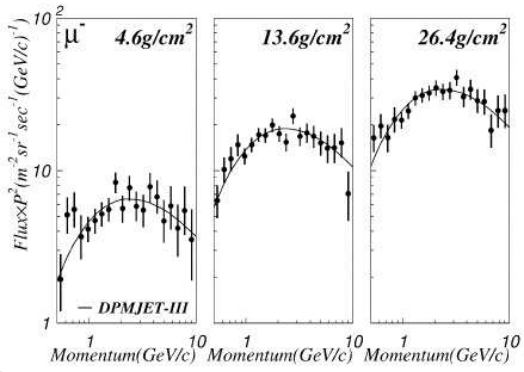

Figure 14: The observed negative muon spectra. The solid lines show theoretical predictions calculated by using DPMJET-III.

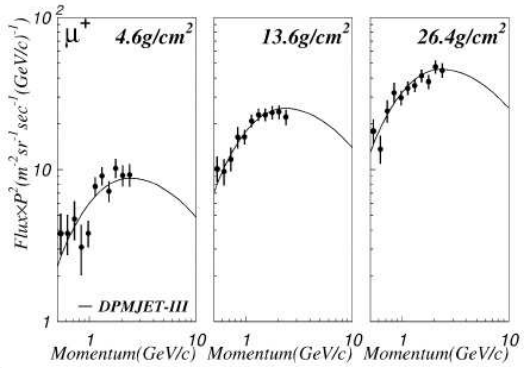

Figure 15: The observed positive muon spectra. The error bars include statistical error only. The solid lines show theoretical predictions calculated by using DPMJET-III.

In the BESS results the atmospheric secondary spectra for protons below 2.5 GeV are observed. Fig. 13 shows the observed proton and helium fluxes as a function of the atmospheric depth. Below 2.5 GeV the proton fluxes clearly increase as the atmospheric depth increases. It is because the secondary protons are produced in the atmosphere. In the primary fluxes above the geomagnetic cut-off, the fluxes attenuate as the atmospheric depth increases. In this energy region, the production of the secondary protons is much smaller than interaction loss of the primary protons. This is because the flux of parent particles of secondary protons is much smaller due to the steep spectrum of

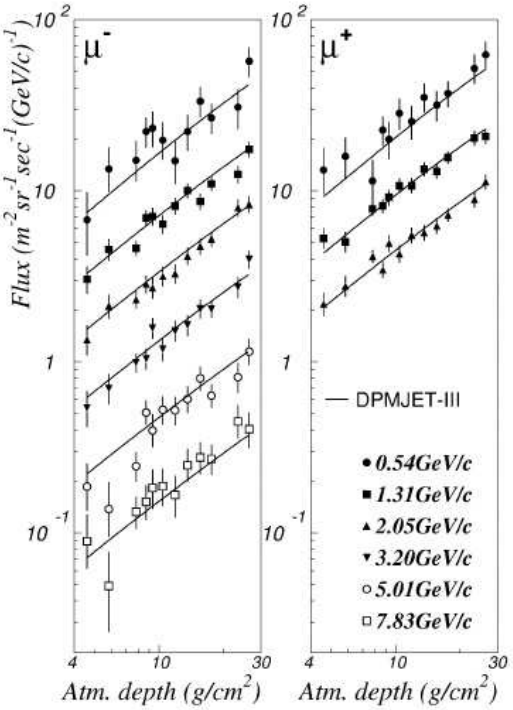

Figure 16: The observed negative and positive muon fluxes. The solid lines show theoretical predictions calculated by using DPMJET-III.

primary cosmic rays. Figs. 14 and 15 show the observed muon spectra together with theoretical predictions. The predictions were made with the hadronic interaction model, DPMJET-III [67], which was used for the evaluation of atmospheric neutrino fluxes [68]. The obtained proton fluxes were used to reproduce the primary cosmic ray fluxes in the calculation. Fig. 16 shows the observed muon fluxes as a function of atmospheric depth together with the calculated fluxes. The calculated fluxes show good agreement with the observed data. The proton and helium fluxes have an overall errors of 8 and 10%, respectively, in an energy region of 0.5-10 GeV/n. The muon fluxes were obtained with an overall error of 20% in a momentum region of 0.5-10 GeV/c.

2.2 L3+Cosmic experiment

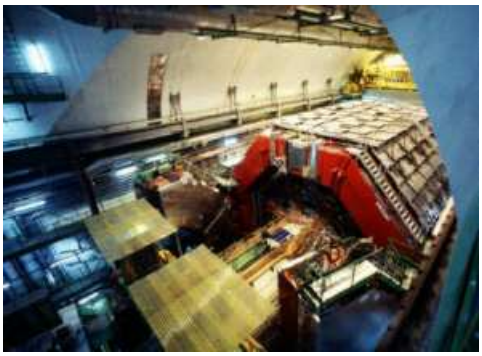

Figure 17: The air shower scintillator array on the roof of the surface hall (54 × 30 m^2) and the L3 detector covered with timing scintillators in the LEP cave)

The L3 detector [73] installed at LEP, CERN, allowed to measure precisely

Figure 18: The air shower scintillator array on the roof of the surface hall (54 × 30 m^2) and the L3 detector covered with timing scintillators in the LEP cave.)

reaction products of e^+e^- collisions and to determine fundamental quantities of the Standard Model of particle interactions. The excellent muon momentum resolution in particular, obtained with the large drift chamber system and the huge magnet, initiated the idea to use this spectrometer also as a tool for cosmic ray and astroparticle physics studies.

A precision spectrometer of large size could provide a major improvement over previous cosmic ray experiments, which gave absolute flux values with uncertainties ranging up to 25% in the energy range 20 GeV to 3 TeV [69]-[72]. The additional possibility to determine also well the angular dependence and the charge ratio permits to constrain the calculated muon neutrino and antineutrino spectra, important for oscillation measurements and for background estimations in neutrino astronomy. In addition these results also constrain the parameters in models for hadronic interactions at very high energies.

Experimental setup

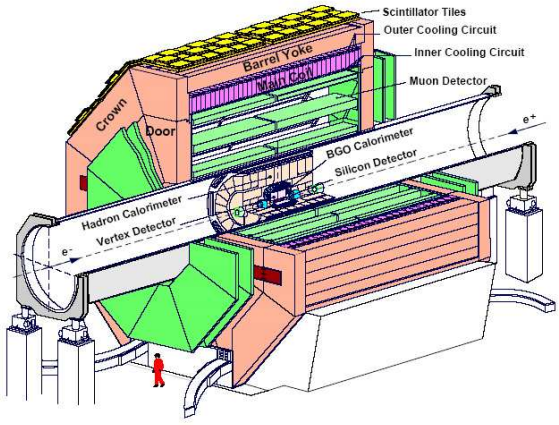

Figure 19: Schematic view of the experimental setup

The parts of the detector used in this analysis are sketched in Figs. 19, 20. Muons have to pass through 30 m of stratified rock overburden, called *molasse*. That limit the minimal detectable muon energy to 15 GeV.
The L3 detector was implemented with an independent trigger and data acquisition system: a surface scintillator array (Fig. 18) was mounted on the roof of the L3 surface hall to detect air showers related to measured muons in the cave.
The arrival time t_0 of a muon is measured with a resolution of 1.7 ns by a 202 m^2 scintillator array placed on top of the L3 detector (Fig. 17. The array is composed of 34 modules, each read out by two photomultipliers in coincidence to reduce noise. Inside a volume of about 1000 m^3 with a magnetic field of 0.5 T, the coordinates and slopes of a muon track are measured in up to six

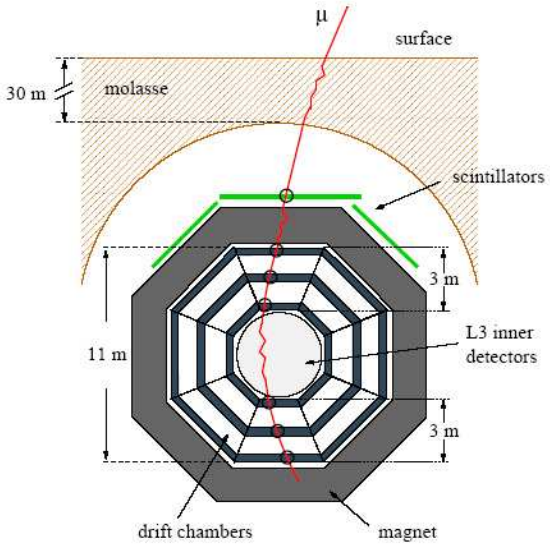

Figure 20: Schematic view of the experimental setup

drift chambers in the bending plane and up to eight times in the non-bending plane. These chambers are arranged concentrically around the LEP beam line in two groups of eight octants, each containing three layers of drift cells. By subtracting the t_0 time from the arrival times of the drift electrons at the sense wires, a track position in each chamber can be reconstructed with a precision of about 60 μm in the bending plane and 1 mm in the non-bending plane.
Only three points are needed to determine the radius of the track in the magnetic field, therefore the momentum of a muon traversing two octants can be measured twice. This redundancy is used to evaluate the detector efficiencies and the resolution of the apparatus. The best resolution is obtained when fitting the six points together over the full track length of 11 meters. The multiple scattering and energy loss inside the L3 inner detectors, as well as the effect of the inhomogeneous magnetic field are taken into account.
Equipped with a trigger and data acquisition system independent of the normal L3 data-taking, L3+C recorded 1.2×10^{10} atmospheric muon triggers during its operation in the years 1999 and 2000.
The L3+C experiment was located 450 m above sea level at a longitude of 6.02° E and a latitude of 46.25° N.
For vertically incident muons, the mean energy loss in the molasse (X = 6854 g cm^{-2}) and the magnet (X = 1227 g cm^{-2}) is 19 GeV at low

momenta and reaches 57 GeV at 1 TeV.

Experimental uncertainties

The momentum bias is dominated by the energy loss uncertainty at low energies (2% at 20 GeV) and by the chamber misalignement at high energies (15% at 1 TeV). The magnetic field uncertainty contributes to less than 0.4% below 3 TeV. The normalization error depends on several items:

- The uncertainty on the acceptance was estimated by comparing independent data samples (from different detector domains, from 1999 and 2000 data, events from different azimuth directions), checking the obtained flux values by modifying the selection criteria, and observing atmospheric effects.

- The influence of the momentum resolution on the minimization result was also analyzed. E.g. a total uncertainty on the absolute vertical flux value of 2.3% is found at 150 GeV. Statistics becomes important above 0.5 TeV.

Discussion of the result

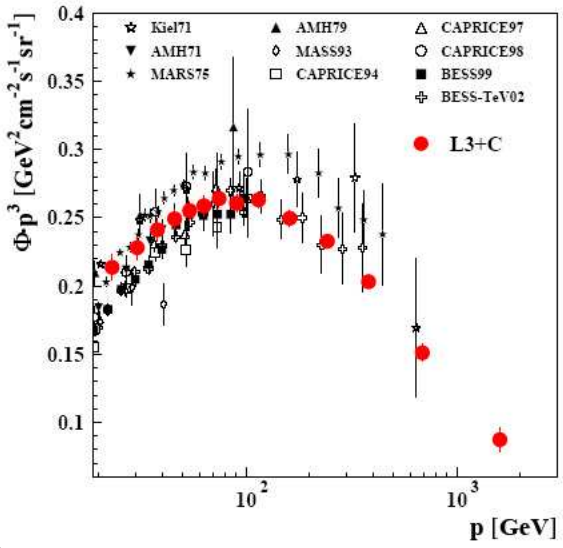

Figure 21: The vertical differential muon spectrum at sea level. The L3+C measurement is compared to previous results providing an absolute flux normalization (for references see text).

It should be noted that the fluxes are neither corrected for the altitude of L3+C

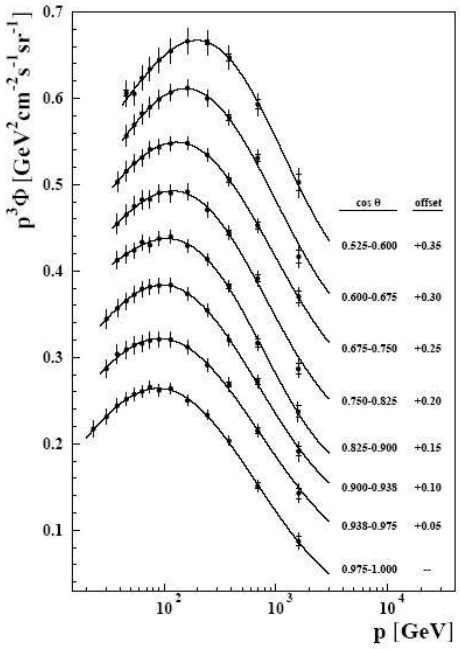

Figure 22: The measured muon flux for zenith angles ranging from 0^0 to 58^0 at 450 m above sea level. Inner error bars denote statistical uncertainty, full bars total uncertainty.

nor for the atmospheric profile to avoid additional theoretical uncertainties. Instead, we quote the average atmospheric mass overburden X above L3+C, which was continuously measured with balloon flights from close to the experiment to altitudes of over 30 km [80].
The measured muon fluxes at the L3+C altitude are shown in Fig. 22 for each zenith angle bin. As no previous continuous zenith angle measurements exist in the large energy range examined here, only the vertical flux can be compared to other experiments, as shown in Fig. 21. Only measurements providing an absolute normalization [81]-[89] are taken into account. The data are extrapolated to sea level using the muon flux predictions of the TARGET [79] program.
The comparison to low energy experiments [83]-[88] gives a good overall agreement with this analysis above about 40 GeV. At lower momenta, a systematic slope difference seems to be present, which corresponds to about

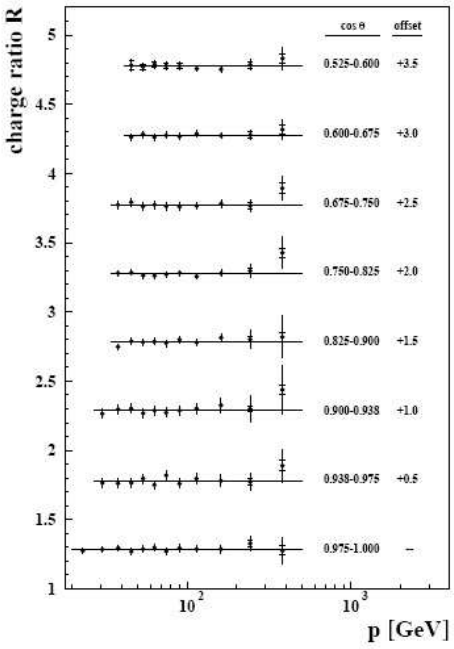

Figure 23: The measured muon charge ratio for zenith angles ranging from 0^0 to 58^0 at 450 m above sea level. $\frac{\mu^+}{\mu^-}$= 1.285 ± 0.003(stat.) ± 0.019(syst.)

three standard deviations of the systematic molasse uncertainty.
The measured charge ratios at the L3+C altitude are shown in Fig. 23 for each zenith angle bin up to momenta of 500 GeV. In the considered momentum range, the charge ratio is independent of the momentum within the experimental uncertainties. The mean value in the vertical direction is found to be 1.285 ± 0.003 (stat.) ± 0.019 (sys.) with a $\chi^2/\text{ndf} = 9.5/11$. This is in good agreement with the average of all previous measurements, 1.270 ± 0.003 (stat.) ± 0.015 (sys.)[78].

3 The FLUKA Monte Carlo code

FLUKA is a general purpose Monte Carlo code for the interaction and transport of particles. It is built and maintained with the aim of including the best possible physical models in terms of completeness and precision. It contains detailed models of electromagnetic, neutrino, muon , hadron-hadron, hadron-nucleus and nucleus-nucleus interactions, covering the range from the MeV scale to the many-TeV one. Charged particle transport (handled in magnetic field too) includes all relevant processes. It also manages interaction and transport of neutrons down to thermal energies (< 20 MeV). Extensive benchmarking against experimental data has been produced (see the references in [174]).
The quality of physics models and the high accuracy of the algorithms make FLUKA a valuable instrument in all cases in which a high degree of reliability of results is required. Among the possible cases, one of these topics concerns the interaction of cosmic rays. FLUKA is already used in space application for dose calculation in long duration flights [175]. Of the same ground, the interaction of cosmic rays with the Earth's atmosphere is of enormous interest both in fundamental research and applied physics, again when dose calculations are required. Applications of FLUKA to predict doses for civil aviation have been already attempted [176].
Dealing with cosmic rays physics, I'll focus the attention on hadronic interaction models.

3.1 Hadronic interactions

The hadronic packages of the FLUKA Monte Code are being developed according to a theoretically inspired approach where interactions should be described in terms of the properties of the elementary constituents. In principle one would like to derive all features of "soft" interactions (low-p_T interactions) from the QCD Lagrangian, as is done for hard processes. Unfortunately the large value of the running coupling constant prevents the use of perturbative calculus. In QCD the color field acting among quarks is carried by the vector bosons of the strong interaction, *i.e.* the gluons, which are "colored" themselves. Therefore the characteristic feature of gluons (and QCD) is their strong self-interaction. If we imagine that quarks are held together by color lines of force, the gluon-gluon interaction will pull them together into the form of a tube or a string. Since quarks are confined, the energy required to "stretch" such a string increases until it is large enough to materialize a quark-antiquark couple from the vacuum. At that point the string breaks into two shorter ones, both with quarks at both ends. Therefore, because of quark confinement, theories based on interacting strings have emerged as a powerful tool in understanding QCD at the soft hadronic scale (the non-perturbative regime). Different implementations of this idea exist, and have obtained remarkable success in describing the features of hadronic interactions. These concepts are embedded in FLUKA in order to give a sound physical base in each step.

At the moment it is not possible to cover all relevant energy ranges by means of a unique numerical model. Different approaches are required, and this requires particular care in order to obtain the proper matching and continuity at transition energies. This important point has been analysed in detail by the FLUKA authors. Apart from paying attention to the phenomenological aspects, the performances of the code are optimized by comparisons with particle production data at single interaction level. The final predictions are obtained with a minimal set of free parameters, fixed for all energies and target/projectile combinations. The results in complex cases, as well as scaling laws and properties, come out naturally from the underlying physical models, and the basic conservation laws are fulfilled "a priori". This approach guarantees, in principle, a very high level of detail in FLUKA. Therefore FLUKA is a very powerful tool for precision calculations when aiming for reaching a deeper understanding and reliability of predictions.

FLUKA contains two models to describe nonelastic hadronic interactions, one for low-intermediate energies up to 5 GeV (PEANUT), and one for higher

energies up to several tens of TeV. The nuclear physics embedded in the two models is very similar. The main differences are a coarser nuclear description (and no preequilibrium stage) and the Gribov-Glauber cascade for the high energy model.

3.1.1 The peanut model

The low-intermediate energy hadronic model of FLUKA is called Pre-Equilibrium Approach to NUclear Thermalization (PEANUT). Presently, PEANUT handles interactions of nucleons, pions, kaons, and γ-rays from about 4 GeV down to reaction threshold (or 20 MeV for neutrons). The reaction mechanism is modeled in PEANUT by explicit (generalized) intranuclear cascade (GINC) smoothly joined to statistical (exciton) preequilibrium emission [92, 93].

At the end of the GINC and exciton chain, the evaporation of nucleons and light fragments (α, d, ^{3}H, ^{3}He) is performed, following the Weisskopf [94] treatment. Competition of fission with evaporation has been implemented, again with a statistical approach. Since the statistical evaporation model becomes less sound in light nuclei, the so called Fermi Break-up model [95, 96] is used instead. In this model the excited nucleus is supposed to disassemble in just one step into two or more fragments, with branching ratios given by plain phase space considerations, corrected for Coulomb barriers when applicable.

The excitation energy still remaining after evaporation is dissipated via emission of γ rays [97].

GINC generalities

The GINC proceeds through hadron multiple collisions in a cold Fermi gas. The hadron-nucleon cross sections used in the calculations are for free nucleons, modified by Pauli blocking, except for pions and negative kaons that requires special treatment. The Fermi motion is taken into account, both to compute the interaction cross section and to produce the final state particles.

Secondaries are treated exactly like primary particles, with the only difference that they start their trajectories already inside the nucleus. Primary and secondary particles are transported according to their nuclear mean field potential and to the Coulomb potential. All particles are transported along classical trajectories, though a few relevant quantistic effects are included.

Binding energies are obtained from mass tables, depending on particle type and on the actual composite nucleus, which may differ from the initial one in case of multiple particle emission. Relativistic kinematics is applied, with

accurate conservation of energy and momentum, and with inclusion of the recoil energy and momentum of the residual nucleus.

Nuclear geometry

In both the INC and the exciton stages, the nucleus is modeled as a sphere with density given by a symmetrized Woods-Saxon [98] shape for A>16, *i.e.*,

$$\rho(r) = \rho_0 \frac{\sinh(R_0/a)}{\cosh(r/a)+\cosh(R_0/a)} \approx \frac{\bar{\rho}_0}{1+\exp\frac{r-R_0}{a}} \tag{36}$$

and by a harmonic oscillator shell model [99] for light isotopes. Proton and neutron densities are generally different, according to the shell model for A<16, and to the droplet model [100, 101] for heavier nuclei.

Fermi motion and the nuclear potential

A standard position-dependent Fermi momentum distribution is implemented in PEANUT:

$$\frac{\mathrm{d}N}{dk} = \frac{|k|^2}{2\pi^2} \tag{37}$$

for k up to a local Fermi momentum $k_F(r)$ given by

$$k_F^{p,n}(r) = \left(3\pi^2 \rho^{p,n}(r)\right)^{\frac{1}{3}} \tag{38}$$

where $\rho^{p,n}$ is the proton or neutron density as defined in the previous paragraph. The Fermi momentum is smeared according to the uncertainty principle, assuming a position uncertainty = $\sqrt{2}$ fm. An example of the resulting distributions is shown in Fig. 24.

The potential depth felt by nucleons at any radius r is given by the Fermi energy plus the relevant binding energy.

Positive Kaons are excellent probes to test the Fermi distribution. They undergo only elastic and charge exchange scattering up to $\approx$ 800 MeV/c, and their interactions are easily modeled starting from phase shift analysis. A nice comparison of PEANUT and experimental data on K^+Pb scattering is shown in Fig. 25.

For pions a nuclear potential has been calculated starting from the standard pion-nucleus optical potential [103].

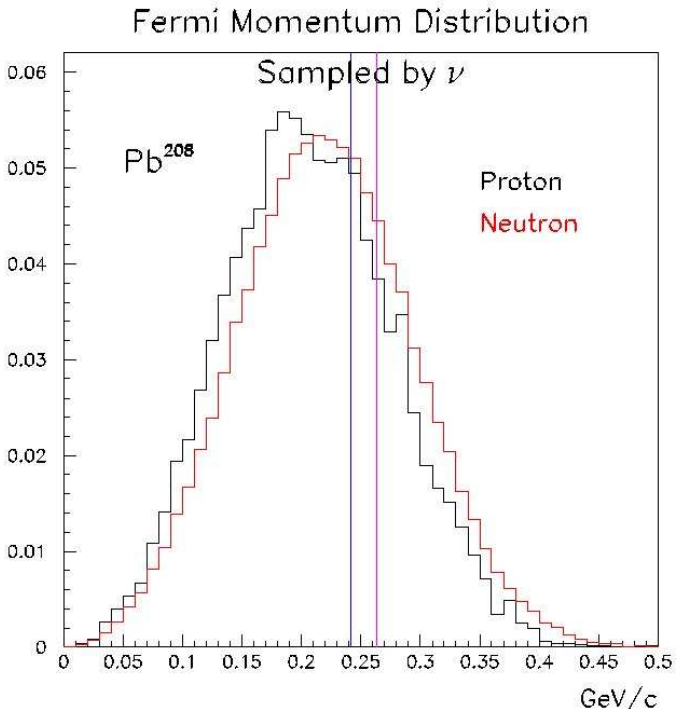

Figure 24: Fermi momentum distribution as sampled by ν_μ in ^{208}Pb. Proton and neutron distributions are shown together with the un-smeared maxima from the central density.

Pion-nucleon cross sections

Pion-induced reactions are complex, mainly because of two-and three-nucleon absorption processes. Above the pion production threshold, the inelastic interactions are handled by a resonance model.

Other pion-nucleon interactions proceed through the non-resonant channel and the p-wave channel with the formation of a Δ resonance. In nuclear matter the Δ can either decay, resulting in elastic scattering or charge exchange, or interact with other nucleons, resulting in pion absorption. The width of the resonance in nuclear matter is thus different from the free one. To account for this the pion-nucleon total cross section used in PEANUT is derived from the free one [104] in the following way:

1. The resonant part is extracted from the free cross section under the assumption of a Breit-Wigner shape with an energy-dependent

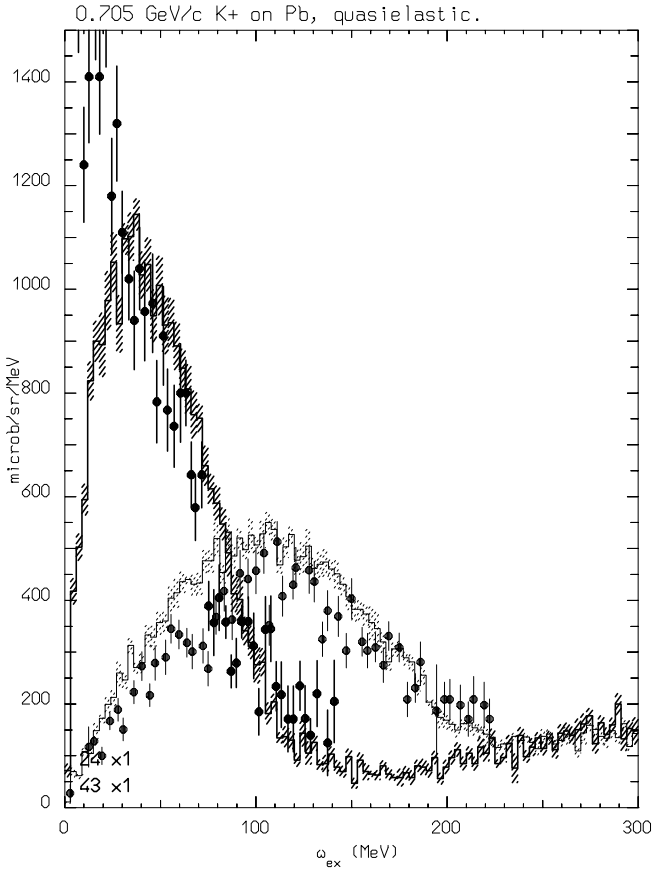

Figure 25: 705 GeV/c $(K^+, K^{+\prime})$ on Pb vs. residual excitation, at 24° and 43°. Histograms: FLUKA, dots: data [102]. Elastic scattering is not included in the calculations. On free nucleons the recoil energy is 43 MeV at 24° and 117 MeV at 43°.

width [106]:

$$\sigma_r = \frac{8\pi}{p_{cm}^2} \frac{M_\Delta^2 \Gamma_F^2}{\left(s - M_\Delta^2\right)^2 + M_\Delta^2 \Gamma_F^2} \tag{39}$$

where p_{cm} is the pion momentum in the pion-nucleon center of mass system, s is the invariant mass squared, and $M_\Delta = 1.232$ GeV.

2. The non-resonant scattering cross section σ_s is obtained by subtracting σ_r from the total experimental cross section.

3. A "new" resonant cross section σ_r^A is calculated, where the free width

Γ_F in Eq. 39 is modified by adding the imaginary part of the (extra) width arising from nuclear medium effects. For this purpose the approach outlined in [105] has been adopted. The Δ effective width thus becomes:

$$\frac{1}{2}\Gamma_T = \frac{1}{2}\Gamma_F - Im\Sigma_\Delta \tag{40}$$

where $\Sigma_\Delta = \Sigma_Q + \Sigma_2 + \Sigma_3$ as calculated by Oset et al. [105]. Σ_Q, Σ_2 and Σ_3 are the partial widths for quasielastic scattering, two-body and three-body absorption.

4. The partial resonant cross section for each channel is obtained from σ_r^A multiplying by the ratio $\frac{\Gamma_i}{\Gamma_T}$ (Γ_i= Γ_F, $2\Sigma_2$ or $2\Sigma_3$). In addition, a two-body s-wave absorption cross section has been derived from the optical model [103] as

$$\sigma_s^A(\omega) = \frac{4\pi}{p}(1 + \frac{\omega}{2m})ImB_0(\omega)\rho \tag{41}$$

where p is the wave number, ω is the pion energy in the lab frame, m is the reduced mass, B_0 is a parameter of the pion optical potential and ρ is the nuclear density.

5. The effective in-nucleus cross section has thus been recalculated as

$$\sigma_t^A = \sigma_r^A + \sigma_s + \sigma_s^A \tag{42}$$

Isospin relations have been extensively applied both to derive the pion-nucleon cross sections in any given charge configuration from the three that are experimentally known, and to weight the different interaction and decay channels of the Δ resonance [106, 107].

Angular distributions of reaction products are sampled according to experimental data both for pion scattering (from free pion-nucleon) and pion absorption (from absorption on ^{3}He and deuterium).

The large cross section for pion absorption in the Δ region can dramatically change the kinematics of ν interactions. As an example, charged pion spectra after ν_μ interaction on iron are shown in Fig. 26, with and without the effect of pion re-interaction. For 1 GeV ν_μ only 55% of the produced π escape from a Fe nucleus, and 75% from an oxygen nucleus.

Quantistic effects

The naive use of free hadron-nucleon cross sections would lead to hadron mean free paths within nuclei that are far too short with respect to reality. There

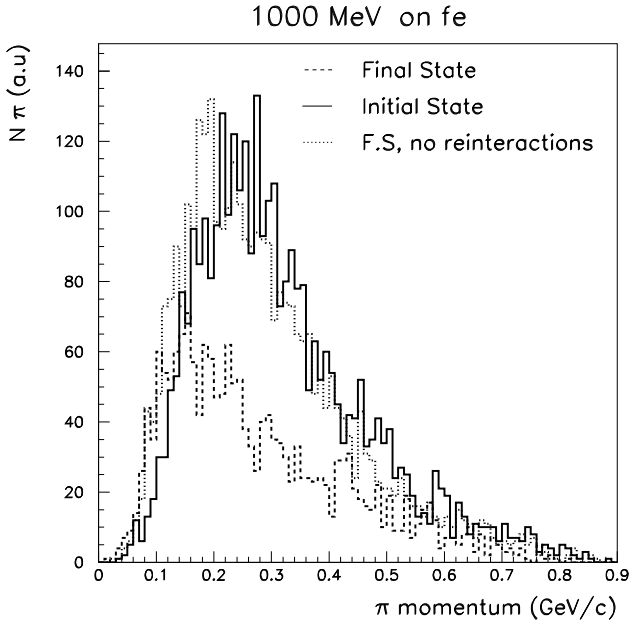

Figure 26: Charged pion spectra after 1 GeV ν_μ interaction on iron.

are many effects that influence the in-medium cross sections, and some of them are accounted for in FLUKA:

- **Pauli blocking**: Any secondary nucleon created in an intranuclear interaction must obey the Pauli exclusion principle, thus it must have enough energy to jump above the Fermi level. For ν interactions, this results in a reduction of the cross section with respect to the one for free nucleons. The effect is important at low ν energies, and is stronger for $\bar{\nu}$ due to the lower average q^2.

- **Nucleon antisymmetrization effects** [**108**]: These effects decrease the probability for secondary particles to reinteract on a nucleon of the same type very close to the production point.

- **Nucleon-nucleon hard-core correlations**: These correlations also prevent secondary particles to collide too close to the production point. Typical hard-core radii used are in the range 0.5-1 fm.

Formation zone and coherence length

The formation zone [109] concept after pion or nucleon interactions has a privileged status among quantistic effects. It can be understood considering that hadrons are composite objects and that the typical time of strong interactions is of the order of 1 fm. The hadrons emerging from an inelastic interaction require some time to "materialize" and be able to undergo further interactions. This time interval can be expressed as

$$t_{lab} \approx \frac{\hbar E_{lab}}{p_T^2 + M^2} \tag{43}$$

where p_T and M are the transverse momentum and mass, respectively, of the emerging hadron. This expression is an approximation suitable for deep inelastic interactions, and it is not fully covariant. In FLUKA the transverse energy entering in Eq. 43 is relative to the jet axis, not to the projectile direction.

In case of elastic or quasi-elastic interactions a more rigorous approach can be followed. The "coherence" length after (quasi)elastic or charge exchange scattering is analogue to the formation zone concept, and such interactions cannot be localized better than the position uncertainty connected with the four-momentum transfer of the collision. Reinteractions occurring at distances shorter than the coherence length undergo interference and cannot be treated as independent interactions on other nucleons. The coherence length concept has been applied to the secondaries produced in quasielastic neutrino-nucleon interactions, with the following recipe: given a two body interaction with four-momentum transfer $q = p_{1i} - p_{1f} = p_{2i} - p_{2f}$, (where in our case the subscript 1 refers to the $i$nitial or $f$inal lepton , and 2 to the hadron) the energy transfer, as seen in a frame where particle 2 is originally at rest, is given by

$$\Delta E_2 = \nu_2 = \frac{q \cdot p_{2i}}{m_2} \tag{44}$$

From the uncertainty principle this ΔE corresponds to an uncertainty in proper time given by $\Delta\tau \cdot \Delta E_2 = \hbar$, which, when boosted to the lab frames, gives a coherence length

$$\Delta x_{lab} = \frac{p_{2lab}}{m_2} \cdot \Delta\tau = \frac{p_{2lab}}{m_2} \frac{\hbar}{\nu_2} \tag{45}$$

To illustrate the effect of the formation zone, FLUKA calculations have been performed where the values from Eqs. 43 and 45 have been multiplied by arbitrary coefficients, ranging from 0 to 100, *i.e.* from no formation zone to almost no reinteractions. The following conclusions can be drawn:

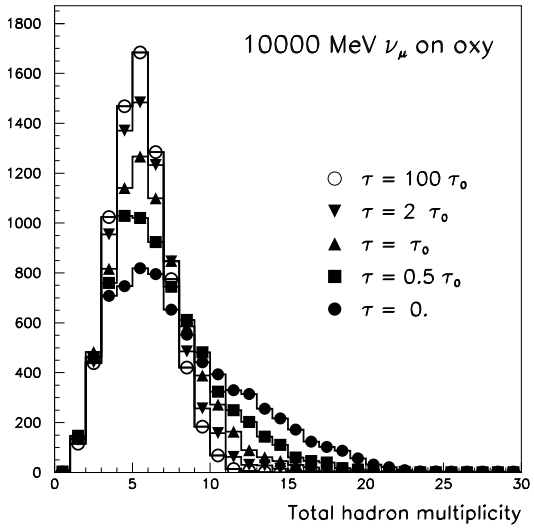

Figure 27: The effect of different formation time (τ) values on the total hadron multiplicity in 10 GeV ν_μ CC interactions on oxygen.

- Reinteractions *increase* the hadron multiplicity with respect to the initial state kinematics, due to the buildup in the intranuclear cascade. An increase in the formation zone therefore corresponds to a suppression of the high multiplicity tail, as shown in Fig. 27.

- Reinteractions *populate* the hadron spectrum in the 100 MeV kinetic energy range, *i.e.* the *cascade* particles, and in the evaporation peak. This is clearly seen in Fig. 28 where for 10 GeV ν_μ on ^{16}O the introduction of the formation zone suppresses the cascade particles by about 40%. Additional variations of a factor two have effects of the order of 15%.

- Reinteractions *depopulate* the hadron spectrum for $p >\approx 1$ GeV/c. In the same test case, the decrease is around 20%. The formation zone approximately halves this percentage.

- Reinteractions *increase* the average emission angle, even for the high energy part of the spectrum. The "standard" formation zone decreases the average hadron emission angle by 10% for $p > 0.2$ GeV/c, and by 4% for $p > 2$ GeV/c (both for 10 GeV ν_μ on ^{16}O).

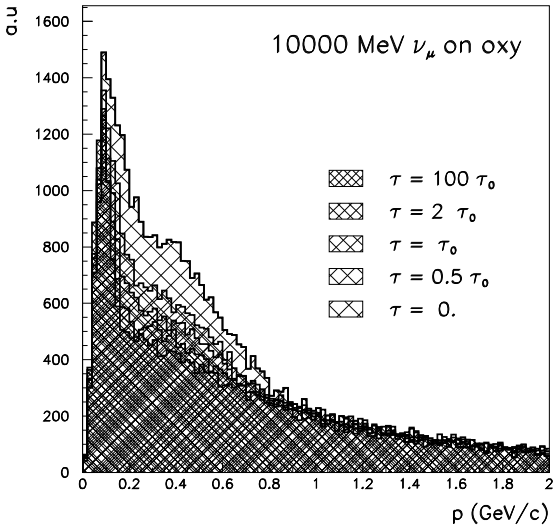

Figure 28: The effect of different formation time (τ) values on the charged hadron spectra in 10 GeV ν_μ CC interactions on oxygen.

3.1.2 The dual parton model for high energies

A theory of interacting strings can be managed by means of the Reggeon-Pomeron calculus in the framework of perturbative Reggeon Field Theory [110], which is an expansion that was developed before the establishment of QCD. Regge theory makes use explicitly of the constraints of analyticity and duality. On the basis of these concepts, calculable models can be constructed, and one of the most successful attempts in this field is the so called "Dual Parton Model" (DPM), originally developed in Orsay in 1979 [111]. It provides the theoretical framework to describe hadron-nucleon interaction from several GeV onwards. DPM exhibits remarkable successes in predicting experimental observables. The quoted references include a vast amount of material showing the capabilities of the model when compared with experimental data. However, it must be stressed that there are other models available, but most of them share an approach based on string formation and decay. For example, the Quark Gluon String Model [118] has been developed more or less in parallel with DPM, sharing most of the basic features of it.

In DPM a hadron is a low-lying excitation of an open string with quarks, antiquarks or diquarks sitting at its ends. In particular, mesons are described as strings with their valence quark and antiquark at the ends. (Anti)baryons

are treated like open strings with a (anti)quark and a (anti)diquark at the ends, made up by their valence quarks.

At sufficiently high energies, the leading term in high energy scattering corresponds to a "Pomeron" exchange (a closed string exchange with the quantum numbers of vacuum), which has a cylinder topology. By means of the optical theorem, connecting the forward elastic scattering amplitude to the total inelastic cross-section, it can be shown that from the Pomeron topology it follows that two hadronic chains are left as the sources of particle production (unitarity cut of the Pomeron). The partons (quarks or diquarks) out of which the chains are stretched carry a net color, while the chains themselves are built in such a way to carry no net color, i.e. they constitute color singlets like all naturally occurring hadrons. In practice, as a consequence of color exchange in the interaction, each colliding hadron splits into two colored systems, one carrying color charge c and the other $\bar{c}$. These two systems carry together the whole momentum of the hadron. The system with color charge c ($\bar{c}$) of one hadron combines with the system of complementary color of the other hadron, in such a way that two color neutral chains are formed. These chains appear as two back-to-back jets in their own centre-of-mass system. The exact way of building up these chains depends on the nature of the projectile-target combination (baryon-baryon, meson-baryon, antibaryon-baryon, meson-meson).

The single Pomeron exchange diagram is the dominant contribution, though higher order contributions with multi-Pomeron exchanges become important at energies in excess of 1 TeV in the laboratory. They correspond to more complicated topologies, and DPM provides a way for evaluating the weight of each, keeping into account the unitarity constraint. Every extra Pomeron exchanged gives rise to two extra chains which are built using two $q\bar{q}$ couples excited from the projectile and the target hadron sea, respectively. The inclusion of these higher order diagrams is usually referred to as *multiple soft collisions*.

Two more ingredients are required to completely settle the problem.

- The first is the momentum distribution for the x variables of valence and sea quarks. Although the exact form of the momentum distribution function, $P(x_1, \ldots, x_n)$, is not known, general considerations based on Regge arguments allow one to predict the asymptotic behavior of this distribution whenever each of its arguments goes to zero. The behavior turns out to be singular in all cases, except for the diquarks. Therefore the true unknown distribution function is approximated with the product of all these asymptotic behaviors, treating all the rest as a normalization

constant.

- The second ingredient is a hadronization model, which must take care of transforming each chain into a sequence of physical hadrons, stable ones or resonances. The basic assumption is that of *chain universality*, which assumes that once the chain ends and the invariant mass of the chain is given, the hadronization properties are the same regardless of the physical process which originated the chain. Therefore the knowledge coming from hard processes and e^+e^- collisions about hadronization can be used to fulfill this task. There are many more or less phenomenological models which have been developed to describe hadronization (examples can be found in [112, 113]). In principle hadronization properties can also be derived from Regge formalism [114].

It is possible to extend DPM to hadron-nucleus collisions [111], making use of the so called Glauber-Gribov approach. Furthermore DPM provides a theoretical framework for describing hadron diffractive scattering both in hadron-hadron and hadron-nucleus collisions. General information on diffraction in DPM can be found in [115] and details as well as practical implementations in the DPM framework in [116, 117].

At energies that are of interest for high energy cosmic ray studies (10-10^5 TeV in the lab), hard processes can no longer be ignored. They are calculable by means of perturbative QCD and can be included in DPM through proper unitarization schemes which consistently treat soft and hard processes together.

The FLUKA implementation of suitable models for heavy ion nuclear interactions is at an operational stage. At medium/high energies (above a few GeV/n) the DPMJET model is used. The major task of incorporating heavy ion interactions from a few GeV/n down to the threshold for inelastic collisions is also progressing and promising results have been obtained using a modified version of the RQMD-2.4 code.

The FLUKA - DPMJET interface

DPMJET is a Monte Carlo model for sampling h-h, h-A and nucleus-nucleus (A-A) collisions at accelerator and cosmic ray energies (E_{lab} from 5-10 GeV/n up to 10^9-10^{11} GeV/n) that has been adapted and interfaced with FLUKA. FLUKA can implement either DPMJET-II.53 [124] or DPMJET-III [126] as an event generator to simulate A-A interactions exclusively. DPMJET (as well as the FLUKA high energy h-A generator) is based on the Dual Parton Model

in connection with the Glauber formalism. The implementation of DPMJET is also considered a possible, future option to extend the FLUKA energy limits for hadronic simulations in general.

Internally, DPMJET uses Glauber impact parameter distributions per projectile-target combination. These are either computed during initialization of the program or can be processed and output in a dedicated run of DPMJET in advance. The computations are CPU intensive for heavier colliding nuclei and it would not be practical to produce the required distributions repeatedly while processing full showers in FLUKA. Therefore, a procedure has been devised to efficiently provide pre-computed impact parameter distributions for a complete matrix of projectile target combinations up to mass number A=246 over the whole available energy range [125].

FLUKA requires A-A reaction cross sections internally in order to select A-A interactions appropriately. Therefore a complete matrix of A-A reaction cross sections is available, along with the Glauber impact parameter distributions. Due to the well established validity of the Glauber formalism, these cross sections can be safely applied down to a projectile kinetic energy ≈1 GeV/n.

DPMJET is called once per A-A interaction. A list of final state particles is returned by DPMJET for transport to FLUKA, as well as up to two excited residual nuclei with their relevant properties. De-excitation and evaporation of the excited residual nuclei is performed by calling the FLUKA evaporation module.

The FLUKA - RQMD interface

Quantum Molecular Dynamics (QMD) approaches are a viable solution for A-A reactions. They represent an improvement over classical INC codes, thanks to their dynamic modeling of the nuclear field among nucleons during the reaction. The treatment of individual two-body scattering/interactions is usually based on similar approaches for INC and QMD codes. Unfortunately, initialization of the projectile and target nuclear states is often difficult and their relativistic extension somewhat problematic.

RQMD-2.4 [127, 128] is a relativistic QMD model which has been applied successfully to relativistic A-A particle production over a wide energy range, from ≈0.1 GeV/n up to several hundreds of GeV/n. The high energy A-A part in FLUKA is already successfully covered by DPMJET. For energies below a few GeV/n several models are under development, either completely new ones, or based on the extension of the present intermediate energy h-A model of FLUKA. Meanwhile, an RQMD-2.4 interface has been developed to enable FLUKA to

treat ion interactions from 100 MeV/n up to 5 GeV/n where DPMJET starts to be applicable.

Several important issues has had to be addressed:

- RQMD does not identify nuclei in the final state, *i.e.* there is no low energy de-excitation (evaporation, fragmentation or fission) performed for neither the excited projectile nor the target residues. This is highly problematic, particularly for the projectile residue, since its de-excitation usually gives rise to the highest energy particle production in the laboratory frame.

- Serious energy non-conservation issues are also affecting the code, particularly when run in full QMD mode (RQMD can be run both in full QMD mode and in the so called fast cascade mode where it behaves as an INC code). Therefore a meaningful calculation of residual excitation energies is impossible with the original code.

These problems have been solved by modifying the code in the following way:

- The nuclear final states are determined from the available information on spectators, correlating the excitation energy to the actual depth of holes left by hit nucleons.

- Then the remaining energy-momentum conservation issues are resolved, taking into account experimental binding energies, as in all other FLUKA models.

- Finally a meaningful excitation energy can be computed and the FLUKA evaporation model is used to produce the particles of low energy (in their respective rest frames) emitted by the excited projectile and target residues.

3.1.3 Benchmarking of FLUKA hadronic models with experimental data

The predictions of FLUKA have been checked with a large set of experimental data collected in accelerator experiments. Reviews of these comparison with data can be found in [119]. Here we shall limit ourselves to show only a few examples, among the most important in view of the application of the code to cosmic ray applications.

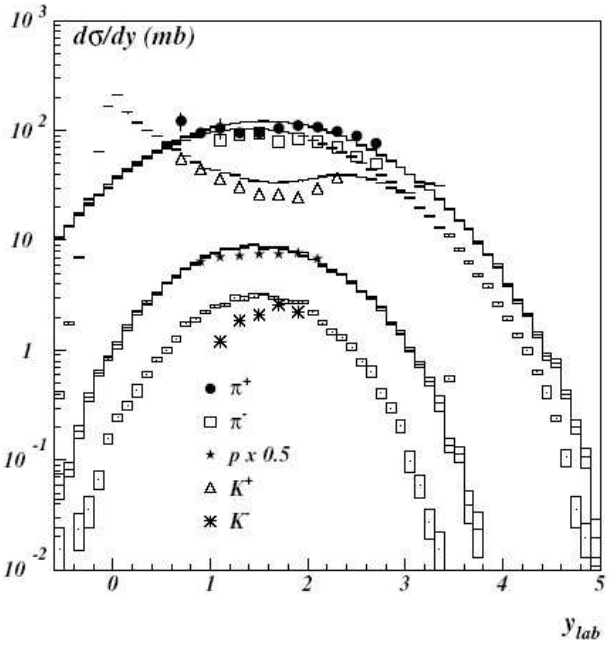

Figure 29: Rapidity distribution of $\pi^{+/-}$, $K^{+/-}$ and protons for 14.6 GeV/c protons on Be [120]. Histograms are simulated data.

Two sets of data are of particular relevance to check the quality of a model to be used for the calculation of atmospheric muons and neutrino fluxes. These concern p-Be collisions. In [120] is it mainly the central rapidity region that has been explored, see Fig. 29, while in [121] the forward region has been investigated, see Fig. 30. In both cases the agreement with FLUKA predictions is quite good. Measurements of $\pi^{\pm}$ and $K^{\pm}$ production rates by 400 GeV/c protons on Be targets were performed by Atherton et al. [122] for secondary particle momenta above 60 GeV/c and up to 500 MeV/c of transverse momentum. Recently the NA56/secondary particle yields (SPY)

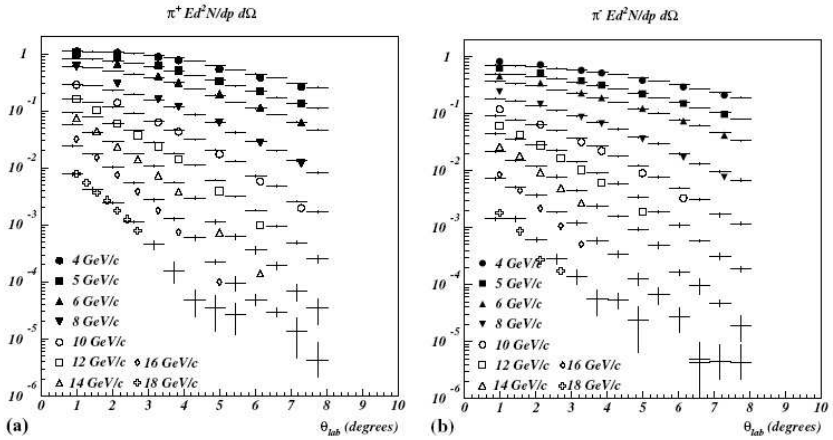

Figure 30: Double differential particle yield for π^+ (a) and π^- (b) for 24 GeV/c protons on Be (symbols extrapolated from the double differential cross-section reported in [121]). Histograms are simulation results. Data are given as a function of θ_{lab} for different momentum bins.

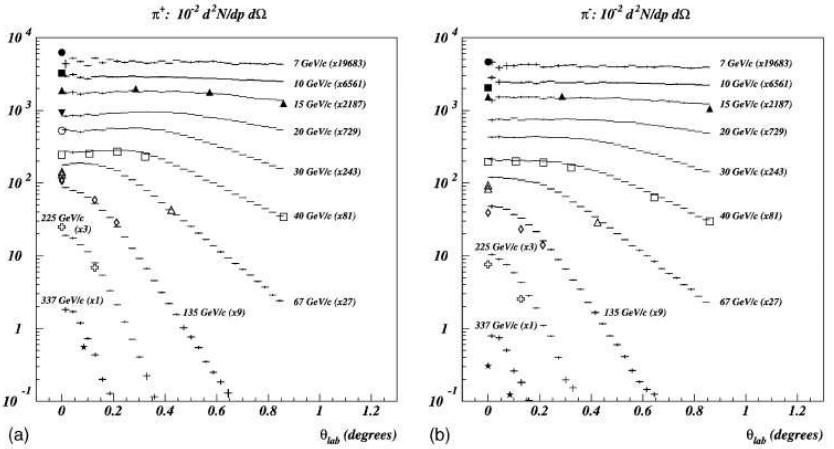

Figure 31: Double differential cross-section for π^+ (a) and π^- (b) production for 450 GeV/c protons on a 10 cm thick Be target [122, 123]. Histograms are simulation results. Data are given as a function of θ_{lab} for different momentum bins. The distributions are scaled by increasing factors (reported in the figure) to allow a clearer separation.

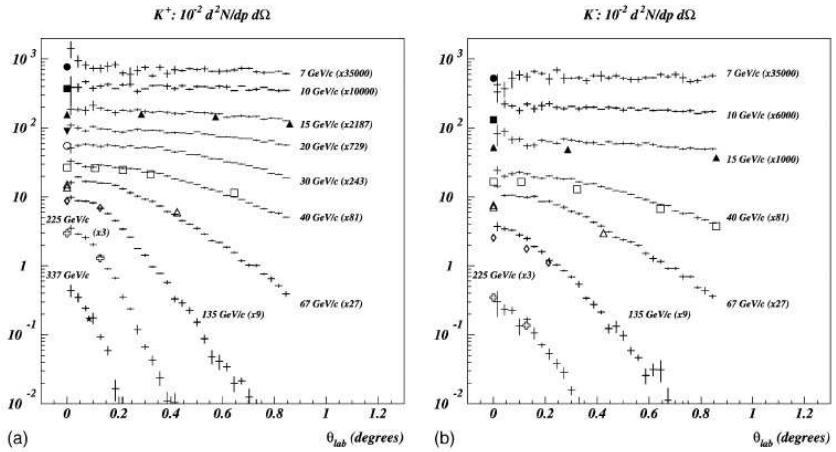

Figure 32: Double differential cross-section for K^+ (a) and K^- (b) production for 450 GeV/c protons on a 10 cm thick Be target (data from [122] and [123]). Histograms are simulation results. Data are given as a function of θ_{lab} for different momentum bins. The distributions are scaled by increasing factors (reported in the figure) to allow a clearer separation.

experiment [123] was devoted to direct measurements of these yields in the momentum region below 60 GeV/c. The SPY experiment measured the production at different angles θ and momenta $P \leqslant 135$ GeV/c down to 7 GeV/c for pions, kaons, protons and their antiparticles, using a 450 GeV/c proton beam impinging on Be targets. These data have been extremely valuable to improve the hadronization model of FLUKA in order to arrive at the present version. FLUKA is in agreement with the Atherton et al. and the SPY measurements at the level of 20% in the whole momentum range of all secondaries, with the exception of a few points mainly for negative kaons. The case for pions is reported in Fig. 31, and the analogous plot for kaons is given in Fig. 32. Also the θ dependence of the measured yields is reasonably described by FLUKA. The measured $K^{\pm}/\pi^{\pm}$ ratios are reproduced to better than 20% below 120 GeV/c.

Most recent validation of the FLUKA hadronic models is the comparison with the HARP experiment [129]. The experiment investigates particle production by p beams on several targets in the range of 1.5-15 GeV/c. In Fig. 33 is shown the first published results for 12.9 GeV/c protons on Al target. The π^+ production cross section as a function of emission momentum and angle

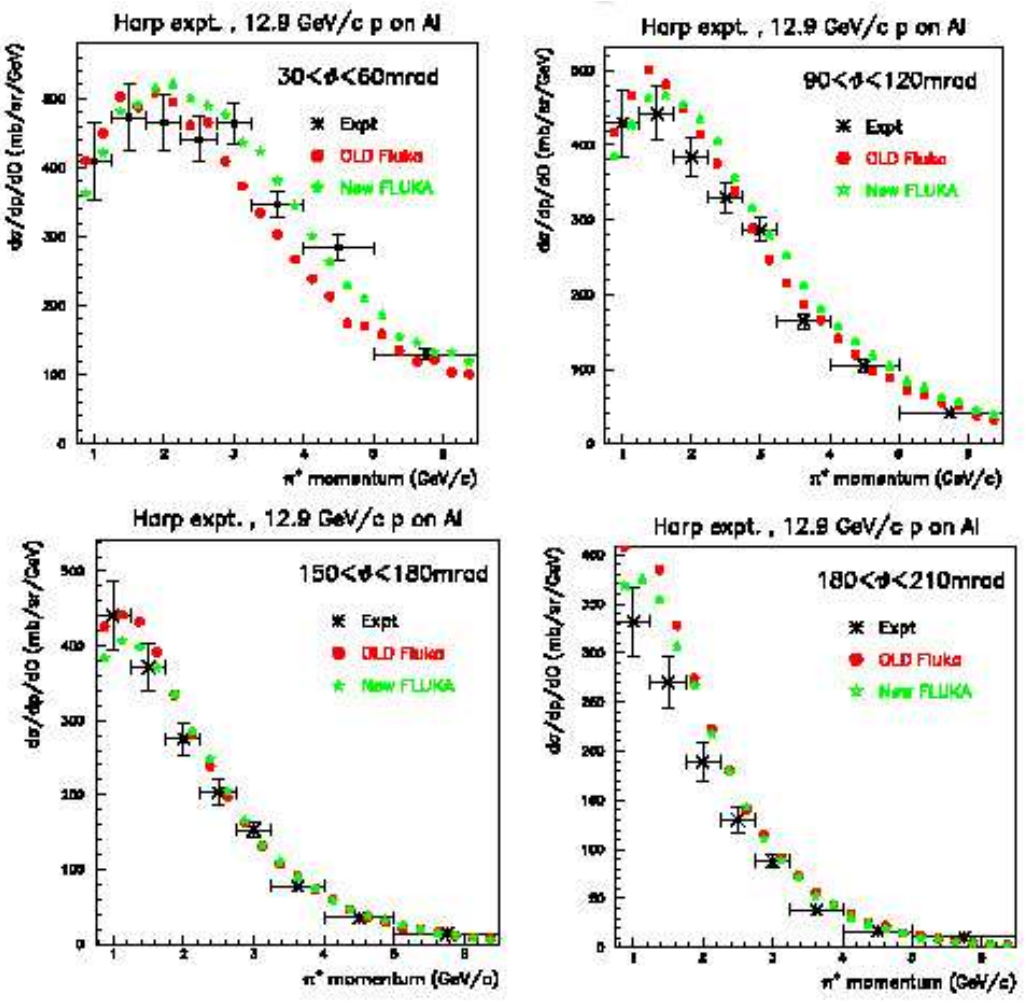

Figure 33: Data from the HARP experiment at CERN. 12.9 GeV/c p on Al π^+ production cross section as a function of emission momentum and angle.

is compared with the old and new FLUKA models.

Recently a validation of the DPMJET-III hadronic model was done by a comparison with data from the NA49 experiment at CERN SPS [130] Figs. 34, 35 show the π^+ and π^- production by 158 GeV/c p beams on p and C targets as a function of Feynman-x and the rapidity distributions.

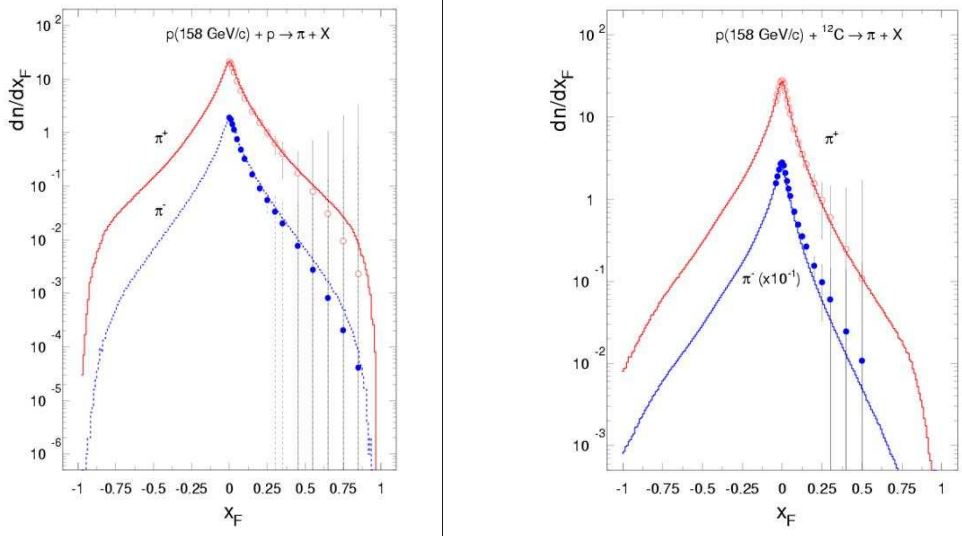

Figure 34: $p + p$ on the left and $p + C$ on the right. π^+, π^- production as a function of Feynman-x.

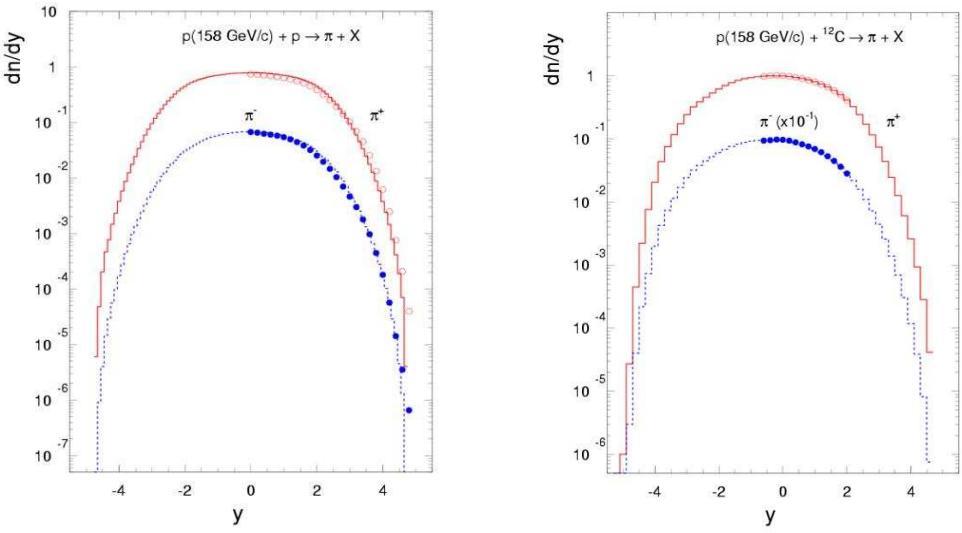

Figure 35: p+p on the left and p+C on the right. π^+, π^- rapidity distributions.

3.2 Features of nucleon-air collisions in the FLUKA model

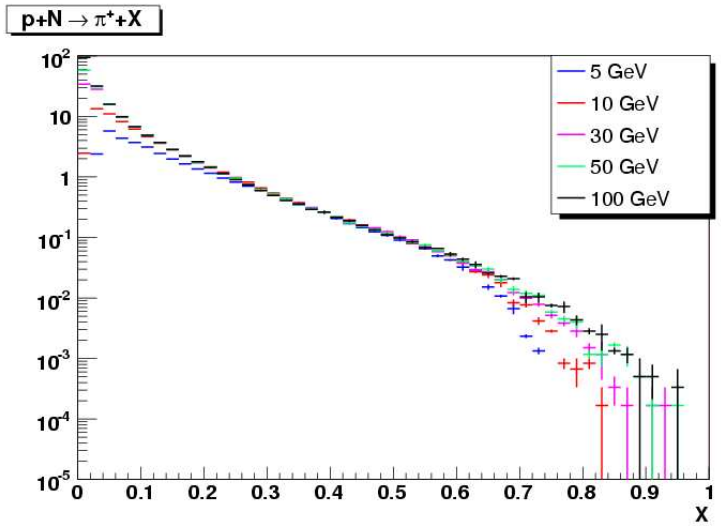

Figure 36: dN/dx_{lab} for positive pions produced by FLUKA in p-air collisions at different kinetic energies of the proton projectile.

In the final state of a high energy interaction one finds the fragments of the target nucleus, a leading nucleon that carries the baryon number of the projectile, a number of mesons, mostly pions, with a non-negligible contribution of kaons. In addition one has to consider the production of nucleon-antinucleon pairs and of heavy flavors. In order to characterize the features of nucleon-air collisions that are relevant in this discussion, I recall few fundamental quantities introduced in Section 1.2: the nucleon-air cross-sections, the distribution of the energy fraction carried away by produced particles and the "spectrum weighted moments" Z_{ij}, all as a function of projectile energy.

In FLUKA, total, elastic and inelastic cross-sections for hadron-nucleus collisions are derived in the framework of the Glauber formalism, using as input the tabulated data (when they exist) of the Particle Data Group for hadron-hadron collisions.

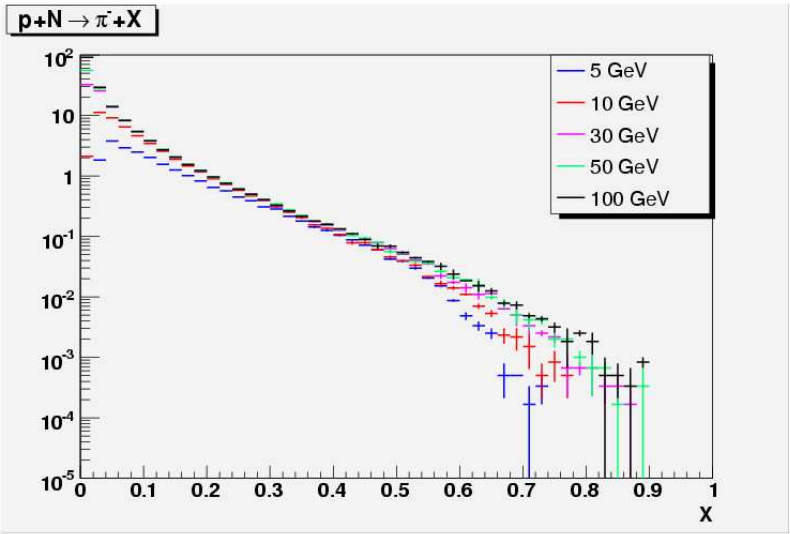

Figure 37: dN/dx_{lab} for negative pions produced by FLUKA in p-air collisions at different kinetic energies of the proton projectile.

For our purposes, particle production can be conveniently studied in terms of a longitudinal non-dimensional variable like $x_{lab} = E_j/E_i$, which is the ratio of the total energies of the secondary particle j over the primary particle i (x_{lab} is approximately equal to x_F in the forward region). We can then construct the $\mathrm{d}N_{ij}/\mathrm{d}x_{lab}$ distributions. These are the differential multiplicity distributions of secondary j as produced by primary i in collisions with air nuclei as a function of x_{lab}. Examples of the x_{lab} distribution in p-air collisions predicted by FLUKA are shown in Figs. 36-39, respectively, for produced π^+, π^-, K^+ and K^-, at different kinetic energy of the projectile. Here x_{lab} is defined as the ratio of secondary total energy with respect to the primary total energy.

The spectrum weighted moments are defined as

$$Z_{ij} = \int_0^1 \left(x_{lab}\right)^{\gamma-1} \frac{dN_{ij}}{dx_{lab}} dx_{lab} \tag{46}$$

where $\gamma = 2.7$ is the approximate spectral index of the differential cosmic ray spectrum. Their use in the literature is justified by the fact that the inclusive yield of secondary cosmic ray particles at a given energy is almost proportional

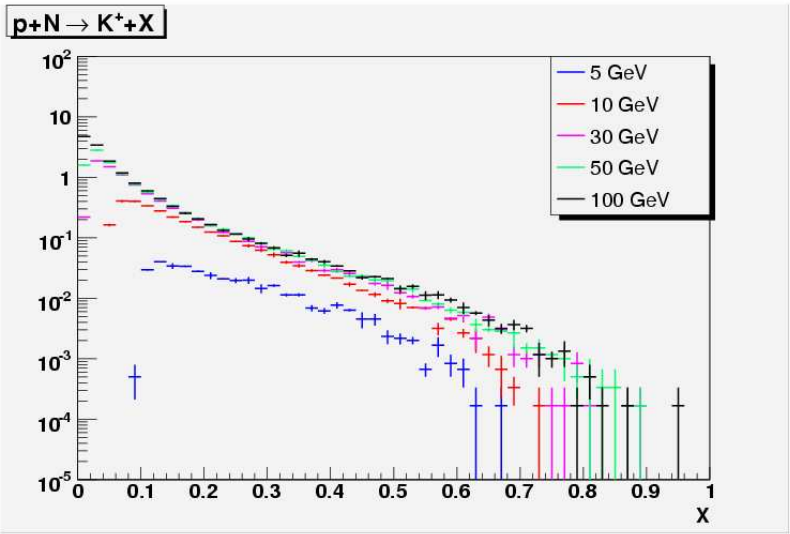

Figure 38: dN/dx_{lab} for positive kaons produced by FLUKA in p-air collisions at different kinetic energies of the proton projectile.

to Z, when the primary spectrum is a power law with a constant spectral index in the whole useful energy spectrum. This is a good approximation for nucleon energies exceeding the TeV scale, but it is not the case in the range of energies considered in this work, since a single power law does not fit the primary spectrum. However, they remain a useful and commonly accepted tool to characterize and compare different interaction models. The resulting spectrum weighted moments for the energies shown in Figs. 36-39 are tabulated in Table 4.

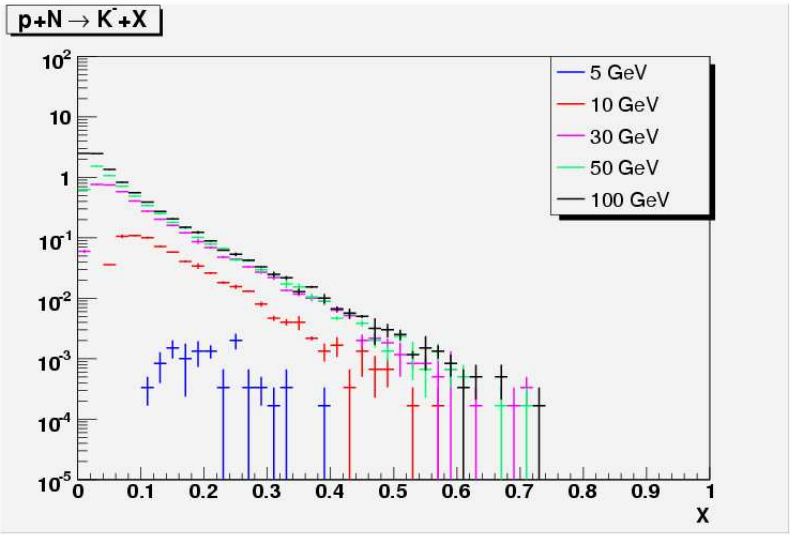

Figure 39: dN/dx_{lab} for negative kaons produced by FLUKA in p-air collisions at different kinetic energies of the proton projectile.

E_k^p (GeV)	p	$nucl$	π^+	π^-	K^+	K^-
5	0.499436	0.735440	0.0313886	0.0169552	0.00066900	1.43247e-05
10	0.271731	0.424942	0.0403301	0.0240934	0.00315013	5.02071e-04
30	0.199909	0.291563	0.0422783	0.0283846	0.00481658	1.72275e-03
50	0.185910	0.268332	0.0428086	0.0291373	0.00528883	2.09420e-03
100	0.179621	0.254491	0.0430343	0.0297099	0.00560599	2.43725e-03

Table 4: Spectrum weighted moments (for a spectral index of the differential primary spectrum $\gamma = 2.7$) for secondary particles produced in p-air collisions as a function of the projectile kinetic energy.

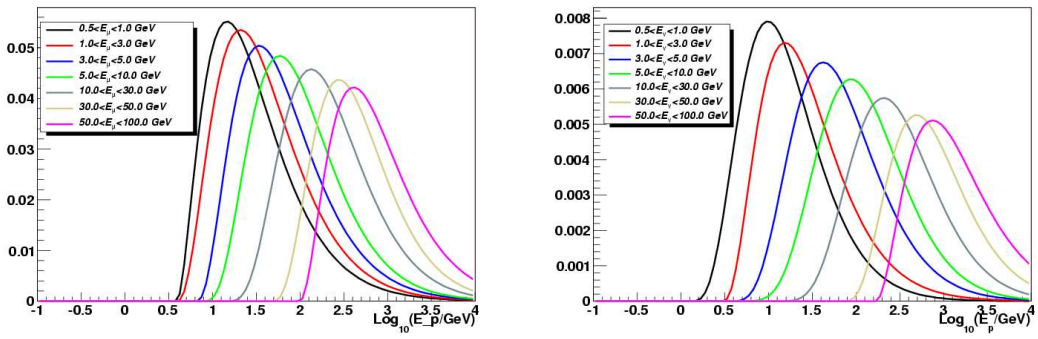

Figure 40: Primary proton energy distributions for different muon (left) and neutrino (right) energies.

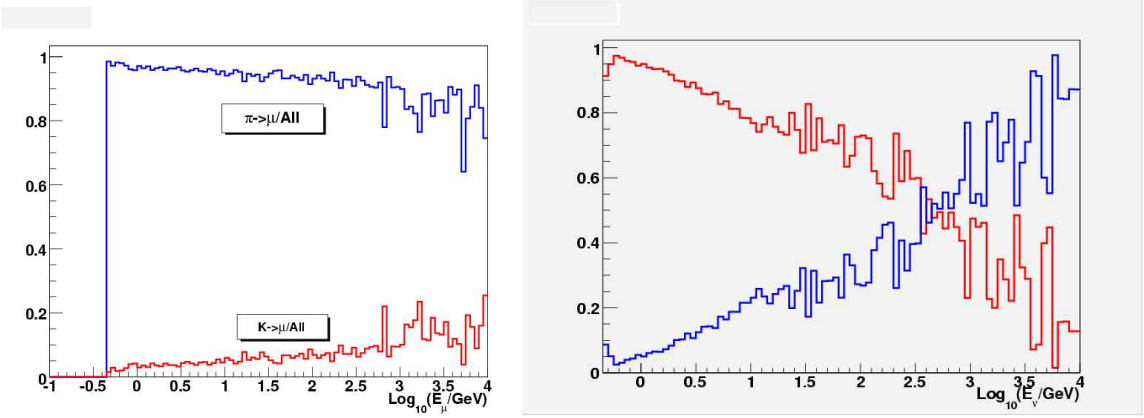

Figure 41: Muon (left) and neutrino (right) over-all ratios related to π and K contributions.

In Figs. 40-45 we show FLUKA calculations of particles in the atmosphere and at ground level. In Fig. 40 are shown distributions of primary proton

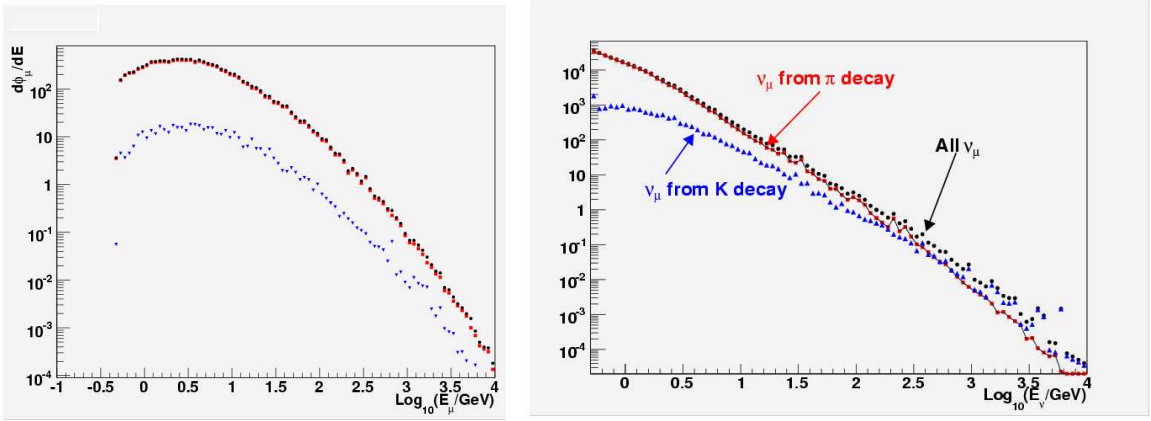

Figure 42: Muon (left) and neutrino (right) spectra with contributions from π and K decay.

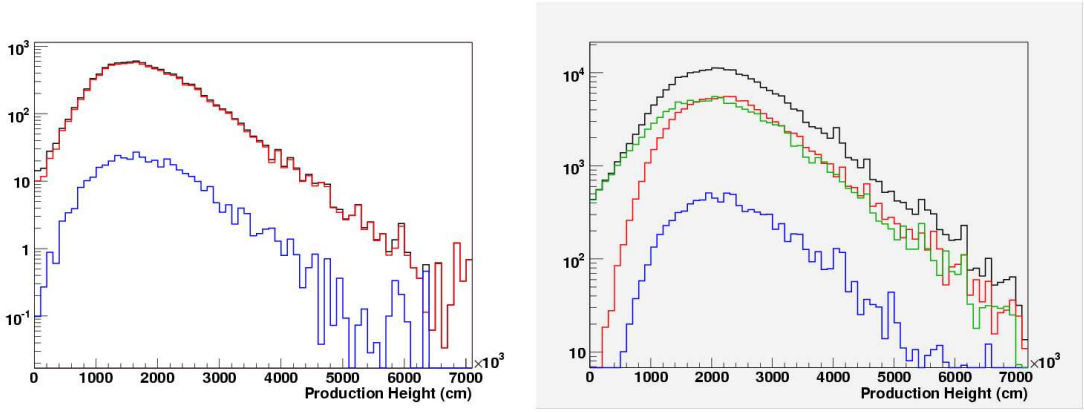

Figure 43: Production altitude for muons (left) and neutrinos (right) that reach the ground level. Green line: from μ decay. Red line: from π decay. Blue line: from K decay.

energy related to protons that produce μ and ν at ground level with energies into fixed windows ("response curves" [1]). Note that muons are produced in average by a primary proton of $E_0 \sim 10E_\mu$. In Fig. 41 are shown the muon and neutrino over-all ratios related to π and K contributions. Above 100 GeV kinematic effects make K more efficient than π in ν production. Fig. 42 shows muon and neutrino spectra with contributions from π and K decay. In Fig. 43

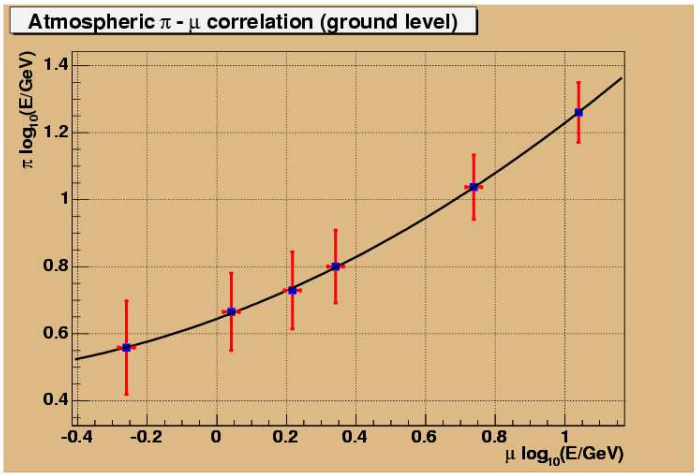

Figure 44: Atmospheric $\pi - \mu$ energy correlation at ground level.

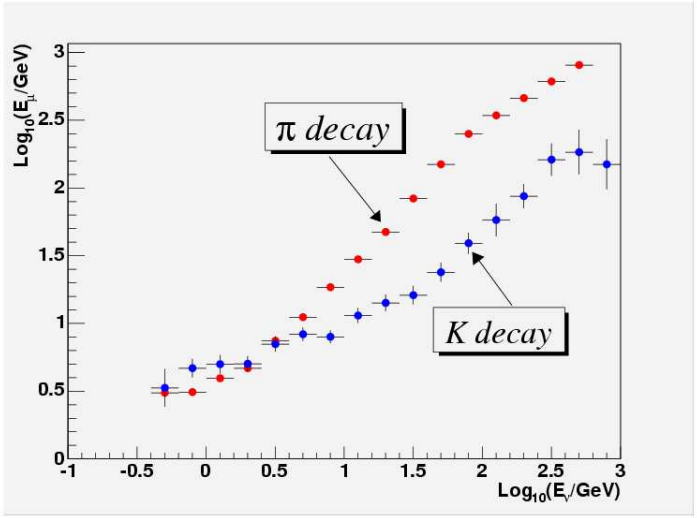

Figure 45: $\mu - \nu$ energy correlation at ground level for muons from π and K decay.

are shown the production altitude for muons and neutrinos that reach the ground level. Fig. 44 represents the atmospheric $\pi - \mu$ energy correlation at ground level. For example, a muon of 10 GeV comes from a pion of $\sim$17 GeV. Fig. 45 represents the $\mu - \nu$ energy correlation at ground level for muons from π and K decay.

3.3 Cosmic rays in FLUKA

A complete calculation to determine particle fluxes in the atmosphere requires:

- the determination of the spectrum and composition of cosmic rays at the local interstellar medium,
- the determination of changing conditions in the solar wind magnetic field and the resulting interaction with the inward flow of galactic cosmic rays from the local interstellar medium,
- the determination of the trajectories of cosmic rays through the Earth's geomagnetic field,
- the transport of the surviving incident cosmic rays through the Earth's atmosphere to various depths.

In the following will be described the set of tools and packages that have been developed for the FLUKA environment to simulate the production of secondary particles by primary cosmic rays interacting with the Earth's atmosphere. These tools, in different versions, have already been successfully used for fundamental physics research [177, 178] and are qualified for applications like those of relevance for the DOSMAX (Dosimetry of Air Crew Exposure during Solar Maximum) project (ARCS research group) [168].
These packages are still in evolution in order to update the physics models and to arrive to a more "user friendly" application program.

The set of FLUKA tools for cosmic ray simulation, not included in the standard distribution, includes the following items:

- A tool to prepare the primary cosmic ray spectra (a code derived from a NASA code (HIZ) which is described in Section 3.3.1).
- A code to generate a 3-D geometrical description of the Earth atmosphere, prepared according to the specifications of the "Combinatorial Geometry" read out by FLUKA. The same program also generates the material specifications for FLUKA.
- A library of user routines (libnuatmmvax) used to build the FLUKA executable capable of managing event generation, geomagnetic effects and particle scoring.

3.3.1 Primary spectrum

The primary flux of galactic cosmic rays is assumed to be uniform and isotropic far from the Earth, and it is locally modified by the effects of the geomagnetic field.
Cosmic rays impinging on the Earth atmosphere are observed over a wide energy range that spans $\sim$ 12 orders of magnitude. The nature and the origin of these particles are depending on the energy range considered.
Up to the energy of the order $\sim$ 100 MeV/nucleon the observed flux of cosmic rays reaching the Earth is of heliospheric origin. The solar wind, a steady flux of charged particles outgoing from the sun, prevents extra-solar cosmic rays with energy below this limit to reach the Earth vicinity. Most of the cosmic ray flux observed below $\sim$ 100 MeV is composed of Solar Energetic Particles (SEP). These particles are fully ionized nuclei present in the solar wind and in the solar system interplanetary medium, which are accelerated by shock waves in the solar wind flux.
A component that is distinguishable from the SEP is contributing to the fluxes in the energy range of $10 \div 50$ MeV/nucleon: the so called Anomalous Cosmic Rays (ACR). ACR are single ionized nuclei reaching the top of the Earth's atmosphere and are believed to represent interstellar neutral nuclei that have drifted into the heliosphere, become ionized by the solar wind or by the UV radiation, and then are accelerated at energies $>$ 10 MeV/nucleon, probably at the solar wind termination shock.

Extra-solar cosmic rays, usually called Galactic Cosmic Rays (GCR), represent the dominant component of the cosmic rays flux in the Earth vicinity, for energies above $\sim$ 10 MeV. This is the component of interest for our study. They are particles accelerated at distant sources and propagate in the galaxy through relatively weak magnetic fields, experiencing electromagnetic and nuclear interactions with photons and nuclear matter in the interstellar medium. Approaching the heliosphere they interact with the fields carried by the solar wind, which effectively modify their flux intensity up to energies of several GeV. Cosmic rays of the highest energy are considered by some authors to have an extra-galactic origin. Galactic cosmic rays are composed mostly of fully ionized nuclei H ($\sim$85%), He ($\sim$12%), heavier nuclei ($\sim$1%) and a small component of electrons ($\sim$2%). There is also a small contribution of the order of 0.1% of positrons and antiprotons which are likely to be produced in secondary reactions with the interstellar medium.

The energy dependence of the differential flux for a given nuclear specie i is well described at high energies by a power law:

$$\Phi(E_k) = K_i E_k^{-\gamma_i} \tag{47}$$

where E_k is the kinetic energy per nucleon, K_i is a normalization factor, and γ_i is the spectral index. Values of the spectral index in the range 2.5 - 3.1 have been observed for the different nuclear species composing the cosmic rays flux.

FLUKA takes into account the Galactic Cosmic Rays (GCR) component of the cosmic rays flux and allows a reliable simulation up to 10000-30000 GeV/nucleon. In the present version of the package, the primary flux is treated as a sum of nucleons (all-nucleon spectrum). The all-nucleon spectrum is obtained from the primary spectra derived from the NASA code (HIZ) [134] which considers all elemental groups from Z=1 to Z=28. In this case, the auxiliary files for input can be produced asking for a given solar modulation (see the paragraph about solar modulation). Such a code was obtained considering an overall normalization of the proton flux derived in the middle 80's, which is now considered obsolete. The Webber compilation [135] was taken into account. At present this compilation is considered to be substantially wrong (see in the following). For this reason a user flag was introduced in the code, giving the user the possibility of modifying the most relevant components (p and He) to follow more recent data sets (AMS and BESS data of 1998) up to 100 GeV. The allowed values for this flag are 0, 1, 2, and 3. For the present study we consider the cases 0, 2 and 3, which represent respectively the original NASA Spectrum and their two different modifications (AMS-BESS fit 2001 and PrimaryCR fit 2005) according to the latest high accuracy measurements performed in the late 90's. In the next paragraph will be discussed with more details the status of the experimental measurement of primary GCR at the top of atmosphere. In Fig.46 we show the comparison of FLUKA spectra (continuous lines) obtained using the PrimaryCR fit 2005, for a few representative nuclei in comparison with different experimental data sets.

The uncertainty on the primary flux has been the object of intense debate in the last years, mostly because of its implication in the calculation of secondary particles in the atmosphere and in particular for neutrinos. As pointed out in [136], the most relevant problem came from the $\sim$50% discrepancy in the proton flux between the previously quoted compilation of Webber [135] and the results from LEAP [137]. Historically, the highest normalization proposed by Webber et al. was taken as reference to explain the muon data

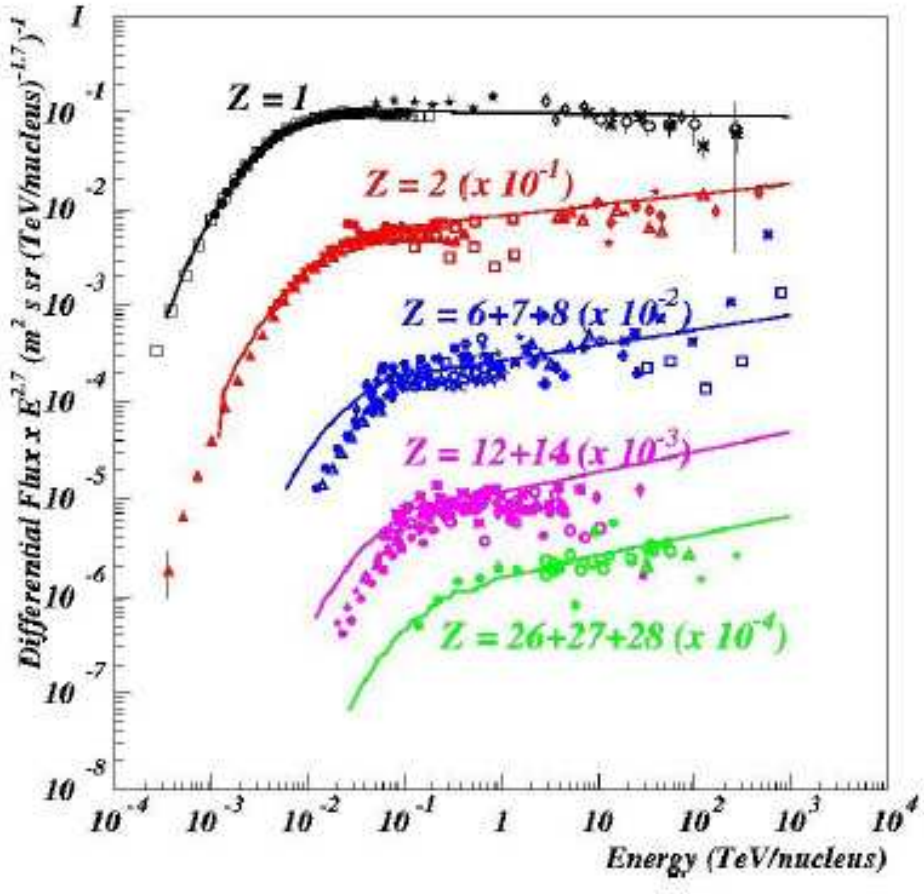

Figure 46: FLUKA calculations of the GCR fluxes (continuous lines) compared with different experimental data sets.

collected at ground level by Allkofer et al. [138] (published in 1971) and later by Rastin [139] (appeared 1984), together with the data taken in the high atmosphere from MASS [140]. New data on atmospheric muons [141, 142, 143] showed that important differences could exist with respect to the first sets.

Since the late 90's there have been new measurements of the primary flux by means of magnetic spectrometers such as IMAX [144], CAPRICE [145, 146] and MASS2 [147], mostly concerning the proton and helium flux and also including some measurement of higher mass primaries.
Our knowledge of the flux has improved dramatically in recent years. The most

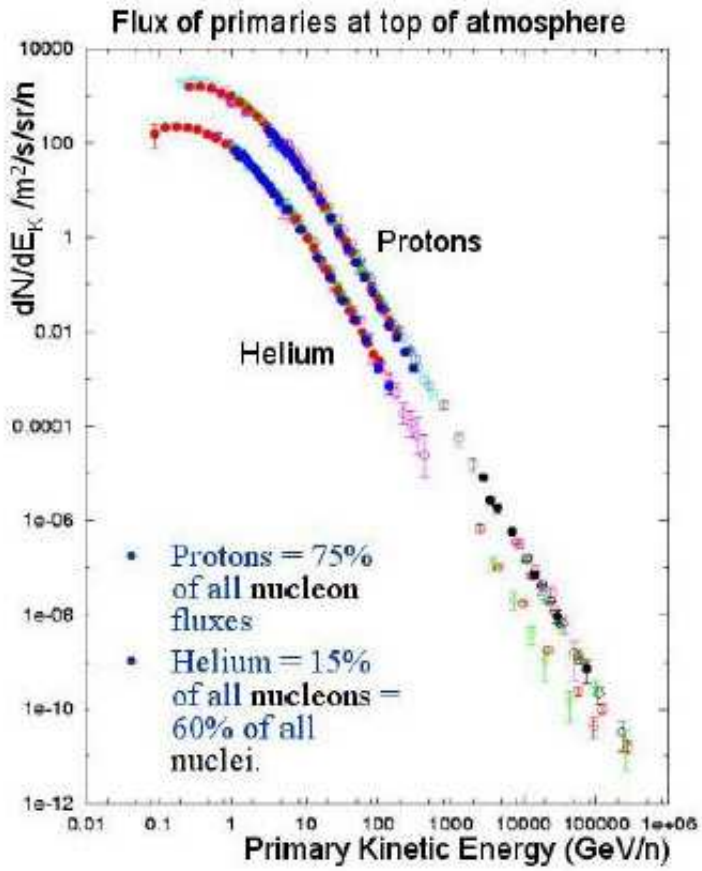

Figure 47: Compilation of recent measurements of the proton and He components of GCR flux at the top of the atmosphere.

recent measurements of protons with AMS [148] (running in the Space Shuttle) and BESS [149] have relatively small uncertainties and are in very good agreement with each other (to within 5%). The AMS and BESS experiments have also measured the Helium flux [150, 151]. In this case the results show a 10% discrepancy when plotted as a function of rigidity. Measurements of the most abundant components of cosmic rays with Z>3 were obtained mostly by the HEAO3 [152] and CRN [153] detectors (both on satellites).
This is the situation up to the 100 GeV region. At energies exceeding 1 TeV there are the data from the balloon-borne calorimetric measurements of JACEE [154], RUNJOB [155] and other experiments [156, 157], mostly based

$$\phi(E_K) = K\left(E_K + b\exp\left[-c\sqrt{E_K}\right]\right)^{\alpha}$$

	α	K	b	c
H	2.74	14900	2.15	0.21
He	2.64	600	1.25	0.14
CNO 14	2.70	62.4	1.78	0.02
Ne-Si 24	2.70	21.4	1.78	0.02
Fe(56)	2.70	5.1	1.78	0.02

Figure 48: Functional form and parameters of the fit of all-nucleon spectrum of GCR (at solar minimum) proposed in 2001 by the Bartol group.

on the emulsion technique. Some of these have the capability of separating different mass components. These calorimetric experiments do not capture all the energy of the primary, and as a consequence, the energy determination is not as precise as with a spectrometer. In particular JACEE and RUNJOB derive the primary energy by the detection of the showers originating by the electromagnetic component produced by the primary interaction. The link between the electro-magnetic component and primary energy is necessarily based on a model of the interaction and therefore it is also improper to consider these measurements as "direct" measurements. RUNJOB has been working for about ten years and its last flight was completed in 2003.

However, these calorimetric detectors give results which are consistent with each other: for the proton γ_p ∼2.8 and for the medium-heavy elements spectra $\gamma_{CNO} \sim \gamma_{Fe}$ ∼2.5 to 2.6, while they do not agree for helium ($\gamma_{He} \sim \gamma_p$ for RUNJOB, while $\gamma_{He} \sim \gamma_{CNO-Fe}$ for JACEE). Given the exposure of these experiments and considering the steepness of the flux, it is clear that the relative uncertainties of data collected at these energies are much larger than those achieved in the data sets below 100 GeV by the other quoted experiments.

In 2001 the Bartol group proposed a new fit to the all nucleon flux [158] to be used as reference for the calculation of secondary particles in atmosphere.

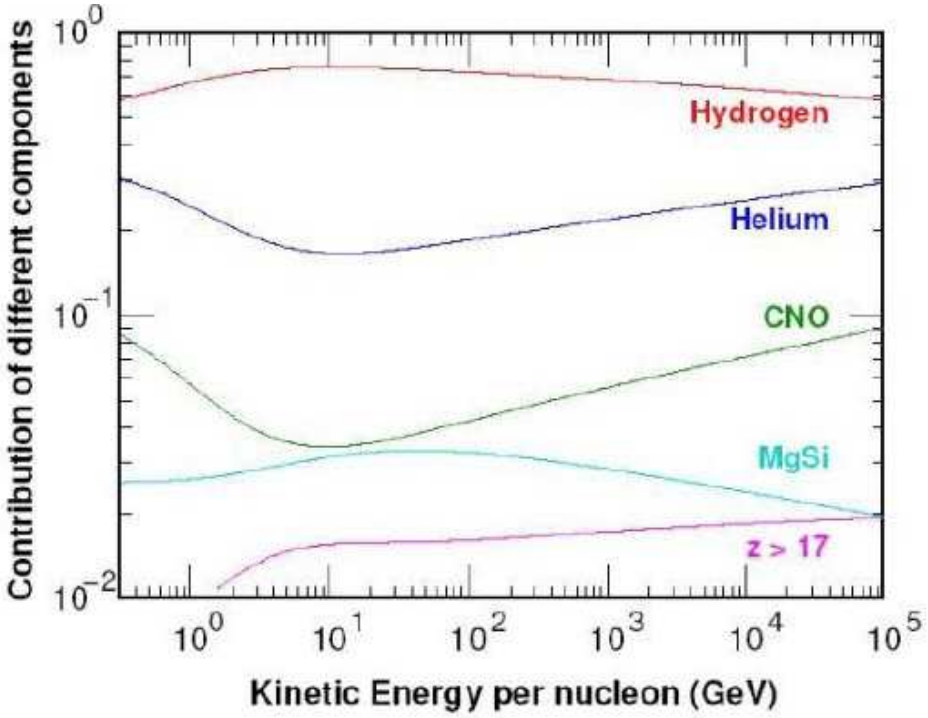

Figure 49: Fraction of the different mass components as a function of energy in the all-nucleon GCR 2001 fit of the Bartol group.

This fit (considering the grouping of all masses into 5 groups) is strongly constrained by the high statistics results of AMS and BESS measurements on the proton and helium components. The fit also proposed a smooth connection to the higher energy data collected by JACEE and RUNJOB. However, this fit does not take into account the results on primary protons of CAPRICE, which is in the same energy region as the AMS and BESS measurements, are about 25% lower. This discrepancy still remains unresolved and constitutes probably one of the most important contributions to the total systematic error in the knowledge of the GCR flux at the top of the atmosphere.
Very recently new data have been taken by BESS [159] (up to 500 GeV/nucleon) and by the ATIC experiment [160] which presented preliminary data on the proton and helium spectrum, filling the gap between the region explored by AMS, BESS and CAPRICE and that covered by JACEE and RUNJOB. However, so far only preliminary presentations are available for ATIC data, so the question cannot yet be settled.

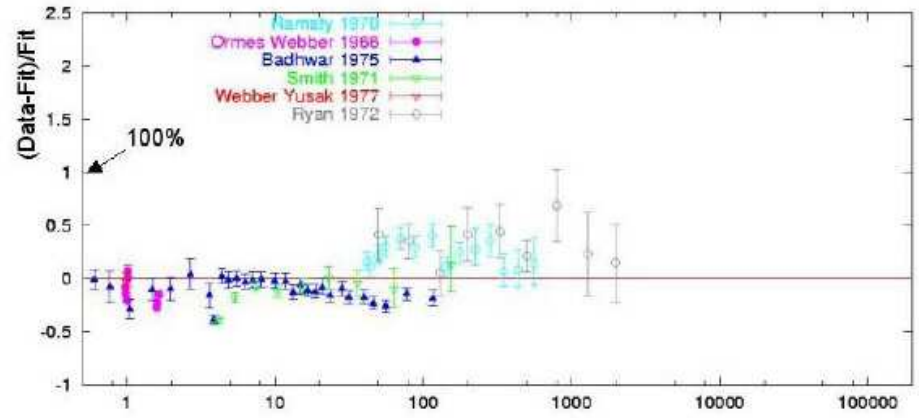

Figure 50: Residuals of the Bartol fit to experimental data for the proton component: the oldest measurements.

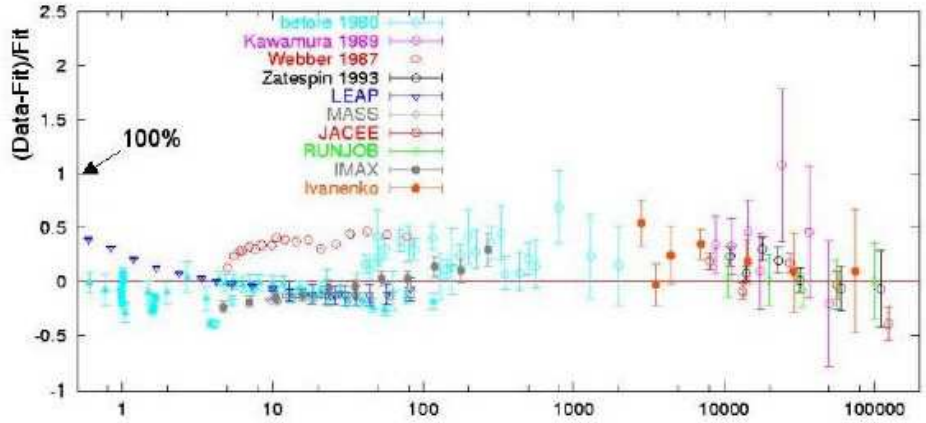

Figure 51: Residuals of the Bartol fit to experimental data for the proton component: measurements in the first half of 90's.

In Fig.47 we show the collection of the recent measurements of the proton and helium components (which are dominant for the problem of radiation doses in the atmosphere) with the exclusion of the most recent measurements from ATIC and BESS.
The Bartol fit of 2001 is what we have used to modify the NASA fluxes when

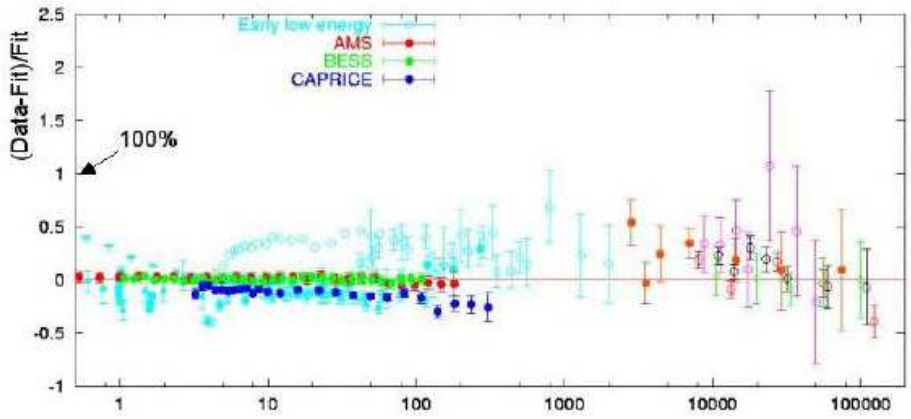

Figure 52: Residuals of the Bartol fit to experimental data for the proton component: the latest measurements are included.

the modification flag 2 and 3 are invoked (AMS-BESS fit 2001 and PrimaryCR fit 2005 respectively). The functional form fit of ref. [159] is shown in Fig.48 together with the parameters for all the 5 mass groups (evaluated at solar minimum).
The relative contributions of all mass groups as a function of energy are shown in Fig.49.

In order to understand the quality of the fit, in Figs. 50, 51 and 52 we show the residuals with respect to the experimental data for protons. Fig.50 shows the comparison with data taken until 1975, while Fig.51 includes all relevant contributions until the middle of '90s. Of particular relevance are the points of the Webber compilation: as previously mentioned they have been considered as reference data for a while, including the original NASA files used in FLUKA (NASA Spectrum). The present understanding, in the light of the most recent measurements, is that this compilation is substantially wrong. This is corroborated in Fig.52, where the latest measurements are included.

In summary, the latest measurements are, at least qualitatively, in agreement between each other and confirm the lower normalization of the LEAP experiment, with the only exception of the even lower normalization of the CAPRICE results (confirming their earlier measurements of 1994). Differences at low energy can be explained in terms of cutoffs and solar modulation. Therefore,

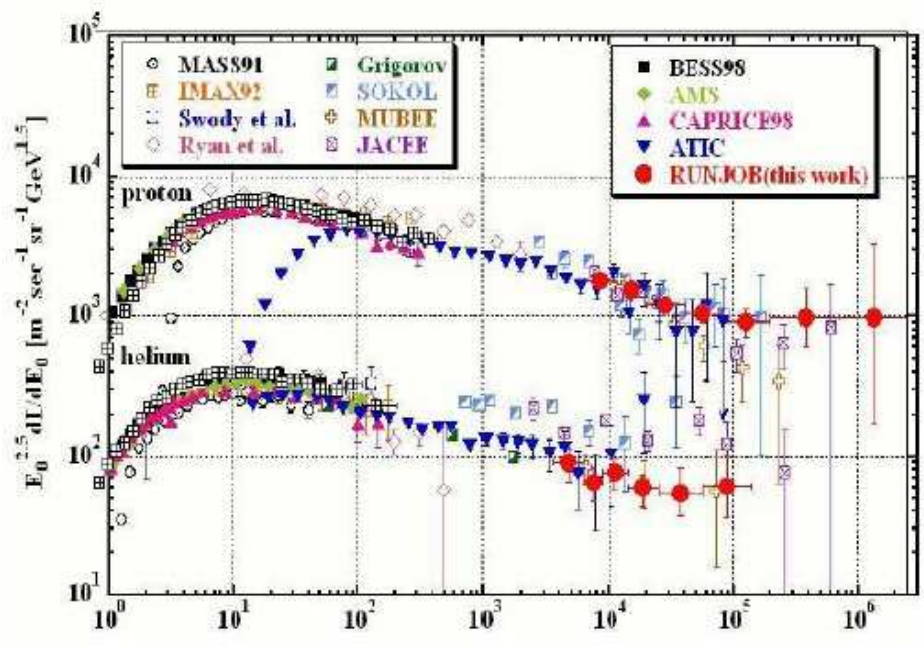

Figure 53: GCR measurements at the top of the atmosphere for the proton and He components. The RUNJOB measurements are put in evidence.

from these plots we can conclude that the present uncertainties in the region below 100 GeV, where the statistical error is now small, are due to the systematic discrepancy between the data sets of CAPRICE (which are lower by a 25% factor) and those of AMS and BESS. At present there is no unbiased way to understand this ambiguity, which is likely due to systematic errors. In any case the conclusion is that the scientific community is brought to discard the early compilation of Webber, and the primary flux below few hundreds of GeV is now determined with an uncertainty ranging from 10% to 25% depending on the inclusion of CAPRICE data. However, it can be noticed how the CAPRICE data tend to follow a steeper spectrum with respect to the behavior of the AMS and BESS data set, and this would give some trouble in the extrapolation to the higher energies if a monotonic power law is expected to represent the cosmic ray spectrum below 10^{15} eV.
As far as these higher energies are concerned, the situation is less clear both from the statistical and systematic point of view in the region above 1 TeV. This is mainly due to the difference between the JACEE and RUNJOB data sets. In Fig.53 we show, in a different representation, the proton and Helium

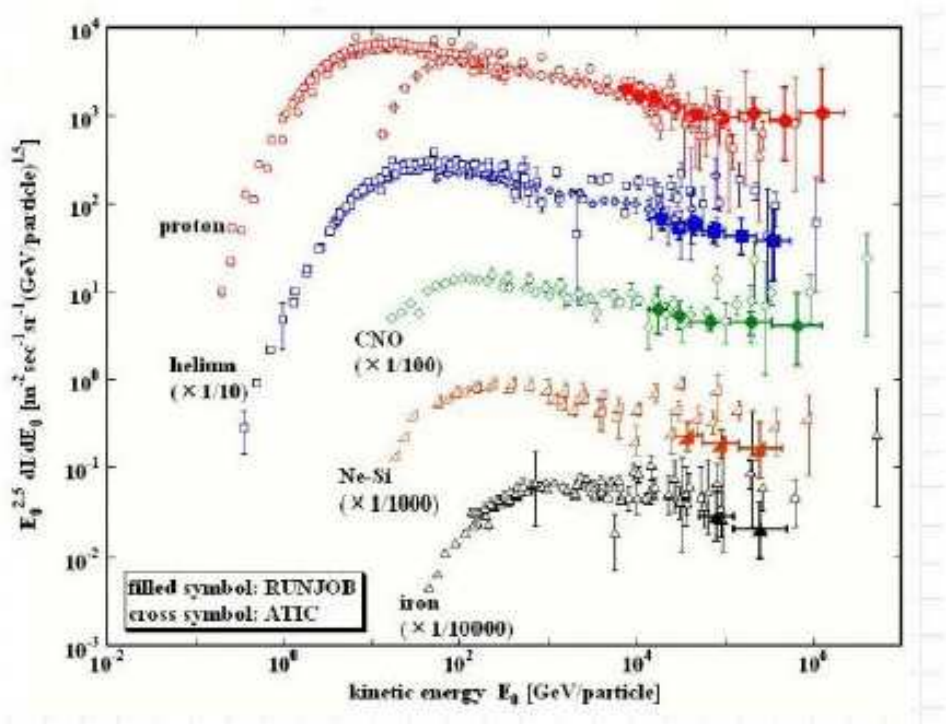

Figure 54: GCR measurements at the top of the atmosphere for different mass components. The RUNJOB measurements are put in evidence.

data up to highest energy measured by RUNJOB (the preliminary ATIC data are also shown, with a normalization arbitrarily matched to the AMS/BESS results at low energy). It can be seen how the main difference between this data set and the one of JACEE is the Helium component.

Fig.54 instead shows the whole data set, as compared to other measurements, including the higher mass components.

In Fig.55 we show the uncertainty associated to the extrapolation at high energy of the low-energy sector. It can be noticed in this plot how most of the high energy proton data stay above the extrapolation of the proposed fit. There are however indirect analysis at high energy on secondary muons and neutrinos [163] that show some preference for a higher normalization of the all-nucleon flux.
In order to have a better understanding of the connection between the energy

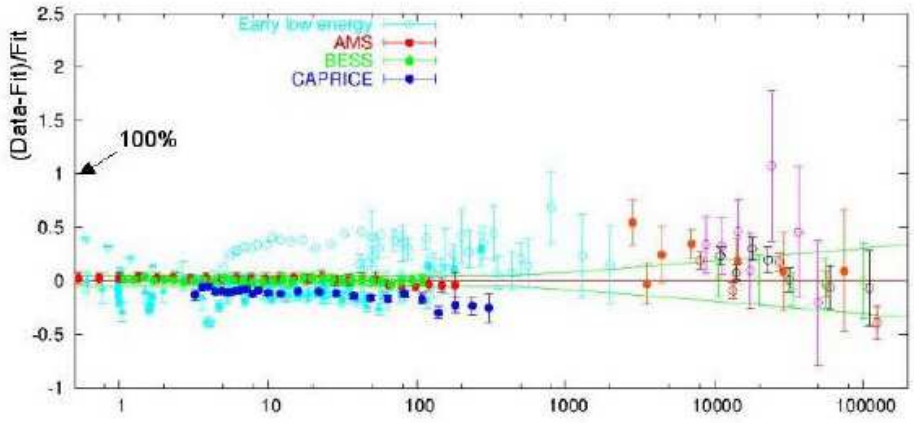

Figure 55: The uncertainty band of the proposed Bartol fit in the multi-TeV region for the proton component.

region below 100 GeV and the multi-TeV spectrum we have used the ATIC data, as shown in the next paragraph.

A new primary spectrum: the High Energy All-nucleon Spectrum

In ICRC 2005 a new primary spectrum [133] (**fit 2004**) was proposed to solve a deficit of the previous (2001) FLUKA calculation [164] in high energy (∼100 GeV) neutrinos.
The new spectrum has been calculated using the so called ICRC2001 fit [166] up to 100 GeV. For the proton component at energies larger than 100 GeV, using the normalization obtained at 100 GeV, was assumed a spectral index of γ =-2.71 to improve the agreement between the predicted fluxes and the MACRO and Super-Kamiokande throughgoing muon data [167]. Above the knee at 3000 TeV a spectral index of γ =-3.11 was assumed.
For what concerns the He component, above 100 GeV γ = -2.59 was used and a charge dependent knee has been assumed according to the rule: $E_{nucleon} = Z * 3000 TeV/A$. Higher Z components have been grouped in CNO, MgSi and Fe sets and treated using an all-particle spectrum with the above cited charge dependent knee parametrization. The resulting all-particle spectrum is shown in Fig. 56 and compared with the ICRC2001 and previous Bartol 1996 [165] fits.
In Fig. 57 is shown the new High Energy All-nucleon Spectrum. In the

following are shown comparisons between the new High Energy All-nucleon Spectrum with the other lower energy options: the old NASA Spectrum (Fig. 58) and the two new different fits to recent measurements (AMS-BESS fit 2001 and PrimaryCR fit 2005) (Figs. 59,60).

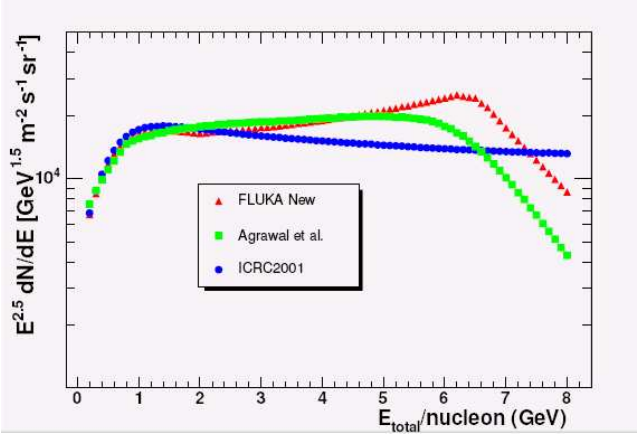

Figure 56: The new all nucleon primary spectrum (**High Energy All-nucleon Spectrum**) adopted for this work compared to the ICRC2001 [166] and the Bartol 1996 [165] ones.

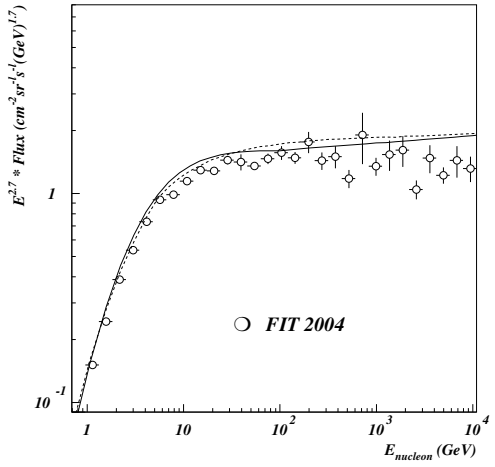

Figure 57: The new High Energy All-nucleon Spectrum (fit 2004) at the top of the atmosphere (open symbols), the 2001 fit (dashed line) and the High Energy All-nucleon Spectrum (fit 2004) (solid line).

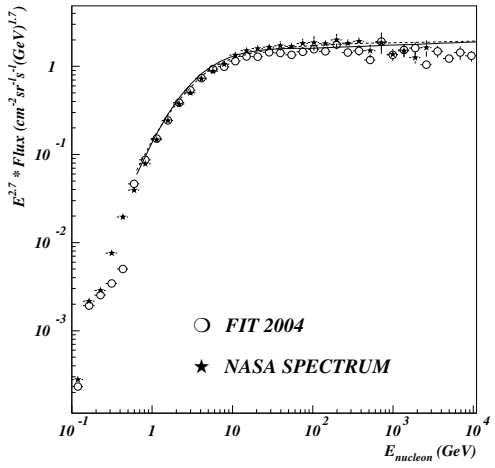

Figure 58: The old NASA spectrum (stars) in comparison with the new High Energy All-nucleon Spectrum (fit 2004) at the top of the atmosphere (open symbols), the 2001 fit (dashed line) and the High Energy All-nucleon Spectrum (fit 2004) (solid line).

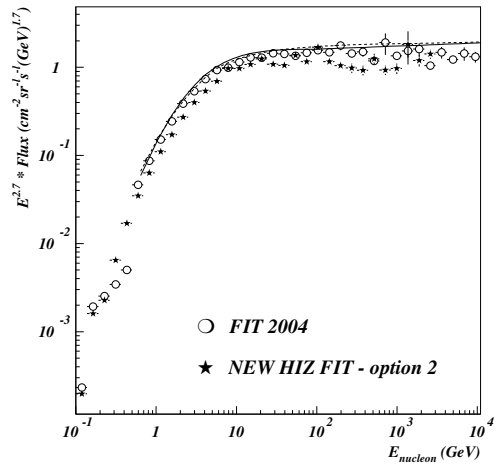

Figure 59: The AMS-BESS fit 2001 (new HIZ fit, option 2) (stars), in comparison with the new High Energy All-nucleon Spectrum (fit 2004) at the top of the atmosphere (open symbols), the 2001 fit (dashed line) and the High Energy All-nucleon Spectrum (fit 2004) (solid line).

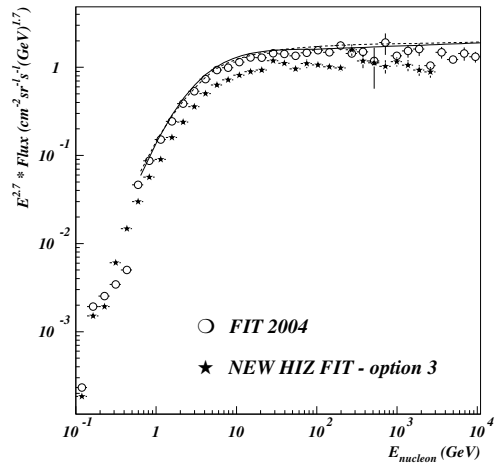

Figure 60: The PrimaryCR fit 2005 (new HIZ fit, option 3) (stars), in comparison with the new High Energy All-nucleon Spectrum (fit 2004) at the top of the atmosphere (open symbols), the 2001 fit (dashed line) and the High Energy All-nucleon Spectrum (fit 2004) (solid line).

3.3.2 Solar modulation

The deviation from the power law, observed below 10 GeV, is a consequence of the already cited influence of the solar wind called solar modulation [187]. Flux intensity in this energy range is anti-correlated to the solar activity and it follows the sun-spot 11-years cycle. The correlation between the solar activity and the modulation of the cosmic rays flux has been studied by the monitoring of the flux of atmospheric neutrons. In fact, a flux of low energy neutrons (E $\sim 10^8 - 10^9$ eV) is produced in the interaction of primary CRs with the atmosphere and it is mostly due to low energy primaries (1 - 20 GeV), due to the rapid fall of the primary flux intensity with energy.
One assumes that far from the solar system there exists an unmodified flux called *Local Interstellar Spectrum* which is modified within the solar system by the interaction with the solar wind. This interaction is well described by the Fokker-Planck diffusion equation. Let us describe the solar wind by a set of magnetic irregularities. If we consider these irregularities as perfect elastic scattering centres, we can obtain the Fokker-Planck diffusion equation. For energies above 100 MeV this equation can be solved using the "Force Field Approximation" [194]. According to this approximation, at a given distance from the Sun, for example at 1 a.u., the population of CRs at energy $E_{interstellar}$ is shifted at the energy $E_{\oplus}$ as in an energy loss mechanism due to a potential V.

$$E_{\oplus} = E_{interstellar} + Z \cdot V_{solarwind}(t) \tag{48}$$

The solar wind potential at a given distance from the Sun depends on only one parameter (time): $V = V(t)$. So we don't mind which the interstellar flux is: given a flux on the earth at a time t, we can find the flux at another time just from the relative variation of the solar wind potential. We can derive this variation from the neutron monitor counts [181].
In the case of the NASA spectrum and of the more recent fits, the HIZ code makes use of an algorithm [181] which takes into account the counting rate of the CLIMAX neutron monitor [182] to provide the prediction for the flux of a specific date or for a given value of the potential which express the effect of the interplanetary modulation of the local interstellar spectrum (Fig. 61). This monitor is extended up to the last years [Figs. 62,63].

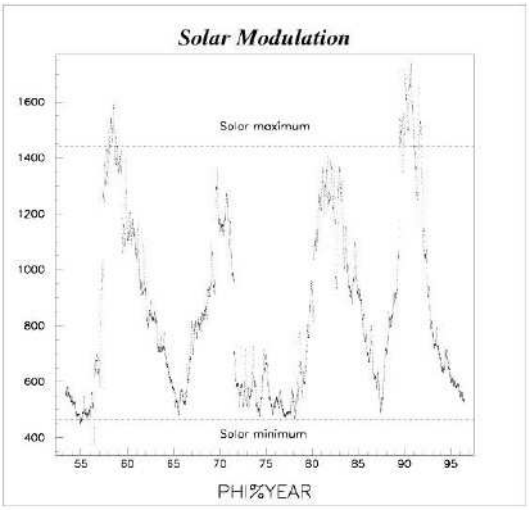

Figure 61: Cosmic rays intensity variation (neutron counts) anti-correlated with the eleven-years sun spot cycle.

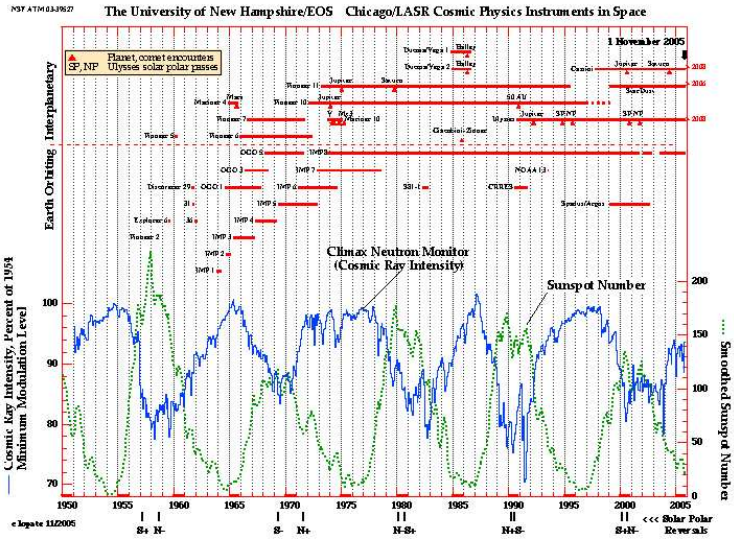

Figure 62: CLIMAX neutron monitor

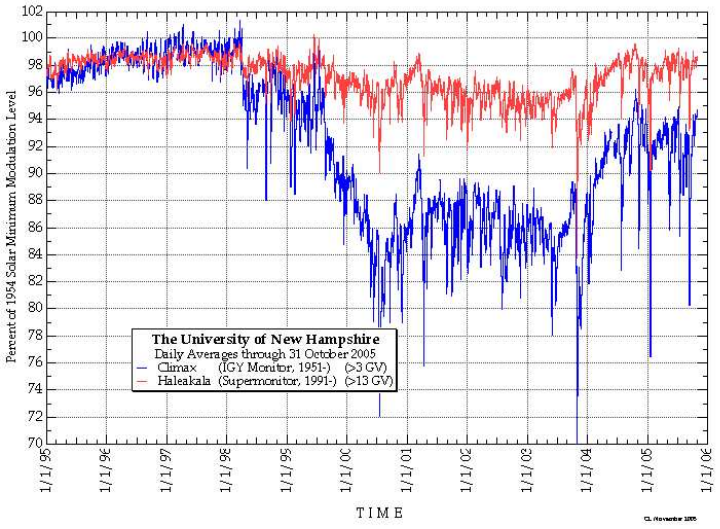

Figure 63: CLIMAX neutron monitor. From 1995 to 2004.

3.3.3 Atmospheric model: geometry and density

The **geometrical setup** is a 3-Dimensional spherical representation of the whole Earth and of the surrounding atmosphere (Fig. 64). This is described by a medium composed by a proper mixture of N, O and Ar, arranged in 100 concentric shells, extending up to about 70 km of altitude (Fig. 65) and cut by a truncated cone centered on the geographical location.

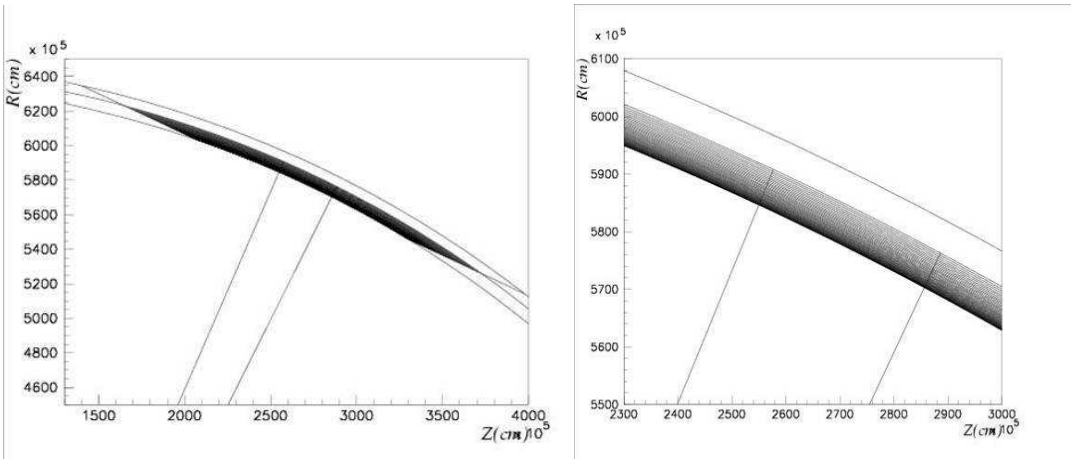

Figure 64: Atmospheric geometrical setup.

The geometry is built using two cones (in reality they are truncated cones in the code) whose vertex is in the centre of the Earth, the base is out of the atmosphere and the altitude (if we consider a geographical location in the northern hemisphere) is in the direction of the Earth radius which passes through the North Pole. The angular span of the two cones holds the atmosphere of interest for the geographical location under examination. In addition there is a third cone placed in the opposite direction: the vertex is where the other two cones have the base, the base is out of the atmosphere and the altitude is in the direction of the Earth radius which passes through the South Pole. So the complete geometry is made from:

- a main series of layers made from the part of the atmospheric shells among the two cones (this is the part where the scoring takes place),
- two series of side-layers made from the part of the atmospheric shells among one of the two cones and the third ones. We need these additional layers to take into account the primary and secondary particles which

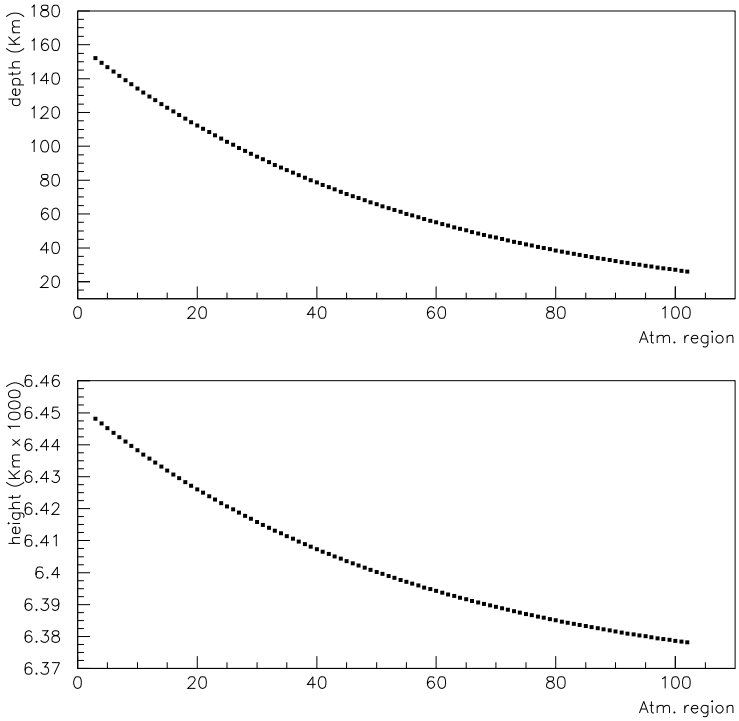

Figure 65: Atmospheric regions thickness (upper figure) and distance from the centre of the Earth (lower figure).

don't come from the vertical direction but can anyway reach the region of interest.

The Fluka package makes use of a height-density profile of atmosphere. An external program (atmocdnw.f) containing a functional fit to this profile allows the user to generate at the same time the input geometry file for FLUKA, together with the data cards for material description (each atmospheric layer, having its proper density, is in practice a different FLUKA material). The same program also generates the tabulation of the electromagnetic cross sections for FLUKA (the 'pemf' file). The generation of geometry and material files by means of an external program allows including different atmospheric profiles, in order to reproduce the expected conditions at different latitudes or at different seasons during the year.

Atmospheric Models

The atmosphere can roughly be characterized as the region from sea level to about 1000 km altitude around the globe, where neutral gases can be detected. Below 50 km the atmosphere can be assumed to be homogeneously mixed and can be treated as a perfect gas. Above 80 km the hydrostatic equilibrium gradually breaks down as diffusion and vertical transport become important.
In this work I have compared two different atmospheric **density** profiles: the U.S. Standard Atmosphere 1976 and the NRLMSISE-00 Model 2001 [169].
The **U.S. Standard Atmosphere 1976** is based on rocket and satellite data and perfect gas theory. The atmospheric densities and temperatures are represented from sea level to 1000 km of altitude. The U.S. Standard Atmosphere 1976 consist of single profiles representing the idealized, steady-state atmosphere for moderate solar activity.
In the **NRLMSISE-00 Model 2001** the Mass-Spectrometer-Incoherent-Scatter (MSIS) empirical model allows including different atmospheric profiles, in order to reproduce the expected conditions at different latitudes or at different seasons during the year.
Data sources include measurements from several rockets, satellites (OGO 6, San Marco 3, AEROS-A, AE-C, AE-D, AE-E, ESRO 4, and DE 2), and incoherent scatter radars (Millstone Hill, St. Santin, Arecibo, Jicamarca, and Malvern).
Below 72.5 km the model is primarily based on the MAP Handbook tabulation of zonal average temperature and pressure by Barnett and Corney [170]. Below 20 km these data were supplemented with averages from the National Meteorological Center (NMC). Above 72.5 km the model takes into account data derived from space shuttle flights.

In Fig. 66-69 there is a comparison between the two models. In particular is shown the atmospheric thickness and density ratio of the NRLMSISE-00 Model on the U.S. Standard Atmosphere for different years and location from sea level up to 70 Km of altitude.
The difference between the two models below 50-60 Km of altitude is $< 10 - 15\%$ both for density and depht in atmosphere.

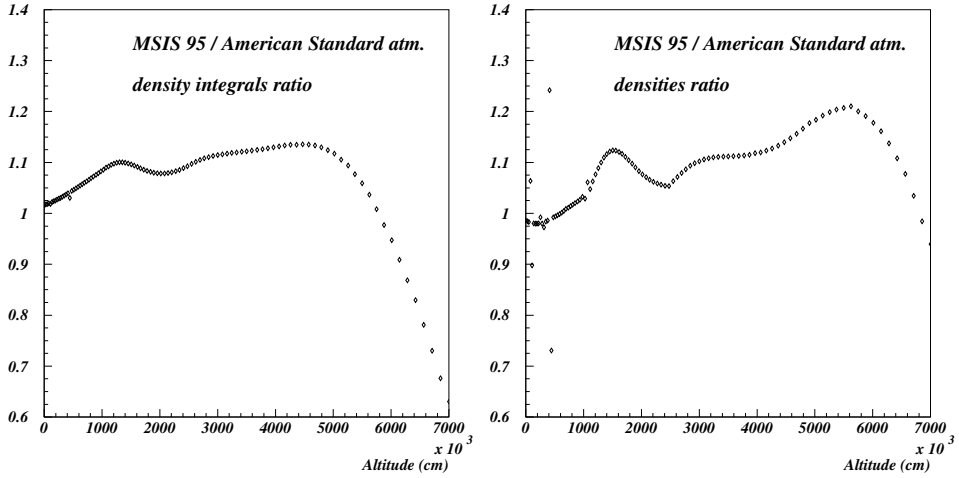

Figure 66: NRLMSISE-00 model on American Standard atmospheric thickness and density ratio. From sea level up to 70 Km of altitude. Year 1995 at Tsukuba (Japan).

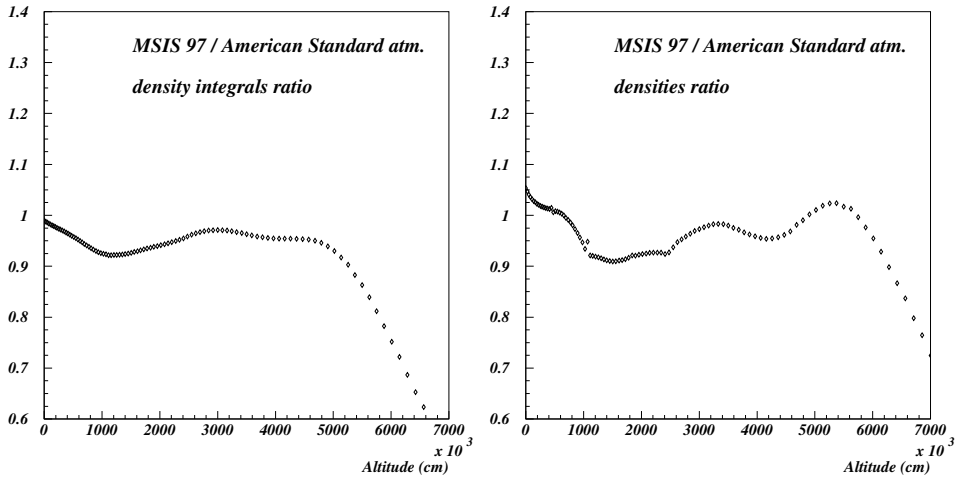

Figure 67: NRLMSISE-00 model on American Standard atmospheric thickness and density ratio. From sea level up to 70 Km of altitude. Year 1997 at Lynn Lake (Canada).

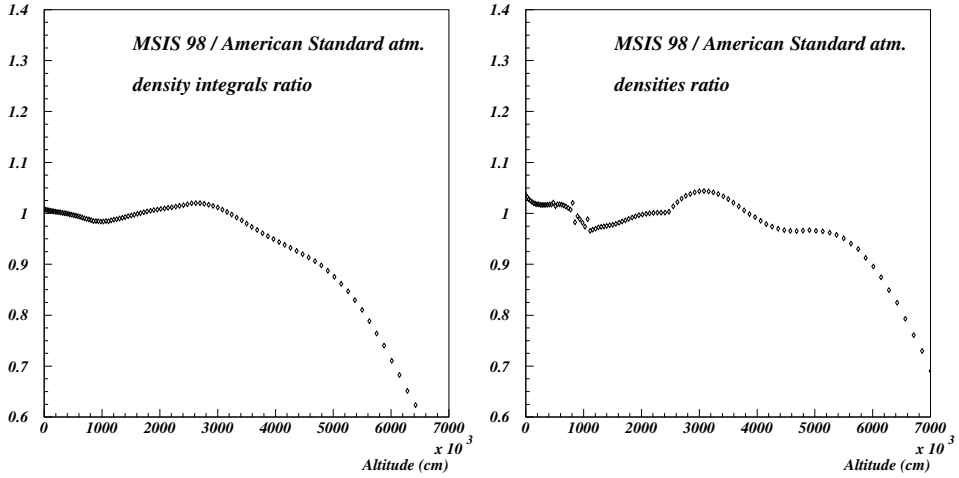

Figure 68: NRLMSISE-00 model on American Standard atmospheric thickness and density ratio. From sea level up to 70 Km of altitude. Year 1998 at Lynn Lake (Canada).

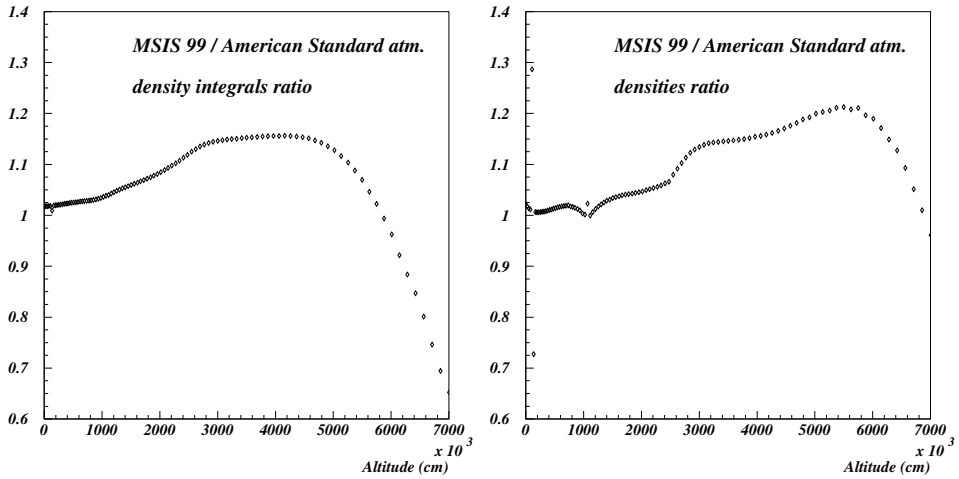

Figure 69: NRLMSISE-00 model on American Standard atmospheric thickness and density ratio. From sea level up to 70 Km of altitude. Year 1999 at Lynn Lake (Canada).

3.3.4 Geomagnetic field

In the last 50 years measurements of the geomagnetic field configuration have been performed regularly with increasing precision, revealing a yearly weakening of the field intensity of 0.07% and a westward drift of $\sim 0.2°/year$ over the Earth 's surface.

This field can be described, at first order, as a magnetic dipole tilted with respect the rotation axis of $\sim 11.5°$, displaced by $\approx 400Km$ with respect the Earth's center and with a magnetic moment $M = 8.1 \times 10^{25} Gcm^3$. The dipole orientation is such that the magnetic south pole is located near the geographic north pole, in the Greenland, at a latitude 75° N and longitude 291°. The magnetic north pole is instead near the geographic south pole, on the border of the Antarctica. Fig. 70 shows the field map at the Earth surface. The intensity at the Earth's surface varies from a maximum of ~ 0.6 G near the magnetic poles to a minimum of ~ 0.2 G in the region of the South Atlantic Anomaly (SAA), in between Brazil and South Africa. The complex behavior of the equipotential field lines is mainly a consequence of the offset and tilt.

The geomagnetic coordinates

The simplest description of a purely dipolar field is obtained in cylindrical coordinates referred to the system defined in Fig. 71. The components of the field are:

$$B_r = -\frac{M}{r^3} 2 sin\lambda \quad ; \quad B_\lambda = \frac{M}{r^3} cos\lambda \tag{49}$$

and the field lines have the form:

$$r = r_0 cos^2\lambda \tag{50}$$

The B intensity along each field line is expressed as:

$$B(\lambda) = \frac{M}{r_0^3} \frac{[4 - 3cos^2\lambda]^{1/2}}{cos^6\lambda} \tag{51}$$

It reaches its minimum value $B_0 = M/r_0^3$ on the equatorial plane ($\lambda = 0$) at the largest distance from the dipole centre $r = r_0$. This equatorial radius r_0 of the field line is often expressed in units of Earth Radii (R_E), introducing the dimensionless parameter $R_0 = r_0/R_E$. The intersection of a field line with parameter R_0 with a sphere of radius R_E centered in the origin of the dipole

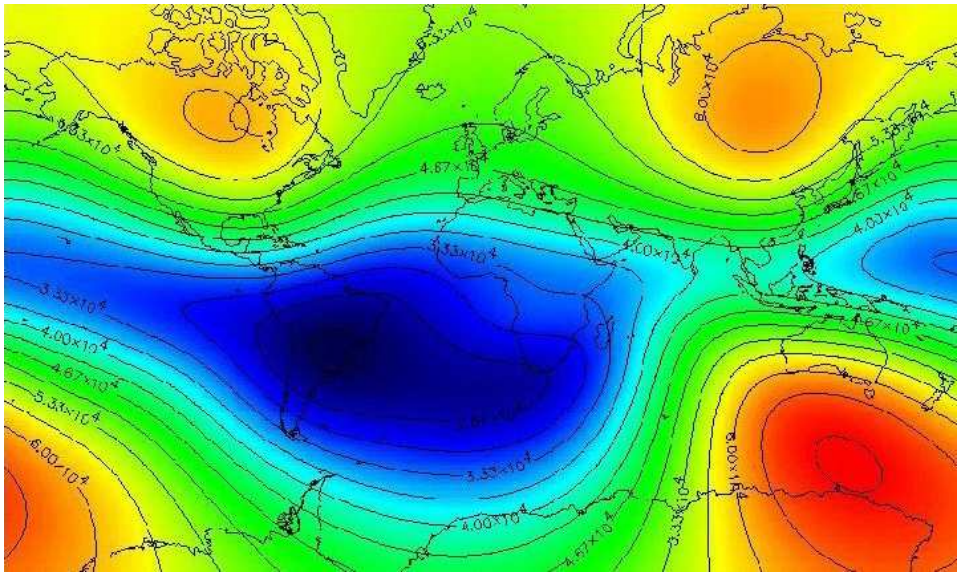

Figure 70: Geomagnetic field map on Earth's surface, Mercatore projection. Field values are expressed in nT for 1998 epoch.

Figure 71: Geomagnetic spherical coordinates and dipolar field line structure.

is simply given by:

$$cos^2\lambda = \frac{R_E}{r_0} = \frac{1}{R_0} \tag{52}$$

R_0 completely determines the field line and can be used as an independent parameter to characterize the dipolar field.

The geomagnetic cutoff

Experimental evidence for a modulation of the cosmic ray flux as a function of the geomagnetic latitude dates to the '30s. Qualitatively, the effect is easily understood when considering the B field line configuration with respect to a geocentered spherical surface. At the magnetic equator, the B field lines run nearly parallel to the spherical surface, while at the poles they encounter the surface at nearly normal incidence. In the polar region, low energy charged particles can therefore reach the surface following the field lines, while in the equatorial region the same particles would be deflected by the Lorentz force. In particular, above 78° in geomagnetic latitude, geomagnetic field lines are connected with the magnetopause region and the geomagnetic cutoff effect disappears. In these conditions low energy solar wind particles reach the Earth atmosphere and form the aurora Borealis.

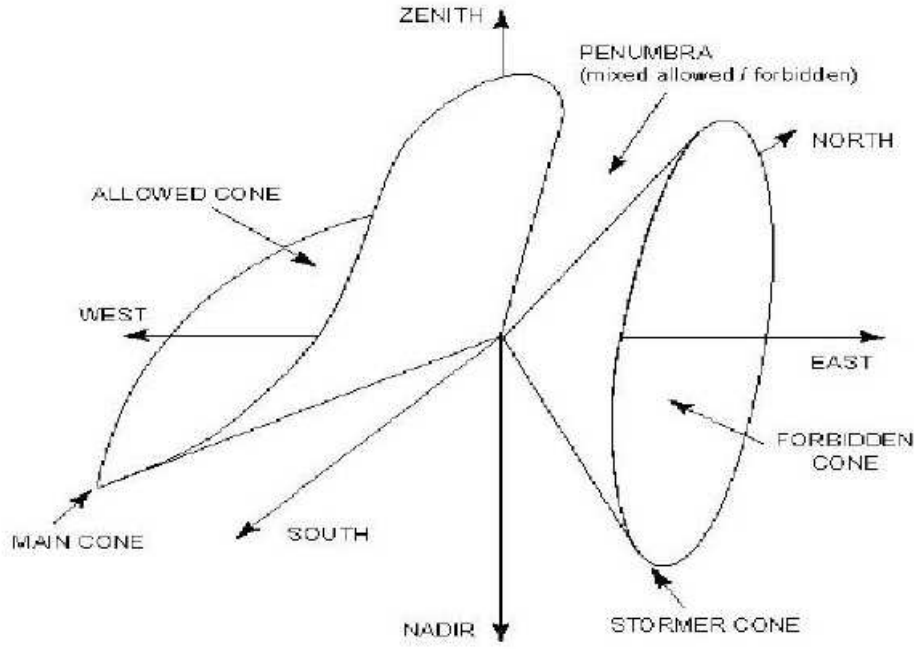

Figure 72: Representation of the full, partial and no access regions in a generic point of the geomagnetic field for a positively charged particle with an arbitrary rigidity.

Quantitatively, the question of charged particle access to a given location

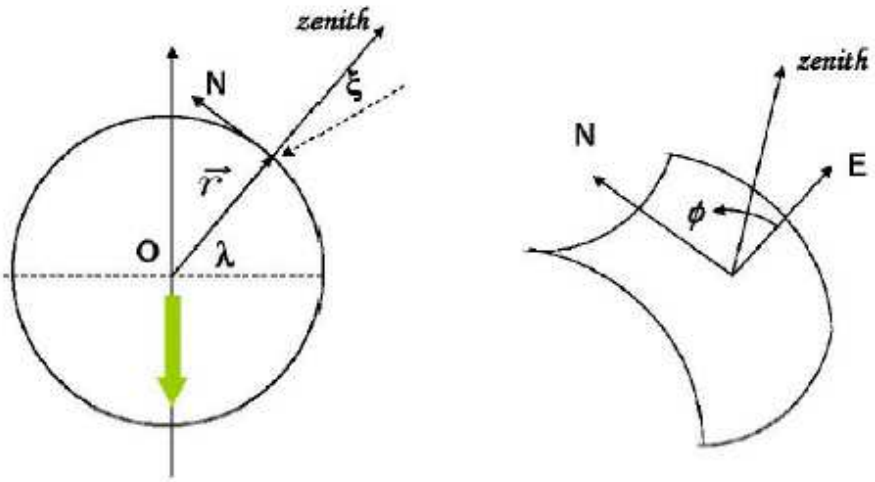

Figure 73: Definition of the spherical geomagnetic coordinates (r,λ) and of the local geomagnetic reference system (East, North, Zenith). The arrival direction of a particle in a point P is described by the polar angle ξ to the zenith and the azimuthal angle ϕ with respect local East.

coming from infinity can be formulated either in a *direction* or in a *rigidity* picture. In the first case, the access of a particle with a specific rigidity is studied as a function of its direction of arrival. A complementary study, i.e. the access along a specific direction as a function of the rigidity of the particle, is the basis of the second approach.

The peculiar result of the *direction* picture in a dipolar field is a net separation of the whole solid angle around any given location of the field in three separate regions characterized by full, partial and no access. This is better explained with the help of Fig. 72 relative to a positive charged particle with an arbitrary rigidity value. The reference system (Fig. 73) has its origin in an arbitrary position of the field with a vertical axis along the zenith direction. The horizontal axis is defined perpendicular both to the zenith and the dipole axis, in the East-West direction with respect the local B field.

On the right side of the picture (Fig. 72), the *Störmer cone* defines the region of no access at that given point. A positively charged particle with that specific rigidity can not reach that point from infinity along any of the directions (*forbidden* trajectories) enclosed in the *Störmer* cone. The existence

of this cone is a general property of any axially symmetric field and, at any field location and for any particle rigidity, the axis of this cone lies in the E-W direction, opening to the East for positively charged particles and to the West for negatively charged ones.

On the left side of the picture, the *main cone* defines the angular region of full access. A positively charged particle with that specific rigidity can reach that point from infinity along all directions (*allowed* trajectories) enclosed in the main cone. Opposite as for the *Störmer* cone, the orientation and the effective shape of the main cone can significantly vary with the particle rigidity and the considered geomagnetic location.

A mix of allowed and forbidden trajectories corresponds to the directions out of the two cones: this is the *penumbra* region. There, only a partial access to the point is possible due to the presence of a solid earth which intercepts part of the trajectories corresponding to arrival directions outside the *Störmer* cone. In the penumbra, the possibility for a positively charged particle to enter the field in that location should be evaluated in each direction by the full integration of the corresponding trajectory.

The logical step towards a rigidity approach to the problem is done by considering how the above picture changes for different particle rigidities.

At a given location, the angular opening of the *Störmer* cone and the shape and orientation of the *main* cone are a function of the rigidity of the particle. For increasing values of the rigidity, the looser bending effect of the magnetic field naturally results in a widening of the region delimited by the main cone and in a reduction of the opening angle in the *Störmer* cone. For a given direction of arrival, there will exist a minimum value of the particle rigidity for which the *Störmer* cone opens up to include that direction. This rigidity value defines the *Störmer rigidity cutoff* (R_S): all particles with a rigidity $R < R_S$ are forbidden to enter the field along that given direction. Analytically, the *Störmer* cutoff can be evaluated from the relation:

$$R_S = \frac{M cos^4\lambda}{r^2[1 + (1 \mp cos^3\lambda cos\phi sin\xi)^{1/2}]^2} \tag{53}$$

where M represents the dipole moment, the arrival location is defined by the geomagnetic coordinates (r, λ) and the arrival direction is defined by ξ and ϕ, respectively the polar angle from local zenith and the azimuthal angle

counted clockwise from local magnetic East (Fig. 73). The $\mp$ sign applies to positively/negatively charged particles.

For vertical incidence ($\xi = 0$), the azimuthal dependence of the cutoff simply vanishes putting in evidence the cutoff behavior with latitude:

$$R_S = \frac{M cos^4\lambda}{4r^2} = \frac{59.9 cos^4\lambda}{4r^2} GV/c \tag{54}$$

where r is expressed in units of earth radii. The cutoff is maximum (minimum) at the magnetic equator (poles) with a ≈15 GV/c (null) value at the Earth's surface.

For an arbitrary ξ, the cutoff is larger for positively (negatively) charged particles arriving from eastern (western) direction. At low energies this breaks the isotropy of the incoming cosmic ray flux, which - depending on the charge sign of the particles - exhibits an East-West asymmetry.

With the *Störmer* cutoff we can exactly define the minimum rigidity needed to access a magnetic location along a given direction. However, due to the *penumbra*, nothing guarantees that above the *Störmer* rigidity the access is always granted.

In FLUKA we take into account the geomagnetic field in two different stages of the simulation chain.

1 Effect of geomagnetic cutoff which modulates the primary spectrum: at a given location (point of first interaction of primary particles) and for a given direction a threshold in energy exists. The closer the injection point is to the geomagnetic equator, the higher will be the energy threshold. A possibility offered to the user is to evaluate the geomagnetic cutoff making use of a dipolar field off-centered with respect the centre of the Earth. Under this (reasonable) approximation, an analytical calculation of the cutoff can be performed. A more accurate algorithm is obtainable using the technique of anti-proton "back-tracing" from the interaction point to the outer space. This allows taking into account the "penumbra" effects (this has been performed offline in the atmospheric neutrino production with FLUKA [177]). In this case the off-set dipole is no more a sufficient approximation and the spherical harmonic expansion like the IGRF model is more adequate [182].

2 The local geomagnetic field is taken into account during shower development. The field is provided to FLUKA by one of the user routines of the quoted library. For local problems it is essential to provide the correct orientation and magnitude of the field.

For our work it is assumed that a dipolar field off-centered with respect the centre of the Earth is a sufficient approximation to describe the shower development in atmosphere. Systematics related to the other component of this analysis are bigger with respect to the slight advantages given by the IGRF model.

Scoring

FLUKA allows defining user-detectors at each boundary crossing between regions, so to easily score the fluence from different radiation fields.

3.3.5 Example of Input data card

In Fig 74,75 is reported an example of user data card to drive the FLUKA executable including our cosmic ray library, with some comment on the relevant points. The example is relative to the simulation at the geographical coordinates of 56.5 degrees of North Latitude and -101.0 degrees of West Longitude, using the solar modulation of Aug. 8th 1994. For the explanation of each directive, the FLUKA user reference guide has to be consulted. The detailed explanation of the meaning of all parameters for the SOURCE and USRICALL directives is reported in the comments of *source.f* and *usrini.f* in the *nuatmmvax* library.

Analysis of results

The outputs of different runs from the FLUKA code can be summed by means of the standard codes available in the standard release. As far as the quoted example is concerned, the *usysuw* code is the proper one. The user can easily access the source code to prepare, if requested in its own output format, if necessary. This is particularly useful if a particular graphic output is requested.

```
TITLE
NASA flux at lat=+56.5, long=-101.0 on 8-aug-1994 (Caprice94)
DEFAULTS                                                              NEW-DEFA
BEAM        3.D+04                                                    PROTON
*
* In the following, the source from nuatmmvax is invoked. PINSKYFL is the
* option to generate nucleon with the NASA flux
* Maximum energy is 30000 GeV
*
SOURCE     28.0     6.499 D+08 0.3        30000.0  1.75      500.0    PINSKYFL
SOURCE     2.0       0.67                                              &
DISCARD    3.0       4.0       7.0       23.0
PHYSICS    2.0                                                       EVAPORAT
PHYSICS               0.3       0.3                                   RESTODPM
PHYSICS    1.0       1.0       1.0                                   COALESCE
PHYSICS    3.5       3.5                                             PEATHRES
DPM-PARA                                                            FLUKA975
BAMJET                                                              FLUKA975
*
* Next card calls the initializaion routine. The string 08AUG94 referes
* to the names of input files prepared by HIZ specifically considering
* the solar modulation of Aug 8th 1994
*
USRICALL   101000.0  0.0       0.0                           0.0      08AUG94
EVENTYPE                       1.0                                    EVAP
LAM-BIAS  -1000000.0                     10.0      39.0               GDECAY
LOW-BIAS   1.0                           1.0       500.0
*
* In the following the geometry file (specifically prepared for the
* required geographical coordinates) is invoked.
*
GEOBEGIN             0.1        53.0      54.0                        COMBINAT
56n101w.geo
56n101w.scr
GEOEND
*GEOEND    2.598544D8 0.0      5.679145D82.798544D8 0.0      5.879145D8DEBUG
*GEOEND     1000.0    1.0       1000.0                                  &
MATERIAL  7.0       14.007    0.001251  5.0                           NITROGEN
MATERIAL  8.0       15.999    0.001429  6.0                           OXYGEN
MATERIAL  18.0      39.948    0.00178   7.0                           ARGON
*
* Here the 100 different material specifications for all atmospheric layers
* follow
*
MATERIAL                       8.781E-08   8.0                        AIR001
COMPOUND  -.9256E-03   5.0    -.2837E-03   6.0    -.01572E-3   7.0    AIR001
MATERIAL                       1.036E-07   9.0                        AIR002
COMPOUND  -.9256E-03   5.0    -.2837E-03   6.0    -.01572E-3   7.0    AIR002
...
* Idem: Mat-prop cards:
MAT-PROP   7.168E-05                        8.0       8.0       1.0
MAT-PROP   8.453E-05                        9.0       9.0       1.0
MAT-PROP   3.026E-04                       17.0      17.0       1.0
...
* cards to Assign a different material to each region
ASSIGNMAT  8.0       1.0       103.0     102.0     1.
ASSIGNMAT  9.0       2.0       104.0     102.0     1.
ASSIGNMAT 10.0       3.0       105.0     102.0     1.
...
*  Internal Vacuum: black hole in this case
ASSIGNMAT   1.0     101.0                          0.0
*  External Vacuum
ASSIGNMAT   2.0     102.0                          1.0
```

Figure 74: Example of user data card.

```
*  Internal vacuum black hole:
ASSIGNMAT   1.0     203.0                          0.0
*  Atmospheric black hole:
ASSIGNMAT   1.0     204.0                          0.0
*  External black hole:
ASSIGNMAT   1.0     205.0                          0.0
ASSIGNMAT   1.0     206.0                          0.0
MAT-PROP    1.0                              8.0       8.0       1.0     USERDIRE
MGNFIELD    20.      100.       30.          0.0       0.0       0.0
*
PART-THR  -0.1000   1.0        16.0        1.0
DELTARAY  0.100                            8.0       107.0
ACCURACY  1.0       1.0
STEPSIZE  -10000.   100000.   1.0          206.0
PHYSICS   +1.                               1.0      39.0                DECAYS
*
* In this case the electro-magnetic simulation is switched off
*
EMF                                                                       EMF-OFF
OUTLEVEL   1.0       7.0
SCORE      208.0     210.0     201.0     229.0
*
* The following cards activate the scoring of double differential flux
* (energy * and angle) at the boundaries of each atmospheric layer
*
USRYIELD   2398.0    11.0     -21.0       1.0       2.0      1.0       0.09g/cm2
USRYIELD   200.0     0.2       30.0       8.0       0.0      6.0          &
USRYIELD   2398.0    11.0     -21.0       2.0       3.0      1.0       0.11g/cm2
USRYIELD   200.0     0.2       30.0       8.0       0.0      6.0          &
USRYIELD   2398.0    11.0     -21.0       3.0       4.0      1.0       0.13g/cm2
USRYIELD   200.0     0.2       30.0       8.0       0.0      6.0          &
...
USRYIELD   2398.0    11.0     -21.0      69.0      70.0      1.0       243.g/cm2
USRYIELD   200.0     0.2       30.0       8.0       0.0      6.0          &
USRYIELD   2398.0    11.0     -21.0      70.0      71.0      1.0       260.g/cm2
USRYIELD   200.0     0.2       30.0       8.0       0.0      6.0          &
USRYIELD   2398.0    11.0     -21.0      97.0      98.0      1.0       940.g/cm2
...
USRYIELD   200.0     0.2       30.0       8.0       0.0      6.0          &
USRYIELD   2398.0    11.0     -21.0      98.0      99.0      1.0       971.g/cm2
USRYIELD   200.0     0.2       30.0       8.0       0.0      6.0          &
USRYIELD   2398.0    11.0     -21.0      99.0      100.0     1.0       1001g/cm2
USRYIELD   200.0     0.2       30.0       8.0       0.0      6.0          &
USRYIELD   2398.0    11.0     -21.0      100.0     101.0     1.0       1033g/cm2
USRYIELD   200.0     0.2       30.0       8.0       0.0      6.0          &
...
RANDOMIZ   1.0
START      100000.0 999999999.
STOP
```

Figure 75: Example of user data card.(cont.)

4 Data-MonteCarlo comparison

We chose to use the atmospheric muons as a benchmark of the complete simulation chain, naturally for the quality of the data available, but also for the close relation with the interesting atmospheric neutrino flux, since muons are produced in the decay of the same mesons that are the source of neutrinos. For this kind of data, precise measurements at ground level by the CAPRICE, and BESS detector are available. The two results are in agreement with each other (at the level of $\pm 5\%$). Other measurement results have been obtained at high altitude ($h \simeq 10 - 30$ km) during the ascent of stratospheric balloons by MASS, CAPRICE, HEAT and BESS detectors.

In this chapter I'll show the results of the muons simulations done using the FLUKA for Cosmic Rays package. The aim is to evaluate the different systematics of the package with the "ingredients" available at the moment.
In particular will be discussed:

- the comparison between two different atmospheric models,
- comparisons off our different primary spectra and their effects on muons at sea-level,
- muons, protons and helium simulations and comparisons at different depth in atmosphere using two different primary spectrum fits and two different interaction models (superposition model and DPMjetIII),
- muons simulations and comparisons at sea-level for energy up to 3 TeV (L3+Cosmic experiment).

4.1 Atmosphere

As told in Section 3.3.3 two different atmospheric models was taken into account: U.S. Standard Atmosphere 1976, NRLMSISE-00 Model 2001.

The data-MonteCarlo comparison have been done on different data sets, covering different experimental location with very different cut-off rigidity (11.4 and 0.4 GV respectively). The first comparison has been made on the BESS experiment data, taken at Tsukuba (Japan) during the year 1995, with a vertical cut-off rigidity of 11.4 GV (Fig.76-81). The geometrical acceptance was about 0.03 m^2sr ($\cos\theta \geq 0.98$ where θ is the zenith angle). The simulation related to NRLMSISE-00 Model 2001 (Figs.76,79) was performed with the Fluka 2005.6 version and the PrimaryCR fit 2005 as primary spectrum. The simulation related to U.S. Standard Atmosphere 1976 (Figs.77,80) was performed with the Fluka 2003 version and the AMS-BESS fit 2001 as primary spectrum. As shown in Appendix A, there is about 5% of excess of production in Fluka 2005.6 version with respect to Fluka 2003 version. Moreover, as we'll see in Section 4.2, there is about 5-10% of lack of production with the PrimaryCR fit 2005 with respect to the AMS-BESS fit 2001. Thus we expect to have no more than 5% of excess from these two ingredients. As shown in Figs.78,81, the comparison between the two simulations gives no more than 5% of excess for the first, as expected. This difference gives the maximum order of magnitude of the effect of the two different atmospheric models.

The second data-MonteCarlo comparison shown in Figs.82-85 is based on the BESS data taken at Lynn Lake in the years 1997, 1998, 1999, with a vertical cut-off rigidity of 0.4 GV. The geometrical acceptance was 0.09 m^2sr ($\cos\theta \geq 0.90$ where θ is the zenith angle). The simulations were accomplished for both the atmospheric models with the same Fluka version (Fluka 2003) and AMS-BESS fit 2001 primary spectrum. The difference between the two models is within 5%, as in the previous comparison.

As previously stated, the physical assumptions underlying the two different atmospheric models are similar. This explains the substantial agreement (within 5%) of the results of the two simulated atmospheres. Beyond this accuracy, NRLMSISE-00 Model 2001 seems to ensure better description of local and seasonal variation.

Tsukuba 1995 negative muons

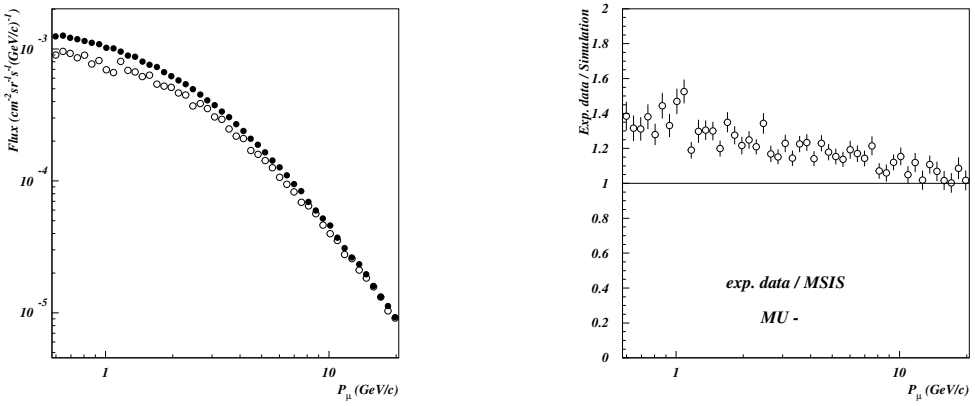

Figure 76: NRLMSISE-00 Model 2001. Flux and data/simulation ratio for negative muons in Tsukuba (Japan) 1995. Fluka 2005.6. PrimaryCR fit 2005. Black points are data and open symbols are simulation.

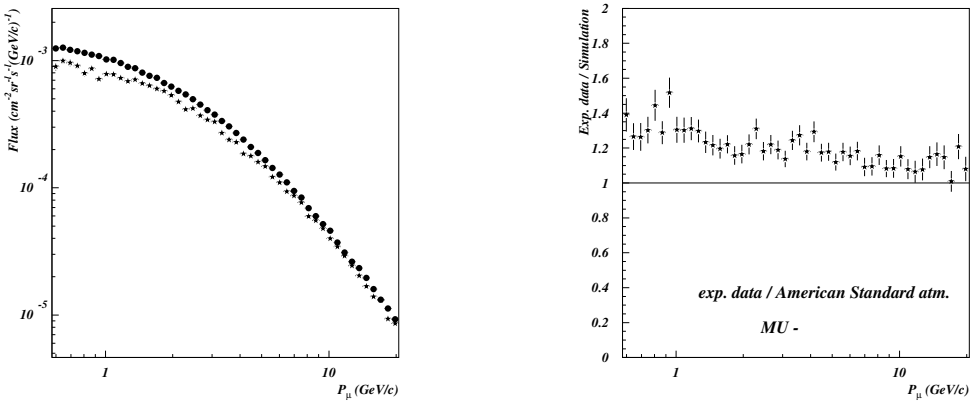

Figure 77: U.S. Standard Atmosphere 1976. Flux and data/simulation ratio for negative muons in Tsukuba (Japan) 1995. Fluka 2003. AMS-BESS fit 2001. Black points are data and stars are simulation.

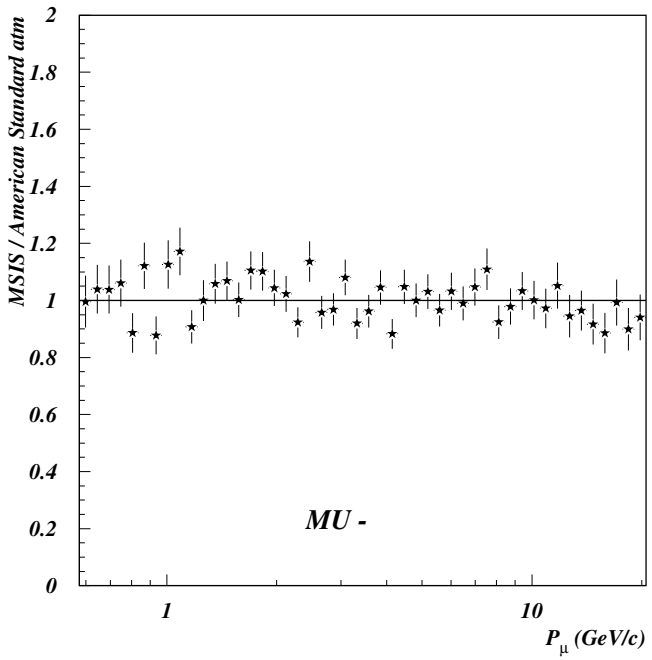

Figure 78: Comparison between NRLMSISE-00 Model 2001 and U.S. Standard Atmosphere 1976 simulations(Figs 76,77) for negative muons in Tsukuba (Japan) 1995.

Tsukuba 1995 positive muons

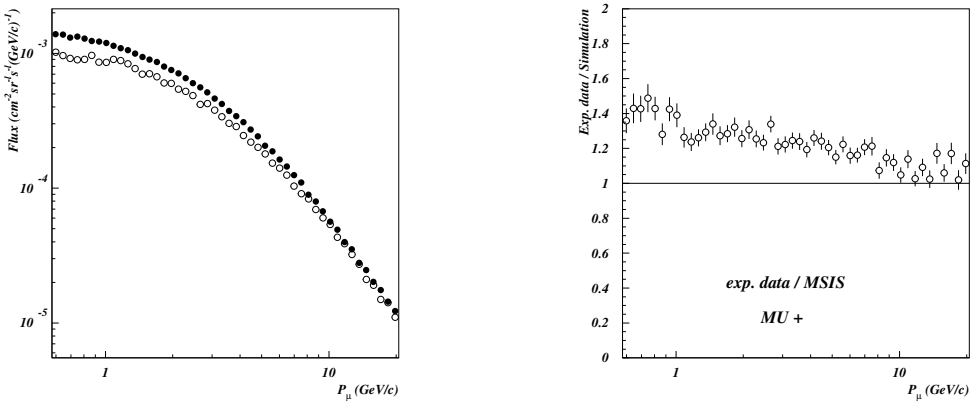

Figure 79: NRLMSISE-00 Model 2001. Flux and data/simulation ratio for positive muons in Tsukuba (Japan) 1995. Fluka 2005.6. PrimaryCR fit 2005. Black points are data and open symbols are simulation.

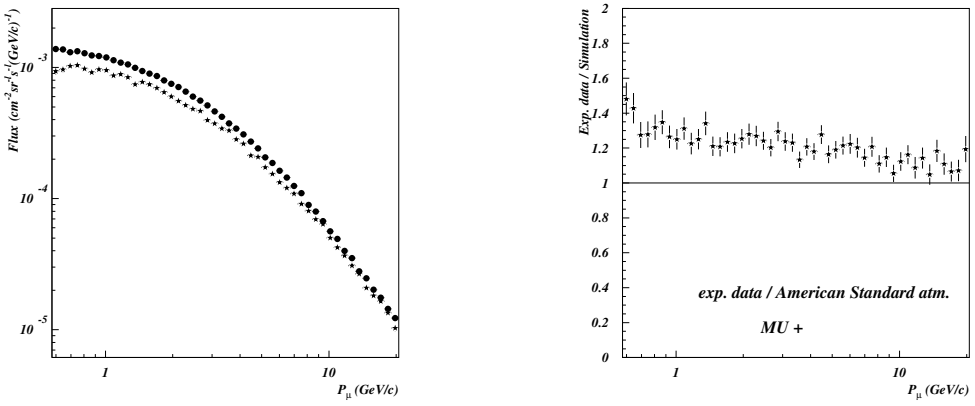

Figure 80: U.S. Standard Atmosphere 1976. Flux and data/simulation ratio for positive muons in Tsukuba (Japan) 1995. Fluka 2003. AMS-BESS fit 2001. Black points are data and stars are simulation.

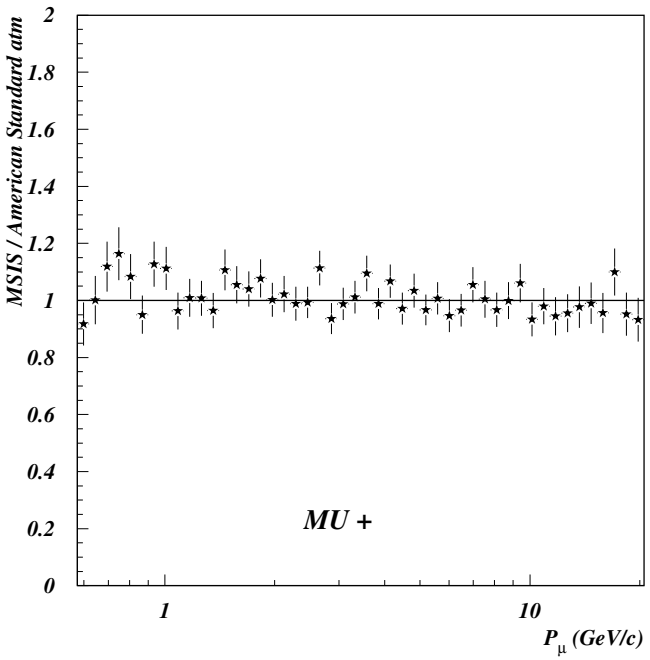

Figure 81: Comparison between NRLMSISE-00 Model 2001 and U.S. Standard Atmosphere 1976 simulations(Figs 79,80) for positive muons in Tsukuba (Japan) 1995.

Lynn Lake '97-'98-'99 negative muons

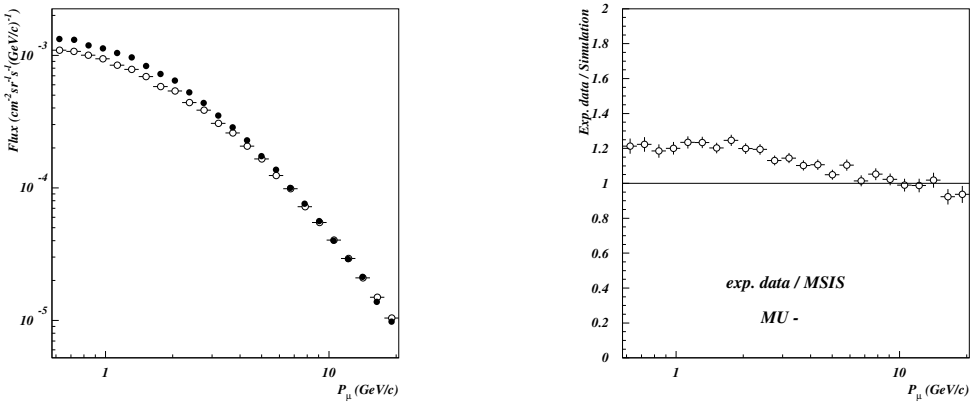

Figure 82: NRLMSISE-00 Model 2001. Flux and data/simulation ratio for negative muons in Lynn Lake (Canada) '97-'98-'99. Fluka 2003. AMS-BESS fit 2001. Black points are data and open symbols are simulation.

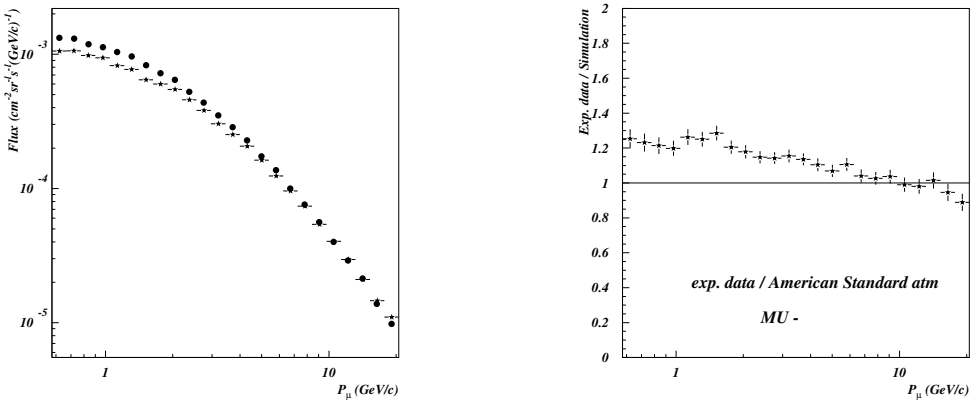

Figure 83: U.S. Standard Atmosphere 1976. Flux and data/simulation ratio for negative muons in Lynn Lake (Canada) '97-'98-'99. Fluka 2003. AMS-BESS fit 2001. Black points are data and stars are simulation.

Lynn Lake '97-'98-'99 positive muons

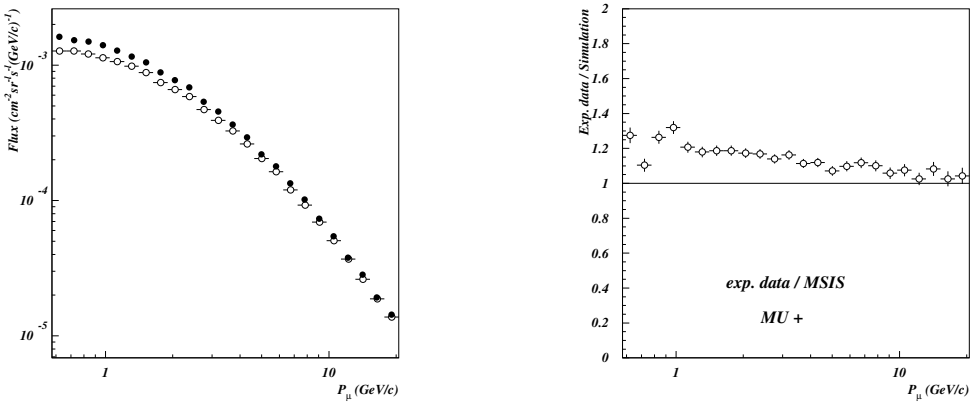

Figure 84: NRLMSISE-00 Model 2001. Flux and data/simulation ratio for positive muons in Lynn Lake (Canada) '97-'98-'99. Fluka 2003. AMS-BESS fit 2001. Black points are data and open symbols are simulation.

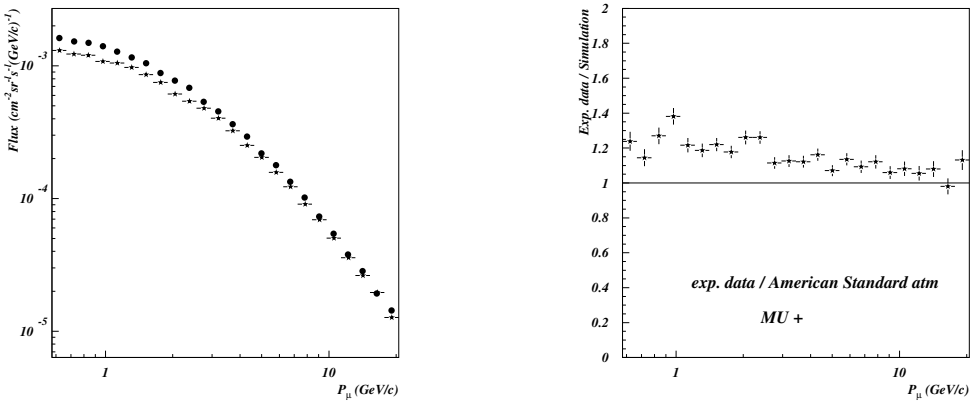

Figure 85: U.S. Standard Atmosphere 1976. Flux and data/simulation ratio for positive muons in Lynn Lake (Canada) '97-'98-'99. Fluka 2003. AMS-BESS fit 2001. Black points are data and stars are simulation.

4.2 Effect of Primary Spectra

We test the effect of the primary composition on the package performance using the muon data of BESS experiments described in Section 2.1.3. The observations was performed at sea level (30 m above sea level) in Tsukuba, Japan, and at 360 m above sea level in Lynn Lake, Canada. The vertical cutoff rigidities in Tsukuba (36.2° N, 140.1° E) and in Lynn Lake (56.5° N, 101.0° W) are 11.4 and 0.4 GV, respectively. The geometrical acceptance in Tsukuba was about 0.03 m^2sr ($\cos\theta \geq 0.98$ where θ is the zenith angle) and in Lynn Lake 0.09 m^2sr ($\cos\theta \geq 0.90$).
Simulations are done using the three different primary spectrum options described in Section 3.3.1. In Figs. 86,87 is shown the proton component of the primary spectrum for the NASA Spectrum and for the AMS-BESS fit 2001 in the day (and year) of the BESS Tsukuba experiment (1995). Figs. 88-91 show the μ^- and μ^+ fluxes simulated using the NASA Spectrum and the AMS-BESS fit 2001 and compared with experimental data. There is a lack of production of 15% up to 25% on the whole range of energy in the case of the AMS-BESS fit 2001. The NASA Spectrum simulation looks better both for lower and higher energies.
The same comparison is done for the Lynn Lake data set of '97-'98-'99 (Figs. 92-97). In this case the NASA spectrum looks too high. There is an excess of production up to 25% both for μ^- and μ^+. On the other hand there is a lack of production up to 20% for the AMS-BESS fit 2001 spectrum, mostly at lower energies.
Figs. 98-103 show a comparison between the AMS-BESS fit 2001 simulation and PrimaryCR fit 2005 simulation. Simulations are related to Lynn Lake data set and use NRLMSISE-00 Model 2001 for the atmosphere. The AMS-BESS fit 2001 simulation is some percent higher then the PrimaryCR fit 2005 one and closer to experimental data.

Primary spectrum: NASA Spectrum and AMS-BESS fit 2001 for the BESS Tsukuba experiment (1995)

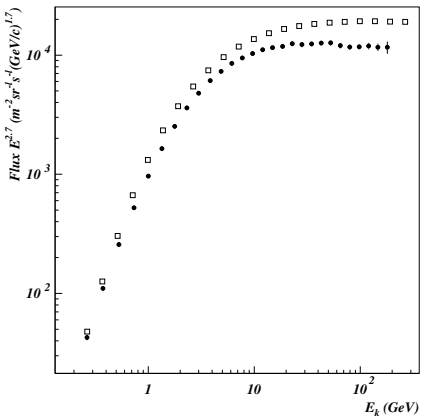

Figure 86: The proton component of the primary spectrum for the **NASA Spectrum** in the day (and year) of the BESS Tsukuba experiment (1995). Black points are AMS data.

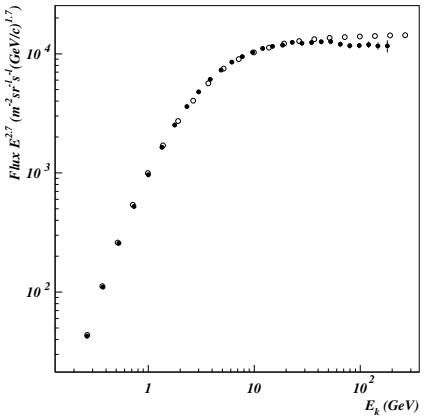

Figure 87: The proton component of the primary spectrum AMS-BESS fit 2001 in the day (and year) of the BESS Tsukuba experiment (1995). Black points are AMS data.

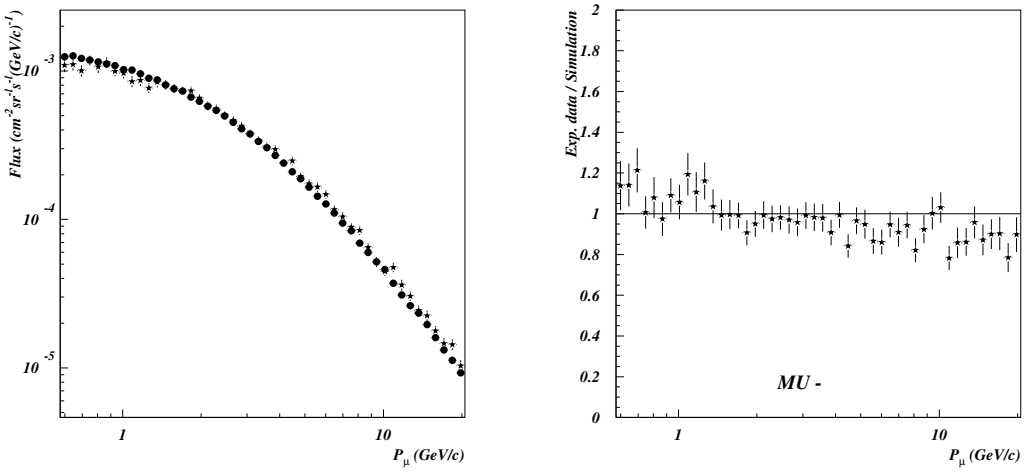

Figure 88: The μ^- flux simulated (stars) using the NASA Spectrum and compared with experimental data (black points). Data/simulation ratio on the right. U.S. Standard Atmosphere 1976. Fluka 2003. BESS Tsukuba experiment (1995).

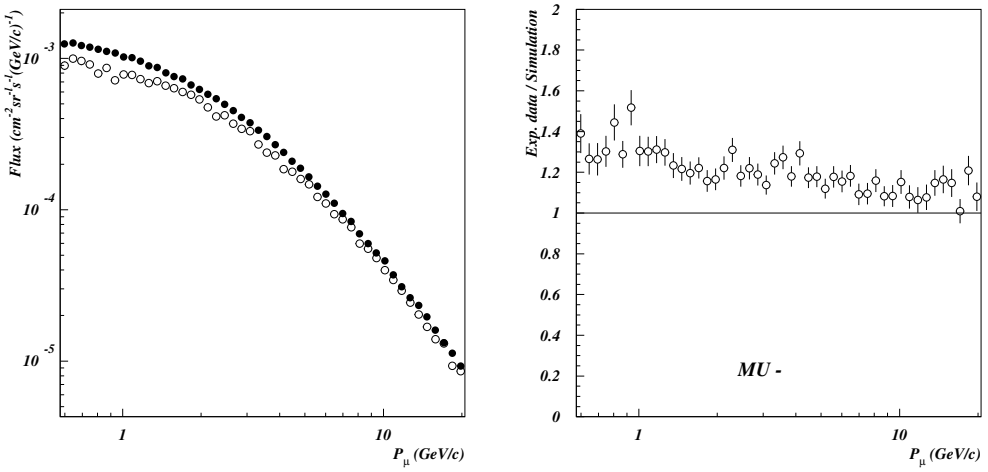

Figure 89: The μ^- flux simulated (open symbols) using the primary spectrum AMS-BESS fit 2001 and compared with experimental data (black points). Data/simulation ratio on the right. U.S. Standard Atmosphere 1976. Fluka 2003. BESS Tsukuba experiment (1995).

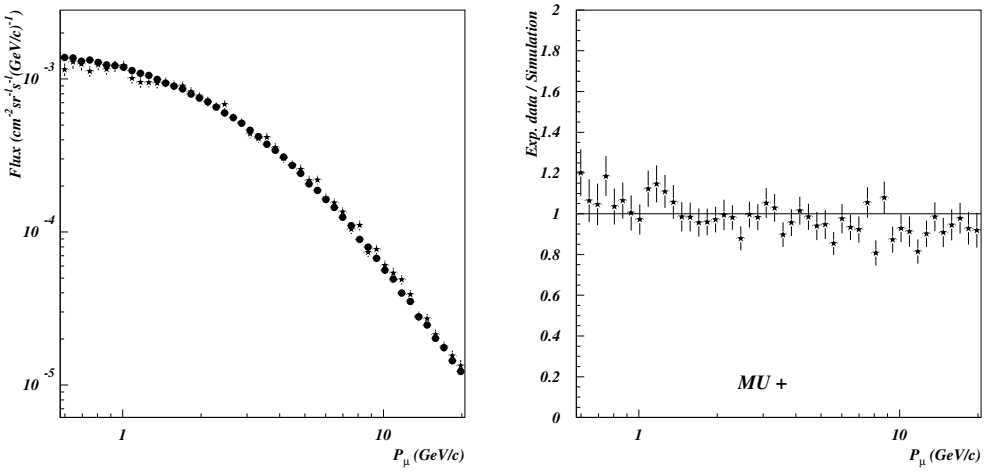

Figure 90: The μ^+ flux simulated (stars) using the NASA Spectrum and compared with experimental data (black points). Data/simulation ratio on the right. U.S. Standard Atmosphere 1976. Fluka 2003. BESS Tsukuba experiment (1995).

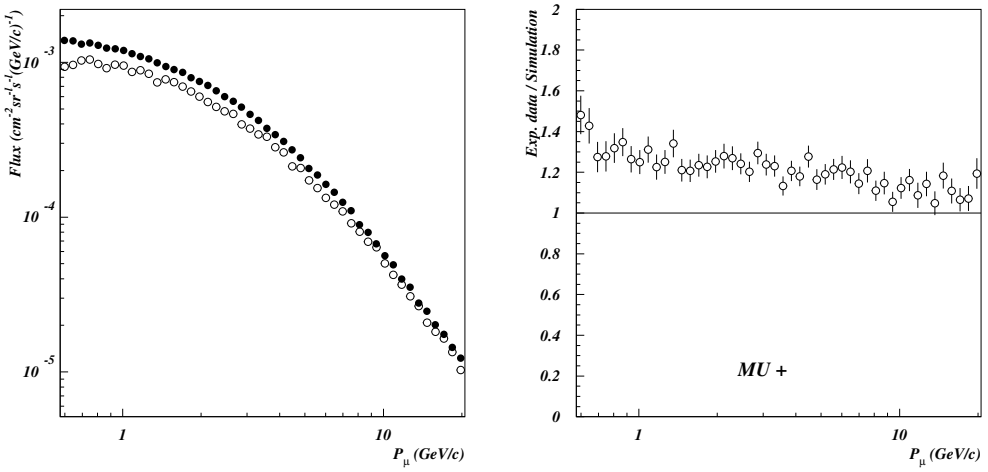

Figure 91: The μ^+ flux simulated (open symbols) using the AMS-BESS fit 2001 primary spectrum and compared with experimental data (black points). Data/simulation ratio on the right. U.S. Standard Atmosphere 1976. Fluka 2003. BESS Tsukuba experiment (1995).

Primary spectrum: NASA Spectrum and AMS-BESS fit 2001 for the BESS Lynn Lake experiment ('97-'98-'99)

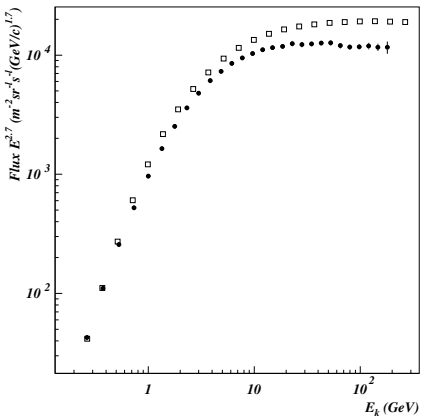

Figure 92: The proton component of the primary spectrum NASA Spectrum in the day (and year) of the BESS Lynn Lake experiment ('97-'98-'99). Black points are AMS data.

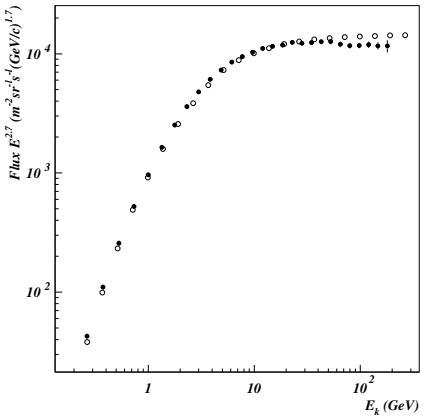

Figure 93: The proton component of the primary spectrum AMS-BESS fit 2001 in the day (and year) of the BESS Lynn Lake experiment ('97-'98-'99). Black points are AMS data.

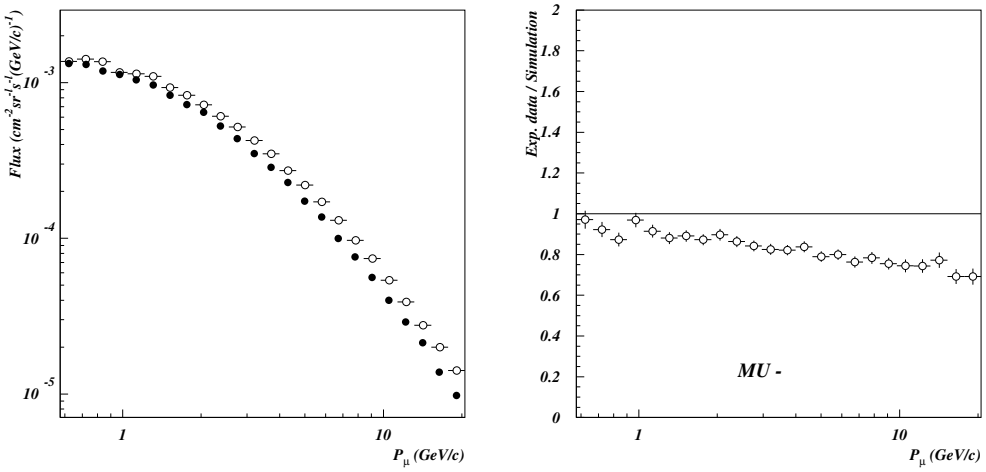

Figure 94: The μ^- flux simulated (open symbols) using the primary spectrum NASA Spectrum and compared with experimental data (black points). Data/simulation ratio on the right. U.S. Standard Atmosphere 1976. Fluka 2003. BESS Lynn Lake experiment ('97-'98-'99).

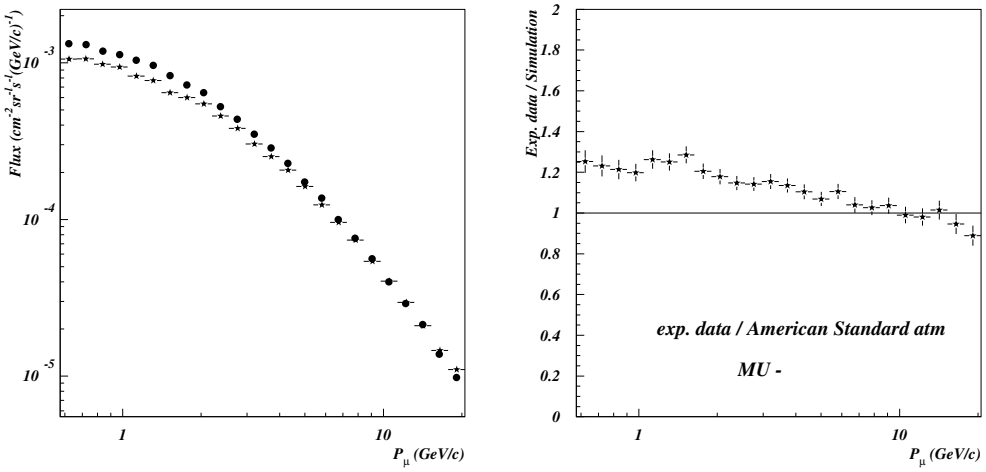

Figure 95: The μ^- flux simulated (stars) using the primary spectrum AMS-BESS fit 2001 and compared with experimental data (black points). Data/simulation ratio on the right. U.S. Standard Atmosphere 1976. Fluka 2003. BESS Lynn Lake experiment ('97-'98-'99).

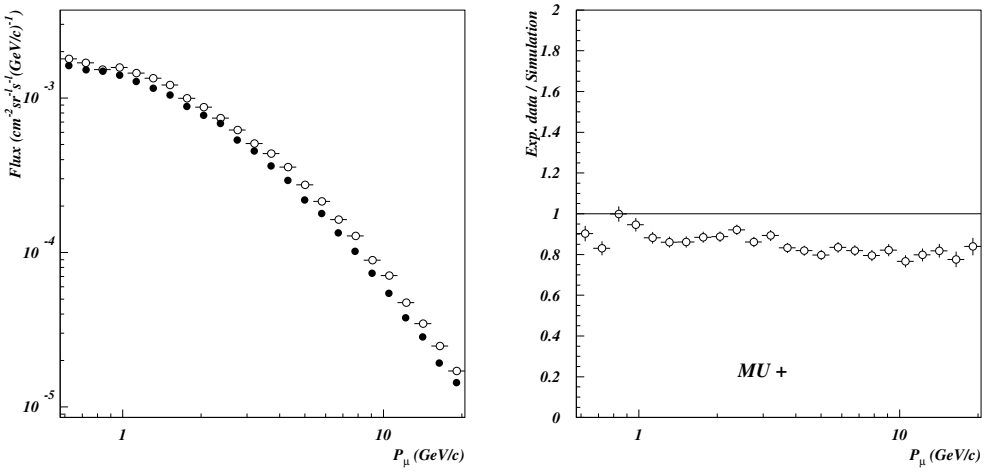

Figure 96: The μ^+ flux simulated (open symbols) using the primary spectrum NASA Spectrum and compared with experimental data (black points). Data/simulation ratio on the right. U.S. Standard Atmosphere 1976. Fluka 2003. BESS Lynn Lake experiment ('97-'98-'99).

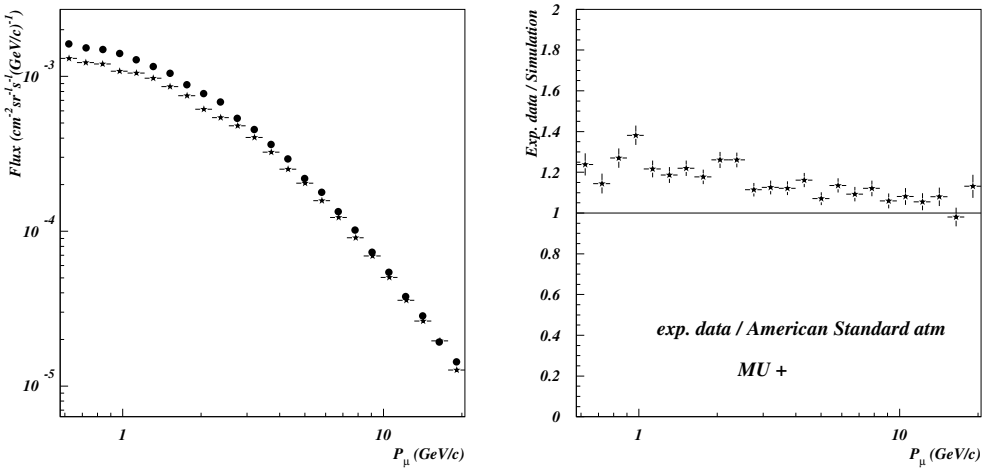

Figure 97: The μ^+ flux simulated (stars) using the primary spectrum AMS-BESS fit 2001 and compared with experimental data (black points). Data/simulation ratio on the right. U.S. Standard Atmosphere 1976. Fluka 2003. BESS Lynn Lake experiment ('97-'98-'99).

Primary spectrum: AMS-BESS fit 2001 and PrimaryCR fit 2005 for the BESS Lynn Lake experiment ('97-'98-'99)

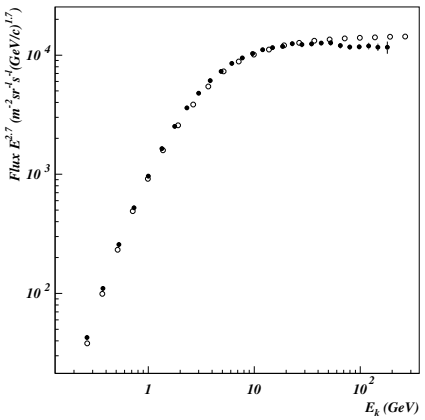

Figure 98: The proton component of the primary spectrum AMS-BESS fit 2001 in the day (and year) of the BESS Lynn Lake experiment ('97-'98-'99). Black points are AMS data.

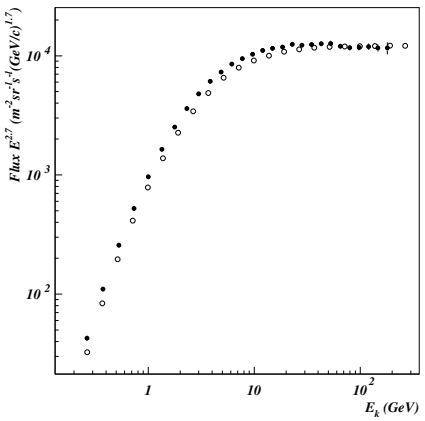

Figure 99: 98 hiz3 The proton component of the primary spectrum PrimaryCR fit 2005 in the day (and year) of the BESS Lynn Lake experiment ('97-'98-'99). Black points are AMS data.

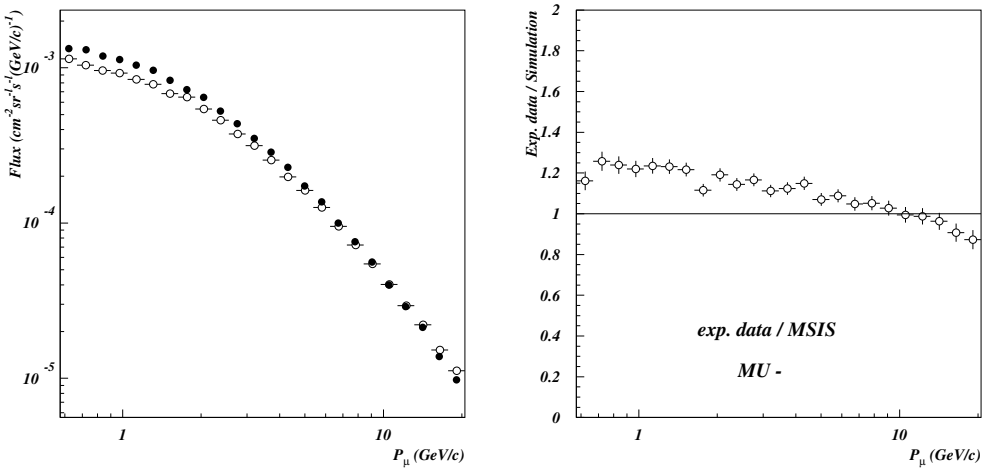

Figure 100: The μ^- flux simulated (open symbols) using the primary spectrum AMS-BESS fit 2001 and compared with experimental data (black points). Data/simulation ratio on the right. NRLMSISE-00 Model 2001 for the atmosphere. Fluka 2005.6. BESS Lynn Lake experiment ('97-'98-'99).

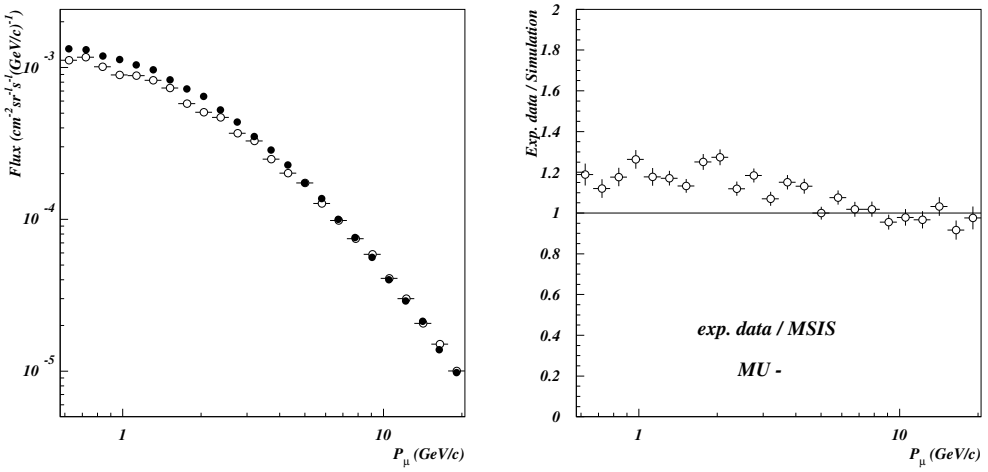

Figure 101: The μ^- flux simulated (open symbols) using the primary spectrum PrimaryCR fit 2005 and compared with experimental data (black points). Data/simulation ratio on the right. NRLMSISE-00 Model 2001 for the atmosphere. Fluka 2005.6. BESS Lynn Lake experiment ('97-'98-'99).

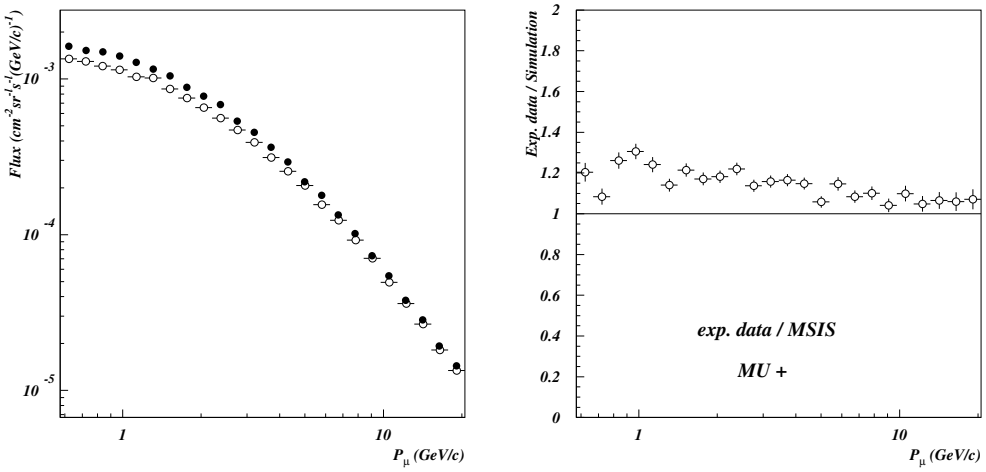

Figure 102: The μ^+ flux simulated (open symbols) using the primary spectrum AMS-BESS fit 2001 and compared with experimental data (black points). Data/simulation ratio on the right. NRLMSISE-00 Model 2001 for the atmosphere. Fluka 2005.6. BESS Lynn Lake experiment ('97-'98-'99).

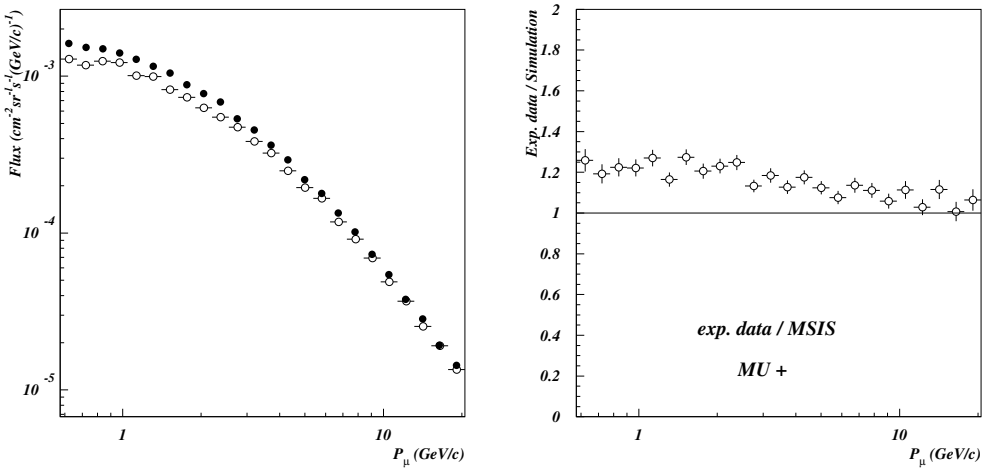

Figure 103: The μ^+ flux simulated (open symbols) using the primary spectrum PrimaryCR fit 2005 and compared with experimental data (black points). Data/simulation ratio on the right. NRLMSISE-00 Model 2001 for the atmosphere. Fluka 2005.6. BESS Lynn Lake experiment ('97-'98-'99).

Primary spectrum: High Energy All-nucleon Spectrum for the BESS Lynn Lake experiment ('97-'98-'99)

Geomagnetic cut-off and solar modulation activity characteristics of **High Energy All-nucleon Spectrum** primary spectrum are similar to BESS Lynn Lake experiment ('97-'98-'99) (low geomagnetic cut-off = 0.4 GV and Solar Minimum activity).
Experimental data and simulation (Figs. 104-105) are in good agreement but there is a global excess of production for μ^+.

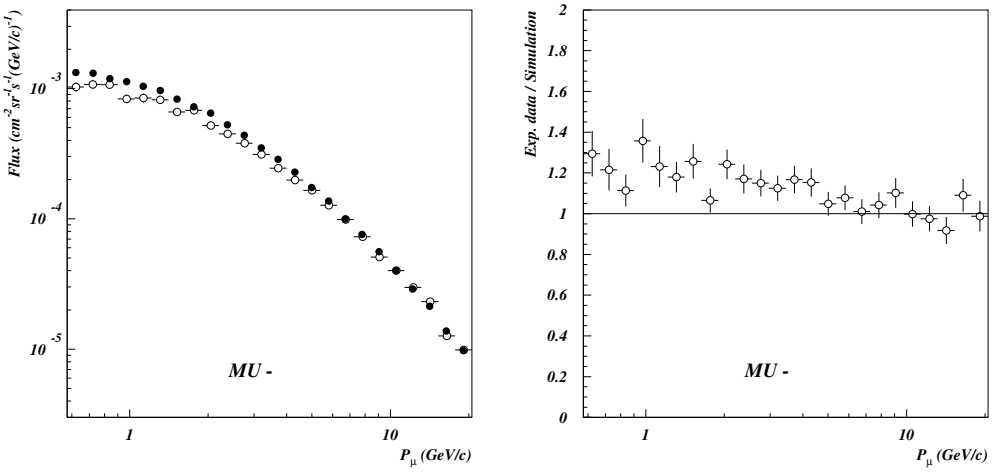

Figure 104: The μ^- flux simulated (open symbols) using the **High Energy All-nucleon Spectrum** primary spectrum and compared with experimental data (black points). Data/simulation ratio on the right. NRLMSISE-00 Model 2001 for the atmosphere. Fluka 2005.6. BESS Lynn Lake experiment ('97-'98-'99).

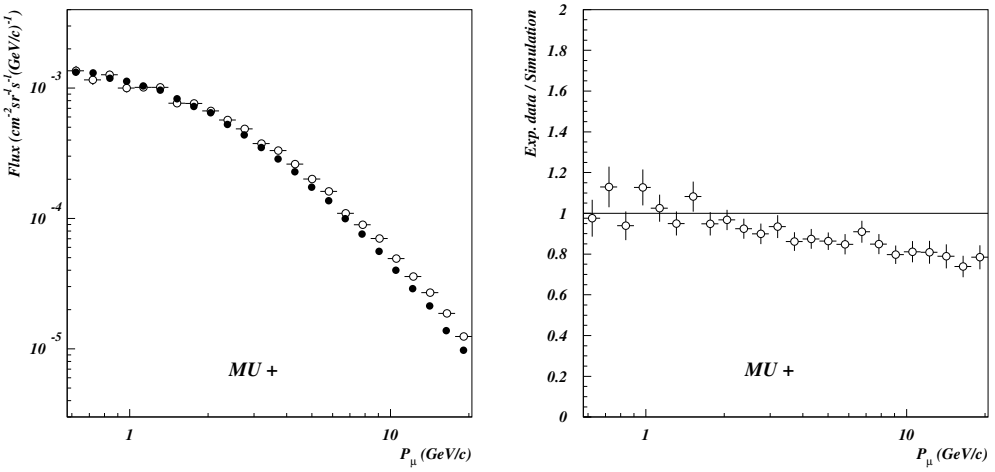

Figure 105: The μ^+ flux simulated (open symbols) using the **High Energy All-nucleon Spectrum** primary spectrum and compared with experimental data (black points). Data/simulation ratio on the right. NRLMSISE-00 Model 2001 for the atmosphere. Fluka 2005.6. BESS Lynn Lake experiment ('97-'98-'99).

Simulation vs Data comparison for different atmospheric models and primary spectra options

A measure of the reliability of the complete package is the behavior of the DATA/MC ratio of the reported fluxes of atmospheric muons over the entire energy range of production of the secondary particles.

A feature of this quantity, that is common to the results obtained for every simulation, independently of the atmospheric model, interaction model and also primary spectrum used, is an energy dependence with respect to the secondary momentum. This effect is always present, even with the different average values and corresponding different fluctuations of the ratio obtained for the different simulation setups and data taking. A consequence of this behavior is clearly seen on the RMS of the ratios values obtained. This quantity can be assumed as in indicator of a possible systematic of the package (neglecting the contribution to RMS to the statistic of data and simulation), and is greatly enhanced by this energy dependence.

A partial hint of the source of this effect can be derived fitting the ratios with respect the particle momentum. As a matter of fact the best fitting function is a power law function:

$$f(p_\mu) = P1 * p_\mu^{P2} \tag{55}$$

where p_μ is the muon momentum and $P1$ and $P2$ are the two parameters of the fit. As examples we report in Figs. 106-109 the power law fit to the ratios shown in Figs. 76, 89, 91 and 100. With the fits, are also shown the original scatter of the ratios and the scatter of the same ratios with respect to the fitted values. Both the goodness of the fit and the very Gaussian behavior of the scatter with respect to the fit indicates that this systematic could be induced by an ingredient of the simulation chain that has a similar power low scaling over the entire range of particle production, namely the primary spectrum adopted for the simulation.

This preliminary conclusion must be confirmed by using different primary spectrum.

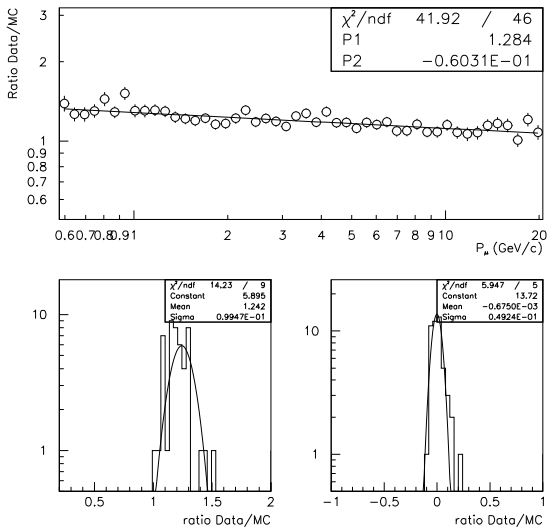

Figure 106: Power law fit of the ratio of Fig. 77 (U.S. Standard Atmosphere 1976. Negative muons in Tsukuba (Japan) 1995. Fluka 2003. AMS-BESS fit 2001). Below at right the ratio original scatter and the scatter with respect to the power law fit.

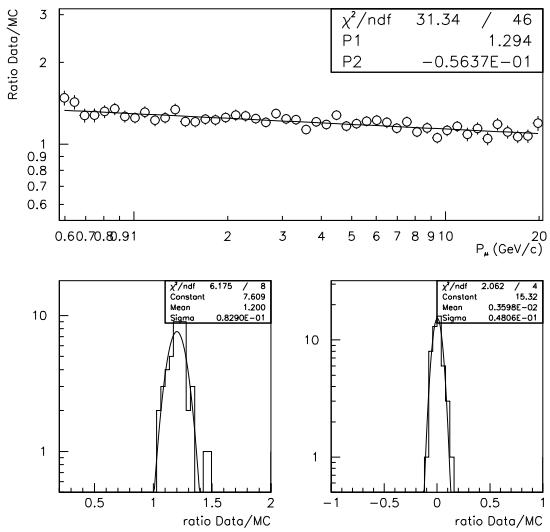

Figure 107: Power law fit of the ratio of Fig.91 (U.S. Standard Atmosphere 1976. Positive muons in Tsukuba (Japan) 1995. Fluka 2003. AMS-BESS fit 2001). Below at right the ratio original scatter and the scatter with respect to the power law fit.

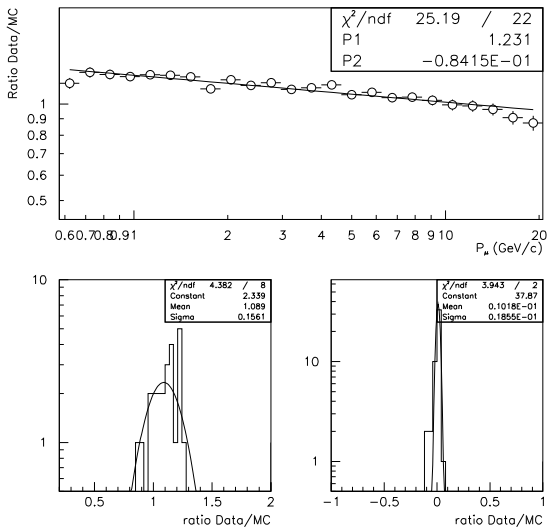

Figure 108: Power law fit of the ratio of Fig.100 (NRLMSISE-00 Model 2001 for the atmosphere. Negative muons in Lynn Lake (Canada) '97-'98-'99. Fluka 2005.6. AMS-BESS fit 2001). Below at right the ratio original scatter and the scatter with respect to the power law fit.

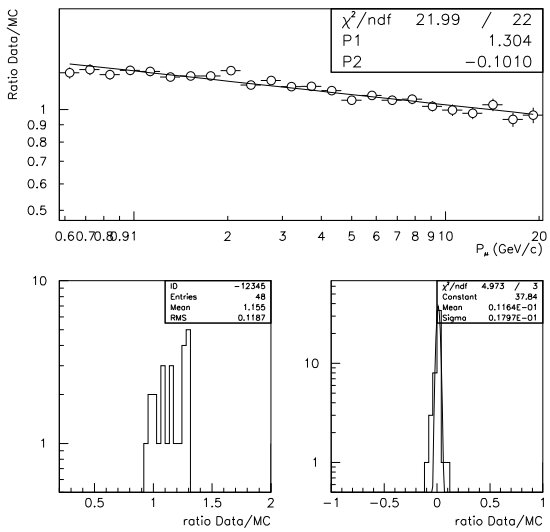

Figure 109: Power law fit of the ratio of Fig.82 (NRLMSISE-00 Model 2001 for the atmosphere. Negative muons in Lynn Lake (Canada) '97-'98-'99. Fluka 2003. AMS-BESS fit 2001). Below at right the ratio original scatter and the scatter with respect to the power law fit.

4.3 High altitude measurements

4.3.1 Atmospheric muons at mountain altitude

In order to understand better the propagation process of cosmic rays particles through the atmosphere, we compared FLUKA simulations with the experimental data of atmospheric muons taken at the top of Mt. Norikura, Japan with the BESS detector.
We decide to use FLUKA in "superposition model" as hadronic interaction model, and the NRLMSISE-00 Model 2001 for the atmospheric model. In this condition we reproduced the experimental data using the two new fit options as primary spectrum.
In this experiment the energy range for muons extends up to 100 GeV.
The Norikura Observatory is located at $36°06'N$, $137°33'E$, which is about 40 km southeast of Kamioka. The altitude is 2 770 m above sea level. The vertical geomagnetic cutoff rigidity is 11.2 GV. The geometrical acceptance was 0.0214 m^2sr ($cos\theta \geq 0.98$ where θ is the zenith angle). The experiment was performed during two periods of 17th-19th and 21st-23th of September 1999.
Figs. 110, 111 show the μ^- and μ^+ fluxes simulated using the primary spectrum PrimaryCR fit 2005 and Figs. 112, 113 show the μ^- and μ^+ fluxes simulated using the primary spectrum AMS-BESS fit 2001. Simulations are compared with experimental data.
Both simulations show a good agreement with data at higher energies and a lack of production at lower energies (up to 20 %). The AMS-BESS fit 2001 simulation looks few percent higher than the PrimaryCR fit 2005 one on the whole range of energy, resulting closer to experimental data.

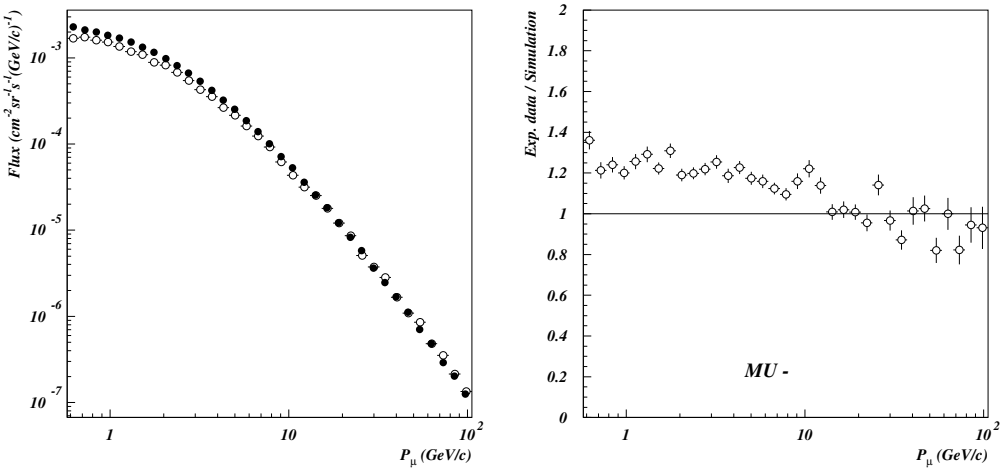

Figure 110: The μ^- flux (open symbols) simulated using the primary spectrum PrimaryCR fit 2005 and compared with experimental data (black points). Experimental data/simulation ratio on the right. NRLMSISE-00 Model 2001 for the atmosphere. FLUKA 2005.6. BESS Mt. Norikura experiment (1999).

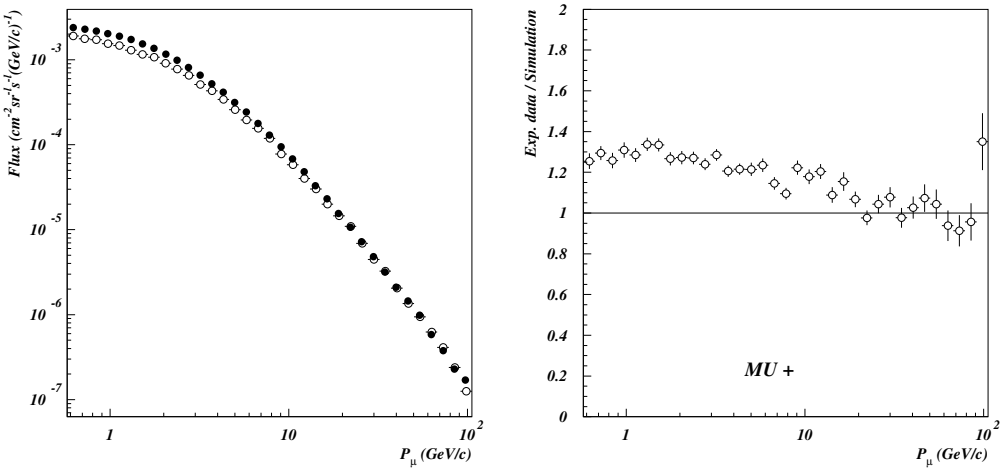

Figure 111: The μ^+ flux (open symbols) simulated using the primary spectrum PrimaryCR fit 2005 and compared with experimental data (black points). Experimental data/simulation ratio on the right. NRLMSISE-00 Model 2001 for the atmosphere. FLUKA 2005.6. BESS Mt. Norikura experiment (1999).

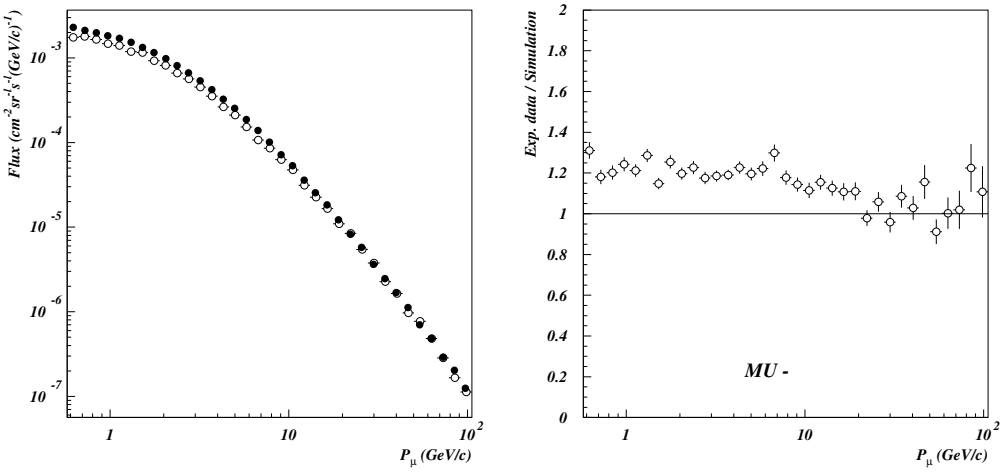

Figure 112: The μ^- flux (open symbols) simulated using the primary spectrum AMS-BESS fit 2001 and compared with experimental data (black points). Experimental data/simulation ratio on the right. NRLMSISE-00 Model 2001 for the atmosphere. FLUKA 2005.6. BESS Mt. Norikura experiment (1999).

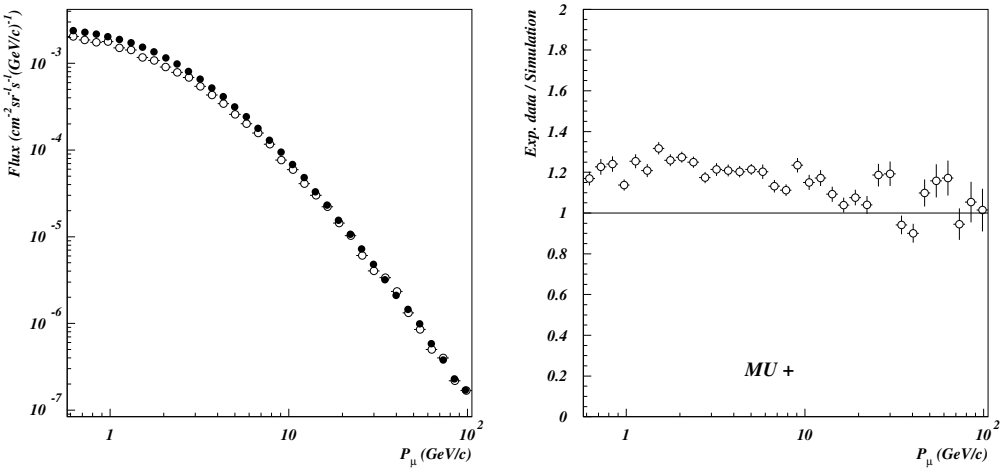

Figure 113: The μ^+ flux (open symbols) simulated using the primary spectrum AMS-BESS fit 2001 and compared with experimental data (black points). Experimental data/simulation ratio on the right. NRLMSISE-00 Model 2001 for the atmosphere. FLUKA 2005.6. BESS Mt. Norikura experiment (1999).

4.3.2 Muons, protons and helium nuclei measured during the BESS-2001 balloon flight

In this Section will be shown simulations done to reproduce the cosmic-ray proton, helium, and muon spectra at small atmospheric depths of 4.5-28 g/cm^2 measured during the slow descending period of the BESS-2001 balloon flight (see Section 2.1.5). The energy region for the proton and helium nuclei fluxes is 0.5-10 GeV/n and the momentum region for the muon fluxes is 0.5-10 GeV/c. The BESS-2001 balloon flight was carried out at Ft. Sumner, New Mexico, USA ($34°49'N, 104°22'W$) on 24th September 2001. Throughout the flight, the vertical geomagnetic cut-off rigidity was about 4.2 GV. The geometrical acceptance is 0.097 m^2sr for protons and helium nuclei, and 0.030 m^2sr for muons. The zenith angle (θ_z) was limited within $cos\theta_z \geq 0.90$ to obtain nearly vertical fluxes.

Muon spectra

At small atmospheric depths, below a few ten g/cm^2, muons come from first interaction primaries with air nuclei ($p+N \rightarrow \pi+X$). Pions produced in these interactions will decay into muons ($\pi \rightarrow \mu + \bar{\nu}_\mu$). The production process of muons is predominant over decay process. This peculiarity should allow us to observe the related hadronic interactions features and check our models.

The first simulation presented (Figs. 114-123) reproduces negative and positive muon spectra at different depth in atmosphere and their experimental data/simulation ratio. The simulation is accomplished with the AMS-BESS fit 2001 primary spectrum. The "superposition model" is used as interaction model (see Section 3.1) and the atmosphere is reproduced with NRLMSISE-00 Model 2001.
For every depth in atmosphere the simulation presents about 10% of lack of muon production.

Proton and helium spectra

We accomplished these simulations with the NRLMSISE-00 Model 2001 to reproduce the atmosphere model and with two different interactions models: "superposition model" and DPMJET III interaction model (and RQMD-2.4 interface for ion interaction from 100 MeV/n up to 5 GeV/n) (Section 3.1.2).

In the simulations shown in Figs. 124-128 (AMS-BESS fit 2001 primary spectrum) the interaction model used is the superposition model. The fluxes shown are related to protons from primary protons added to the two protons coming from primary helium nuclei, according to superposition model assumption.
Above the cut-off energy threshold for protons (3.4 GeV), there is a good reproduction (with a lack of production $< 10\%$). Below the cut-off energy threshold, the production of secondaries is more then 50% less then observed flux.

The simulations shown in Figs. 129-138 are accomplished with DPMJET III interaction model (plus RQMD-2.4 interface for ion interaction below 5 GeV/n). The primary spectrum fit used is AMS-BESS fit 2001.
Proton and helium nuclei spectra from BESS 2001 balloon flight present a geomagnetic cut-off effect at 3.4 GeV for protons and 1.4 GeV/n for helium nuclei. The above cut-off region looks well reproduced with less than 10% of lack of production for protons and about 20% for helium nuclei.
Below $\sim$2.5 GeV, proton spectra are mainly from atmospheric secondary protons. In DPMJET III model proton simulations (Figs. 129-133) this energy region present a huge lack of production: up to 60% that decrease to 20% with the increasing of the atmospheric depth.

The observed proton flux in the energy region below the geomagnetic cut-off is the result of multiple detections of the same particles. We are taking into account only a limited part of the Earth's atmosphere, the one contained into the truncated cones of our geometry (see Section 3.3.3). This prevents us from reproducing trapped particles coming from a different sector of the Earth's atmosphere. So the simulated fluxes are obtained by counting each particle crossing the detector only once, i.e. the real proton fluxes [10].

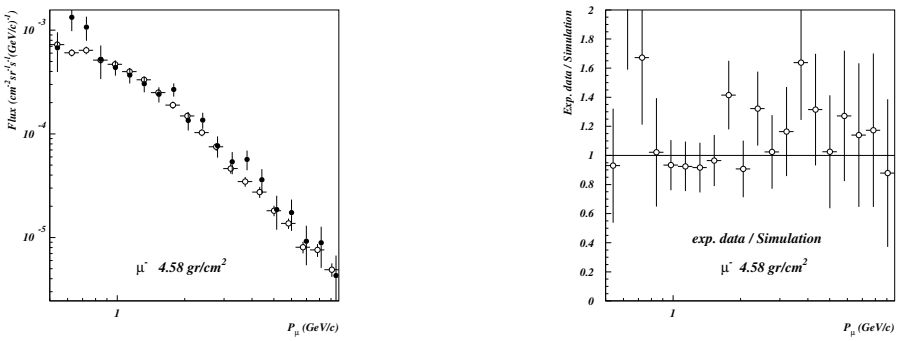

Figure 114: Atmospheric depth of 4.58 g/cm^2. The μ^- flux (open symbols) simulated using the primary spectrum **AMS-BESS fit 2001** and compared with experimental data (black points). Experimental data on simulation ratio on the right. NRLMSISE-00 Model 2001 for the atmosphere. FLUKA 2005.6 used in superposition model. BESS-2001 balloon flight.

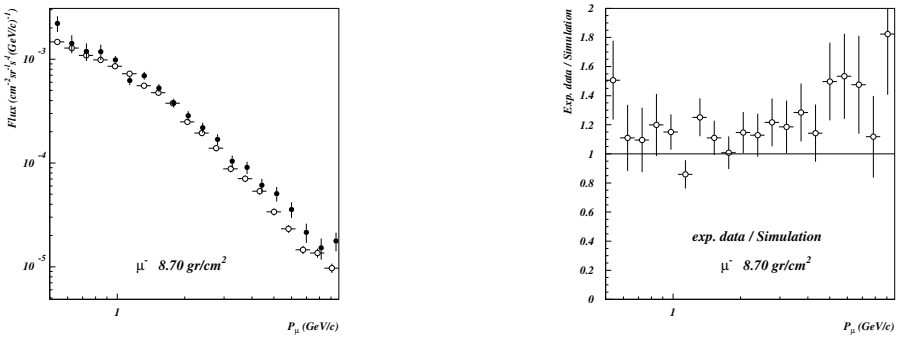

Figure 115: Atmospheric depth of 8.70 g/cm^2.

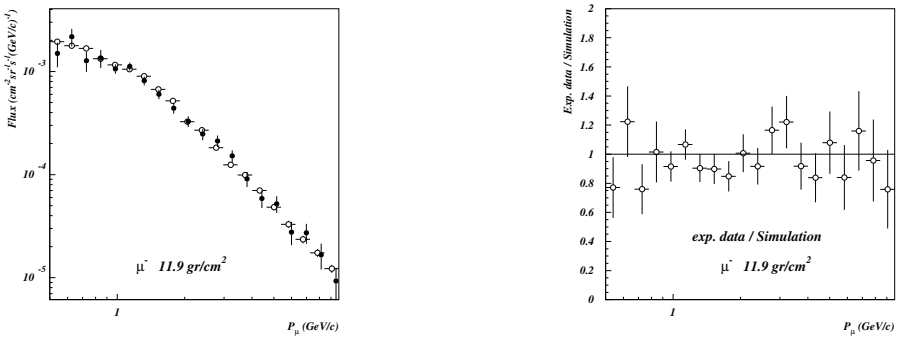

Figure 116: Atmospheric depth of 11.9 g/cm^2.

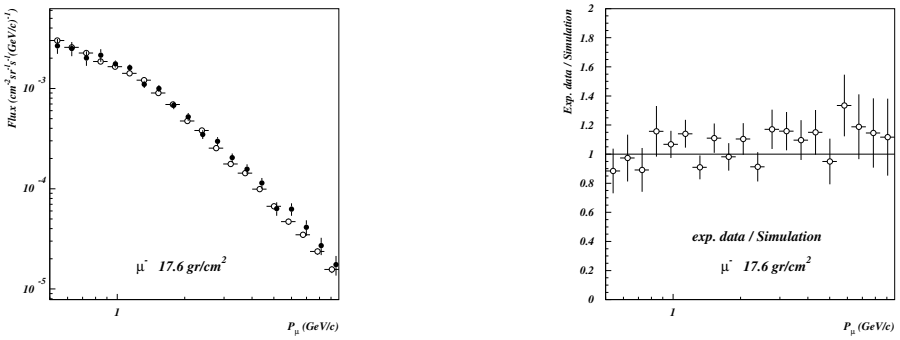

Figure 117: Atmospheric depth of 17.6 g/cm^2.

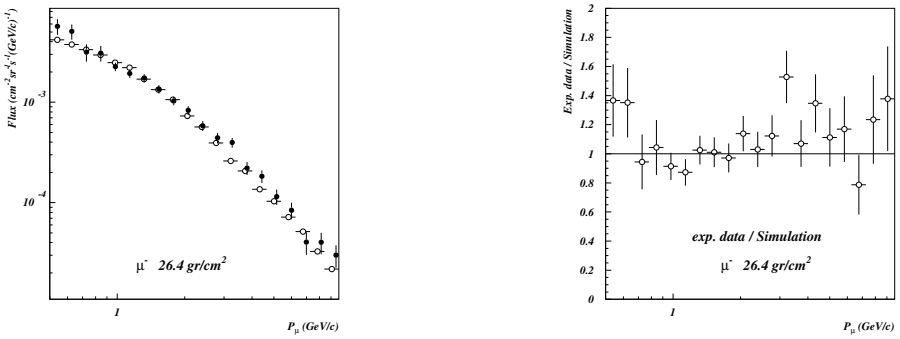

Figure 118: Atmospheric depth of 26.4 g/cm^2.

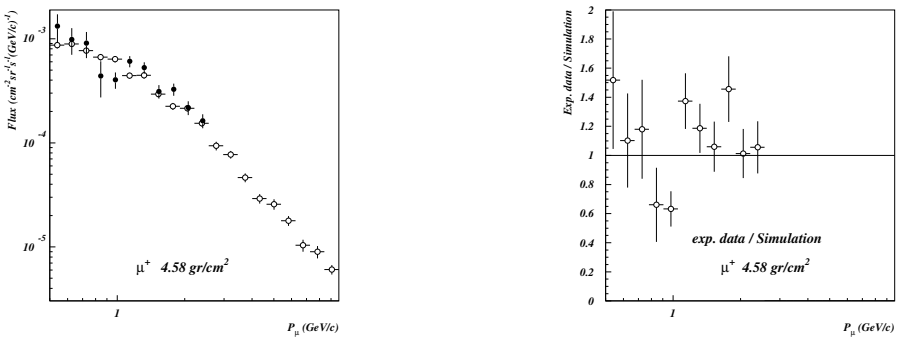

Figure 119: Atmospheric depth of 4.58 g/cm^2. The μ^+ flux (open symbols) simulated using the primary spectrum **AMS-BESS fit 2001** and compared with experimental data (black points). Experimental data on simulation ratio on the right. NRLMSISE-00 Model 2001 for the atmosphere. FLUKA 2005.6 used in superposition model. BESS-2001 balloon flight.

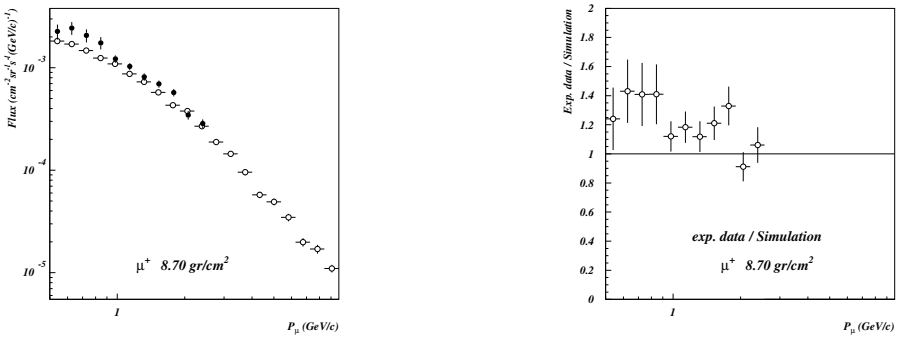

Figure 120: Atmospheric depth of 8.70 g/cm^2.

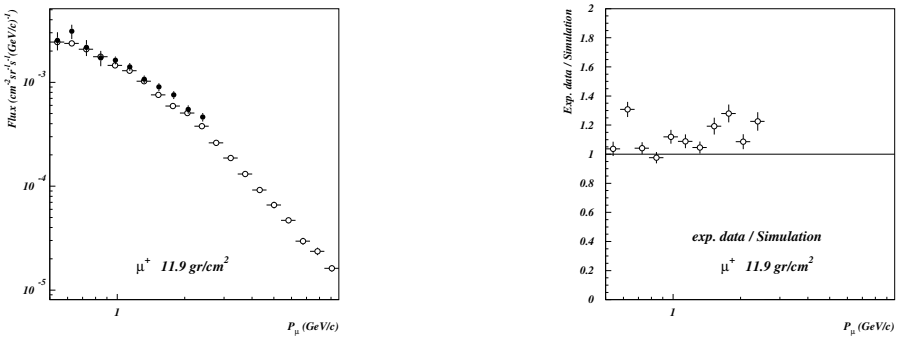

Figure 121: Atmospheric depth of 11.9 g/cm^2.

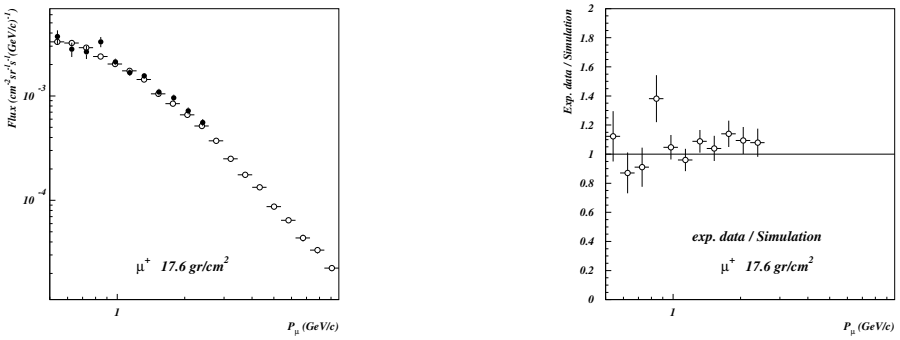

Figure 122: Atmospheric depth of 17.6 g/cm^2.

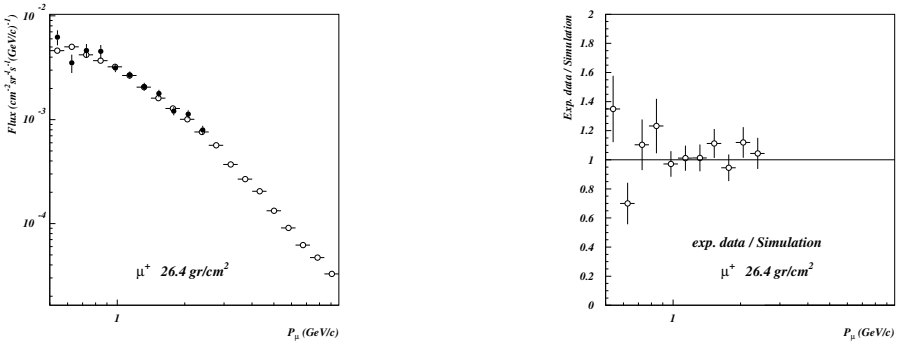

Figure 123: Atmospheric depth of 26.4 g/cm^2.

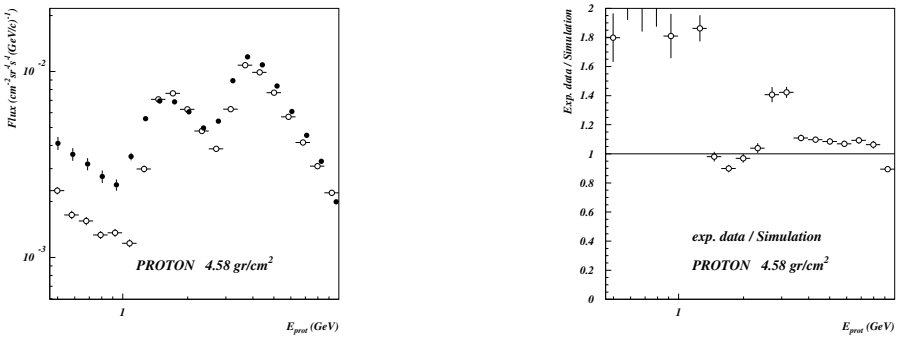

Figure 124: Atmospheric depth of 4.58 g/cm^2. Protons from primary protons added to the two protons coming from helium nuclei flux (open symbols) simulated using the primary spectrum **AMS-BESS fit 2001** and compared with experimental data (black points). Experimental data/simulation ratio on the right. NRLMSISE-00 Model 2001 for the atmosphere. FLUKA 2005.6 used in **superposition model**. BESS-2001 balloon flight.

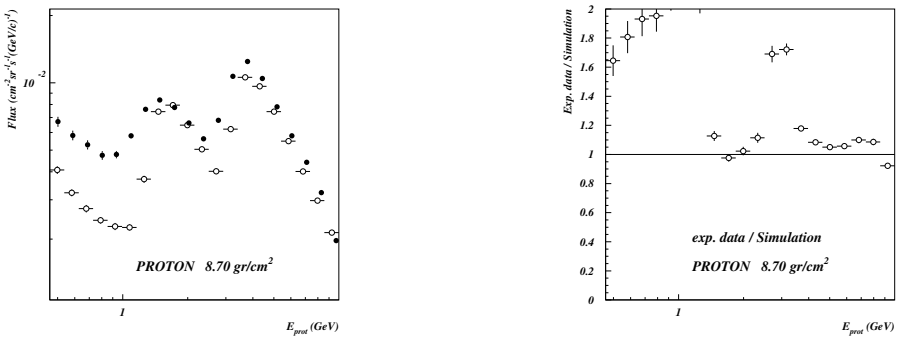

Figure 125: Atmospheric depth of 8.70 g/cm^2.

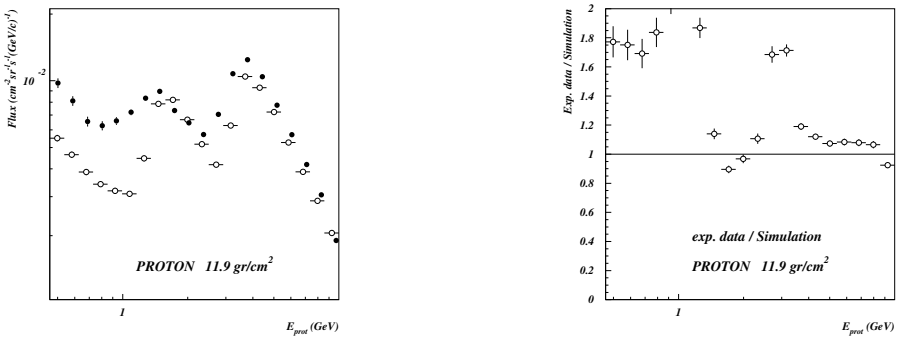

Figure 126: Atmospheric depth of 11.9 g/cm^2.

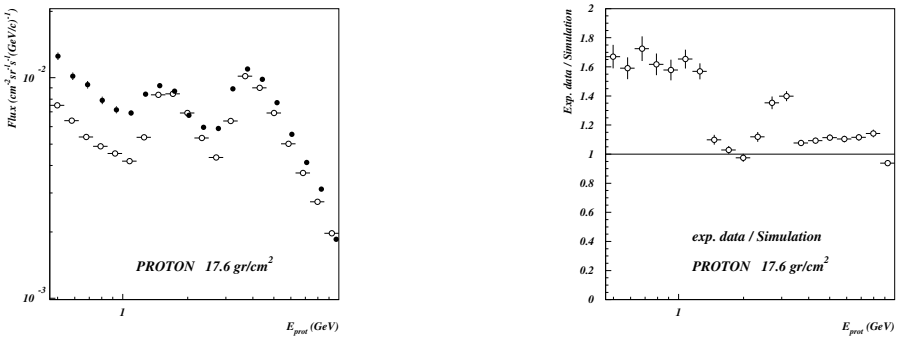

Figure 127: Atmospheric depth of 17.6 g/cm^2.

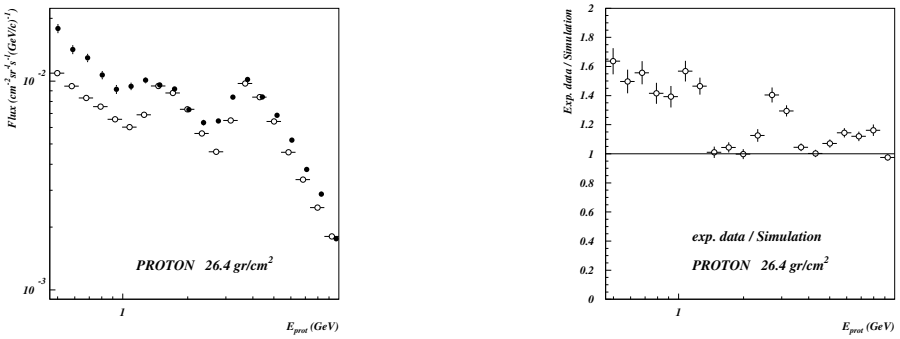

Figure 128: Atmospheric depth of 26.4 g/cm^2.

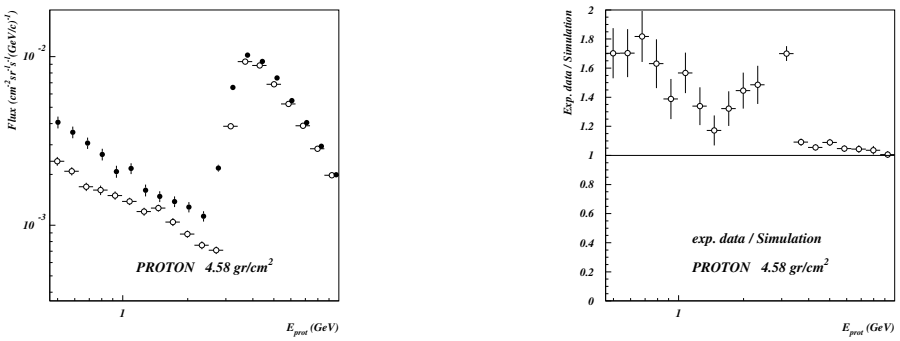

Figure 129: Atmospheric depth of 4.58 g/cm^2. Protons flux (open symbols) simulated using the primary spectrum AMS-BESS fit 2001 and compared with experimental data (black points). Experimental data/simulation ratio on the right. NRLMSISE-00 Model 2001 for the atmosphere. FLUKA 2005.6 with **DPMJET III + QMD** interaction model. BESS-2001 balloon flight.

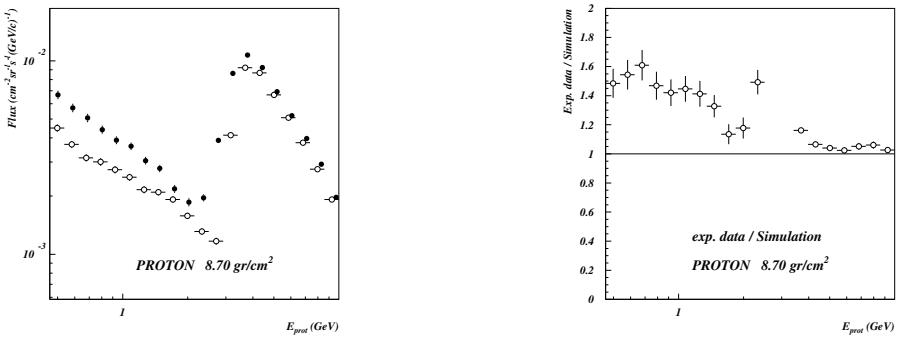

Figure 130: Atmospheric depth of 8.70 g/cm^2.

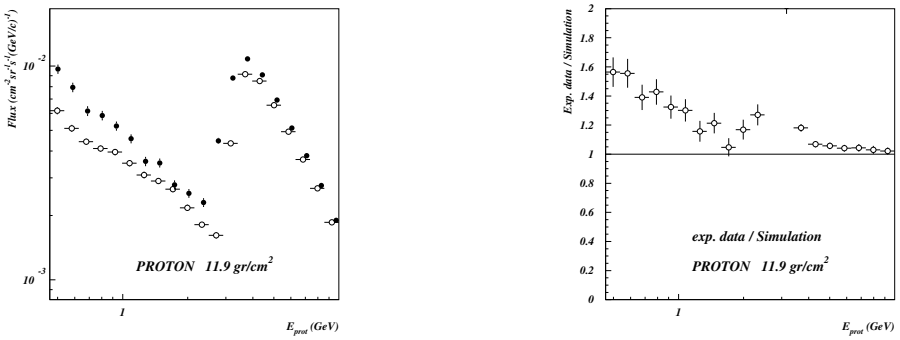

Figure 131: Atmospheric depth of 11.9 g/cm^2.

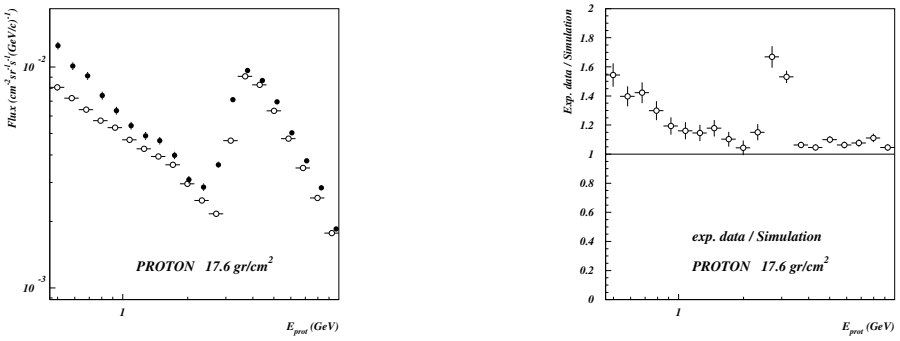

Figure 132: Atmospheric depth of 17.6 g/cm^2.

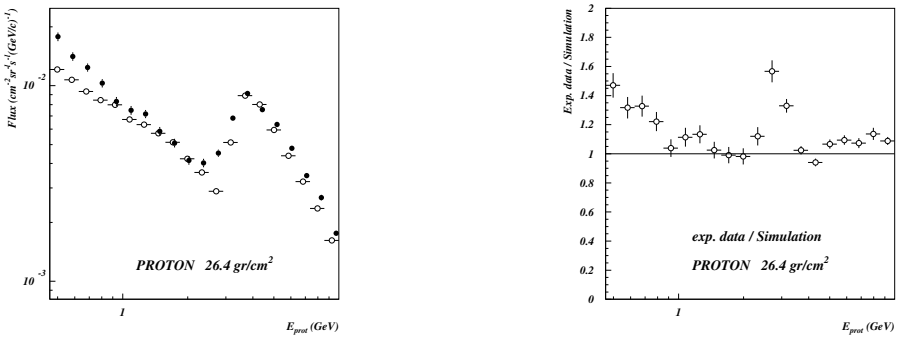

Figure 133: Atmospheric depth of 26.4 g/cm^2.

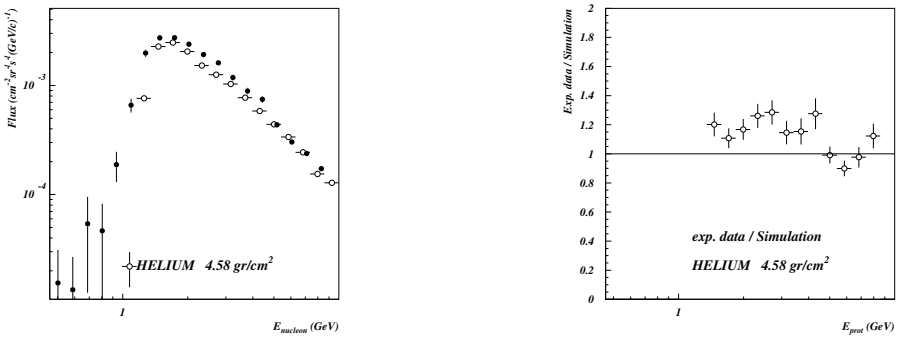

Figure 134: Atmospheric depth of 4.58 g/cm^2. Helium nuclei flux (open symbols) simulated using the primary spectrum AMS-BESS fit 2001 and compared with experimental data (black points). Experimental data/simulation ratio on the right. NRLMSISE-00 Model 2001 for the atmosphere. FLUKA 2005.6 with **DPMJET III + QMD** interaction model. BESS-2001 balloon flight.

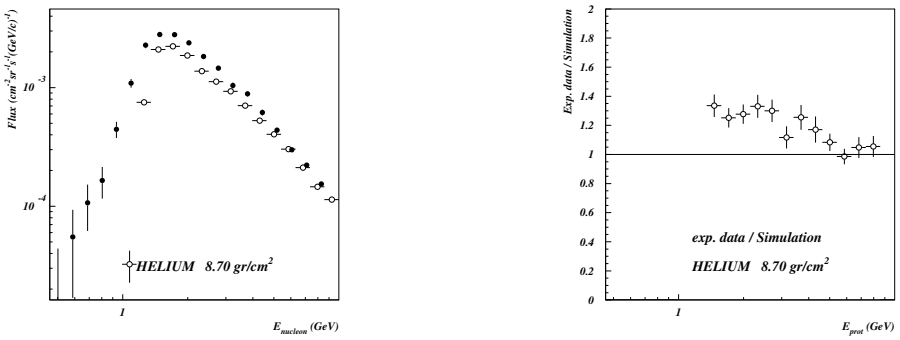

Figure 135: Atmospheric depth of 8.70 g/cm^2.

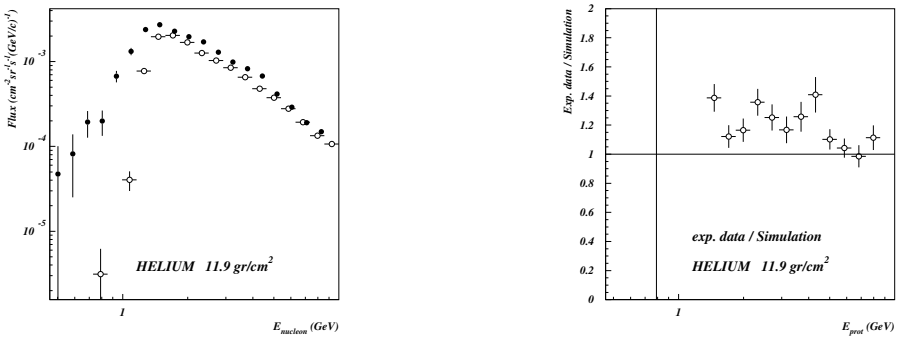

Figure 136: Atmospheric depth of 11.9 g/cm^2.

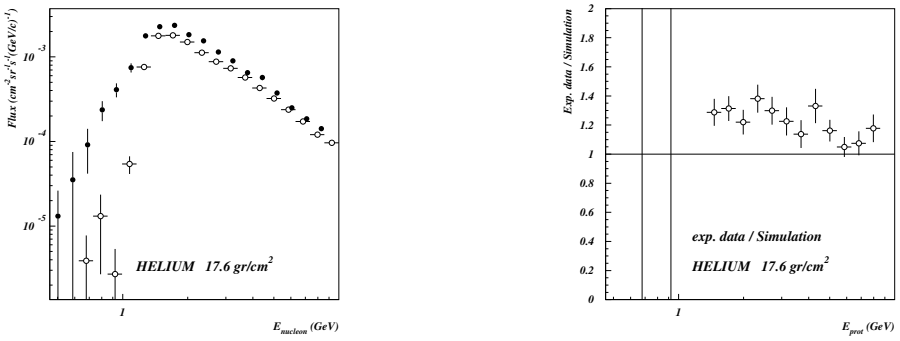

Figure 137: Atmospheric depth of 17.6 g/cm^2.

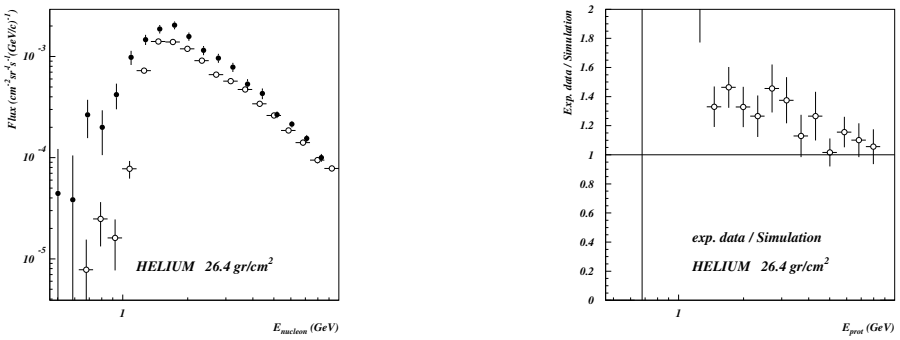

Figure 138: Atmospheric depth of 26.4 g/cm^2.

4.4 High energy muons

As told in Section 2.2, the L3+Cosmic experiment recorded 1.2×1010 atmospheric muon triggers in the energy range 20 GeV to 3 TeV during its operation in the years 1999 and 2000.
The L3+C experiment was located 450 m above sea level at a longitude of 6.02° E and a latitude of 46.25° N.
For these simulations we used the **High Energy All-nucleon Spectrum** primary spectrum (see Section 3.3.1) and we reproduced the muon fluxes related to different $cos\theta$ ranges recorded by the experiment.
In order to verify the consistency of our simulations we need a comparison with experimental data. The two distributions have different binning, so we decided to fit them and compare the obtained results. Experimental data and simulations (Figs. 139, 142, 145, 148, 151, 154, 157, 160) are fitted using the three parameters function:

$$\Phi(p_\mu) = P1 * p_\mu^{(-P2+P3*\log p_\mu)} \quad . \tag{56}$$

There is a good agreement between the two fits (<10% of difference) over the all energy range and for every $cos\theta$ value.

We have also accomplished a comparison between the simulated μ^+/μ^- ratio with the experimentally obtained value (Figs. 141, 144, 147, 150, 153, 156, 159, 162). The results seems to agree with experimental data for every $cos\theta$ value as well.

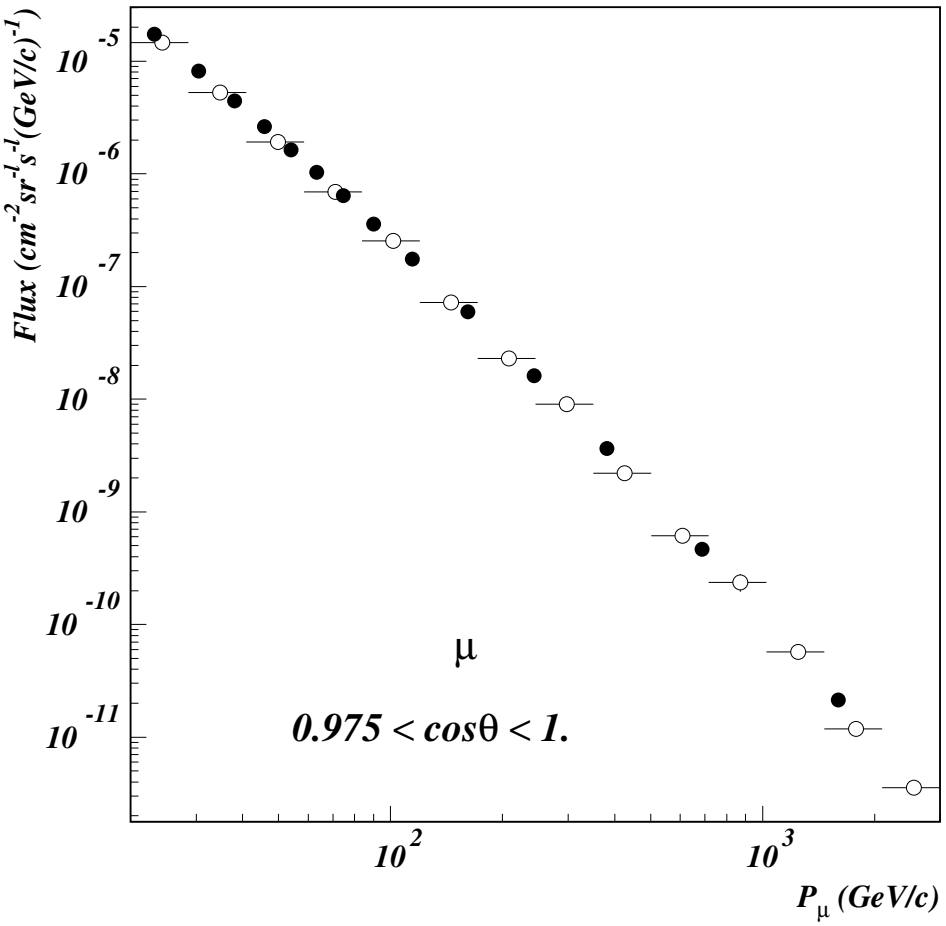

Figure 139: Muon fluxes at sea level. Vertical flux ($0.975 < cos\theta < 1.$). Black points are data and open symbols are simulation.

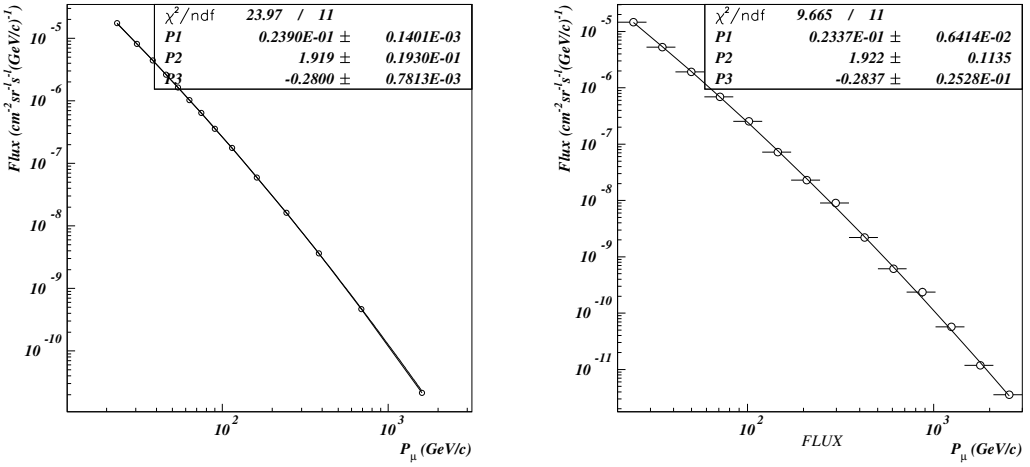

Figure 140: Muon fluxes at sea level. Vertical flux ($0.975 < cos\theta < 1.$). Data and simulation fit

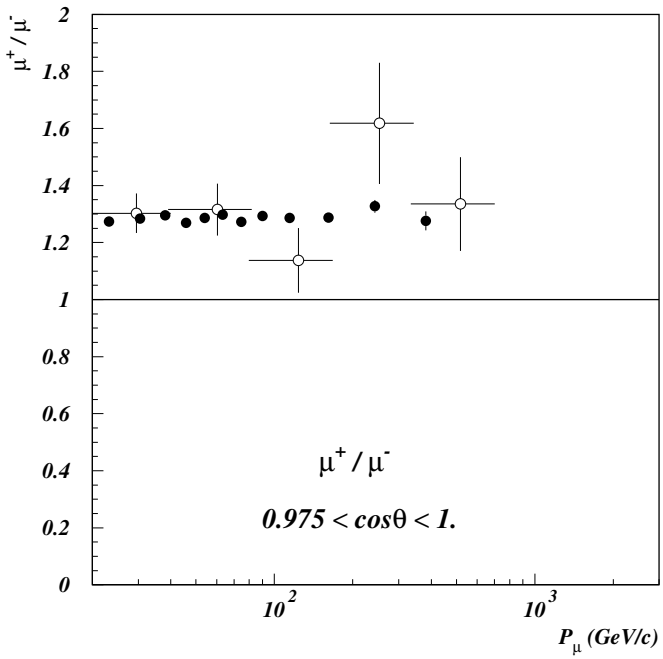

Figure 141: Muon fluxes ratio. Vertical flux ($0.975 < cos\theta < 1.$). Black points are data and open symbols are simulation.

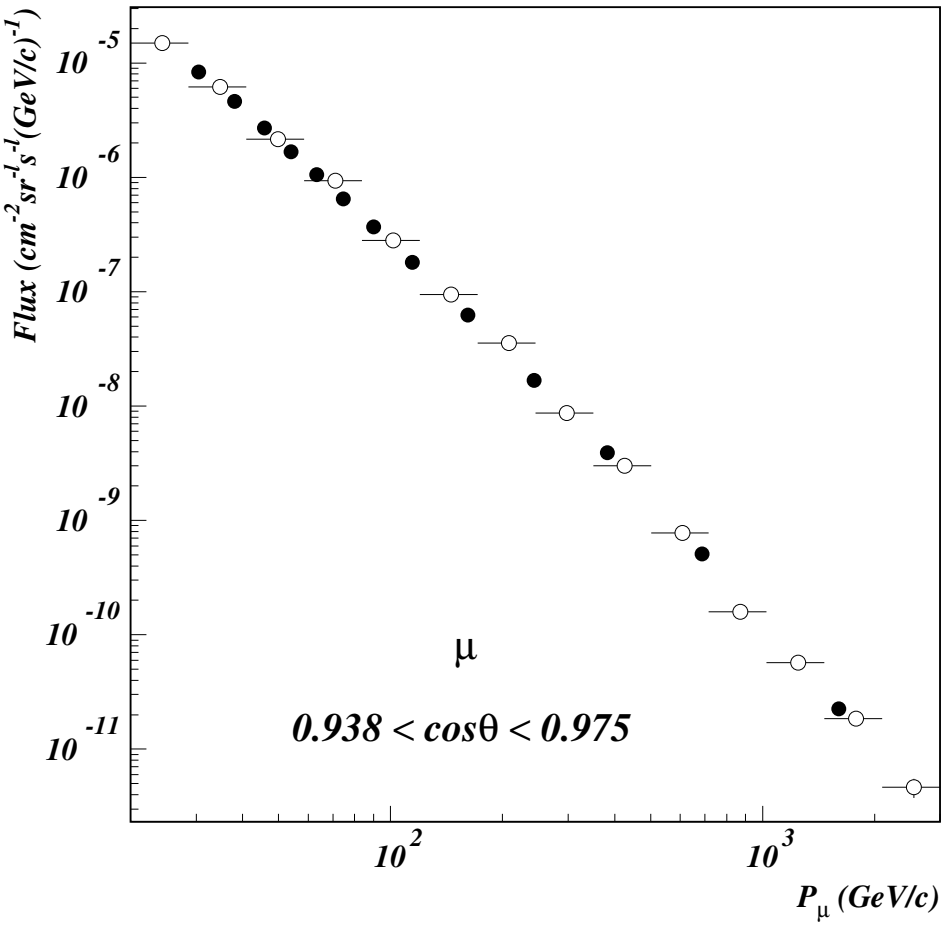

Figure 142: Muon fluxes at sea level. Flux $0.938 < cos\theta < 0.975$. Black points are data and open symbols are simulation.

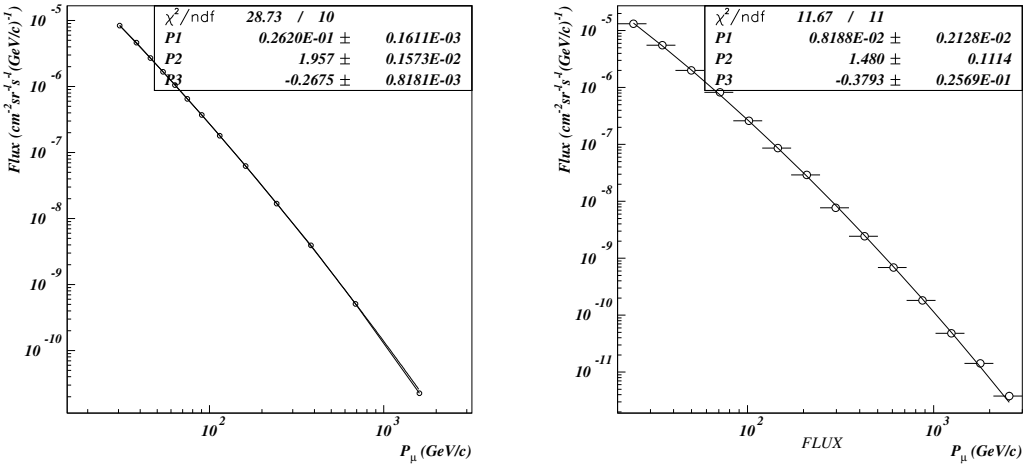

Figure 143: Muon fluxes at sea level. Flux $0.938 < cos\theta < 0.975$. Data and simulation fit

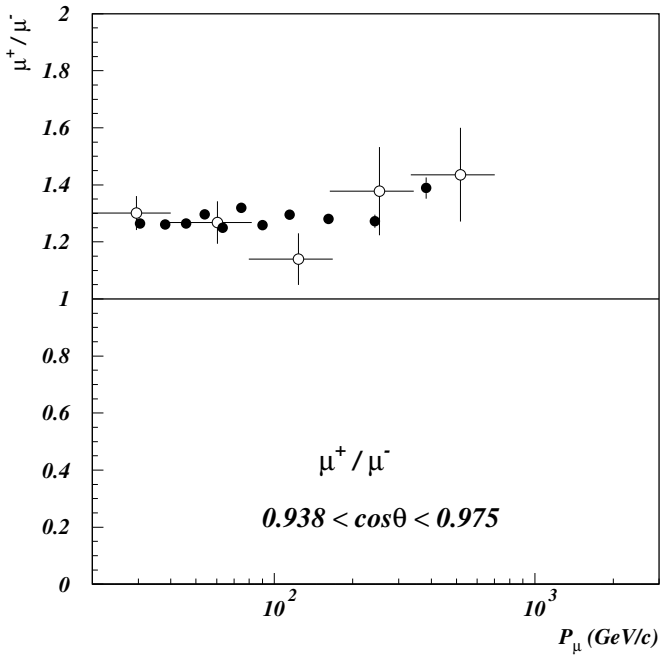

Figure 144: Muon fluxes ratio. Flux $0.938 < cos\theta < 0.975$. Black points are data and open symbols are simulation.

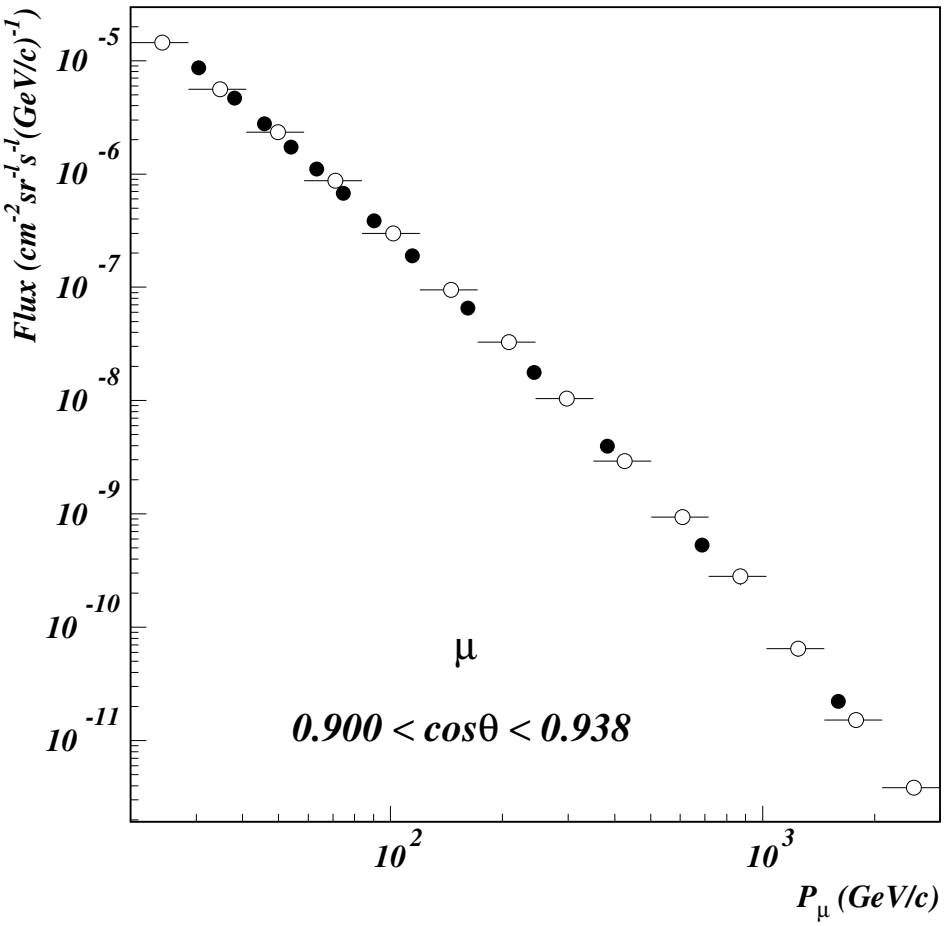

Figure 145: Muon fluxes at sea level. Flux $0.900 < cos\theta < 0.938$. Black points are data and open symbols are simulation.

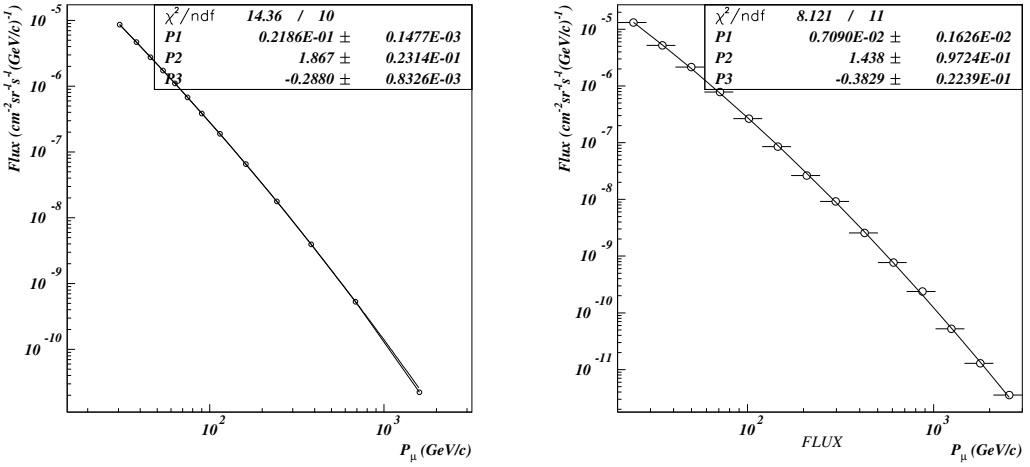

Figure 146: Muon fluxes at sea level. Flux $0.900 < cos\theta < 0.938$. Data and simulation fit

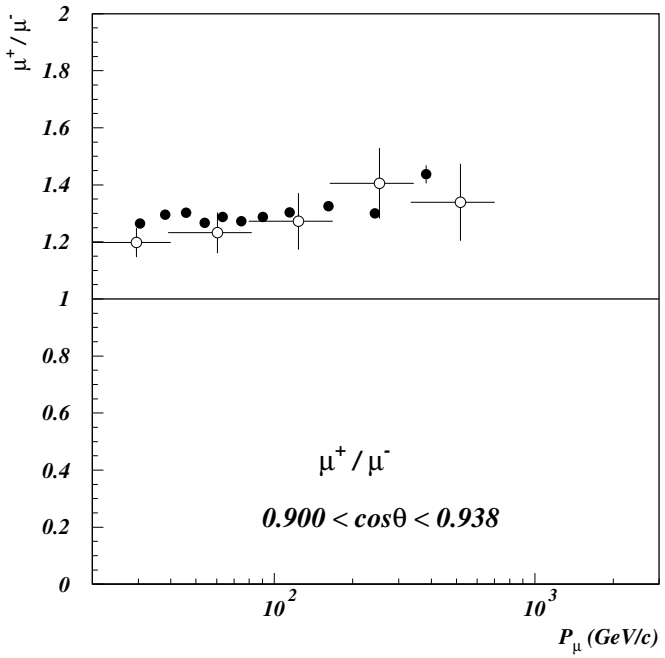

Figure 147: Muon fluxes ratio. Flux $0.900 < cos\theta < 0.938$. Black points are data and open symbols are simulation.

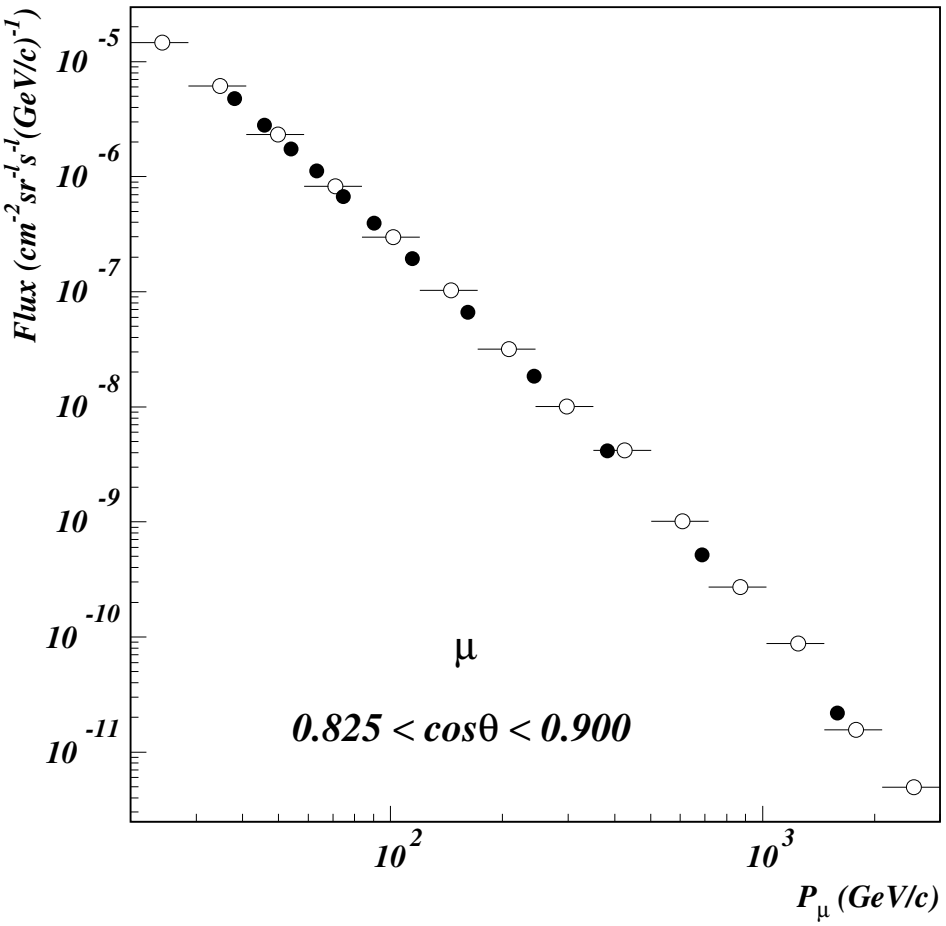

Figure 148: Muon fluxes at sea level. Flux $0.825 < cos\theta < 0.900$. Black points are data and open symbols are simulation.

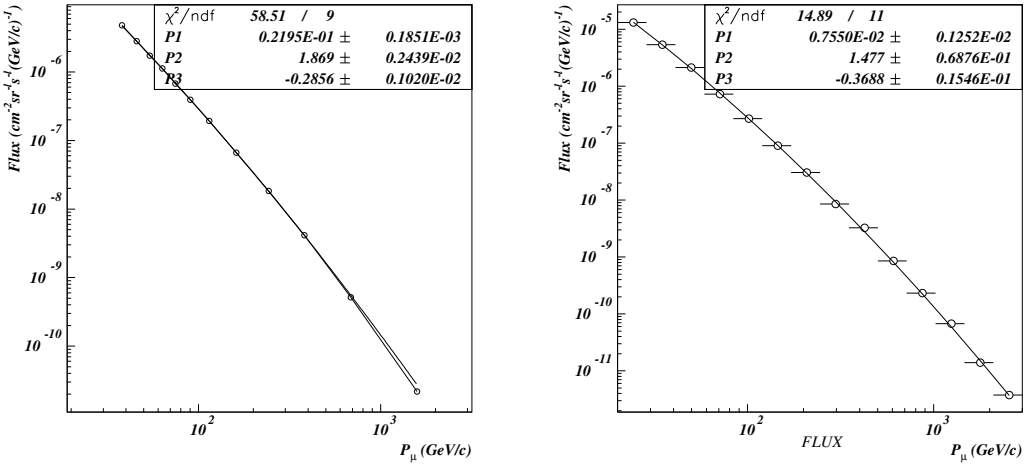

Figure 149: Muon fluxes at sea level. Flux $0.825 < cos\theta < 0.900$. Data and simulation fit

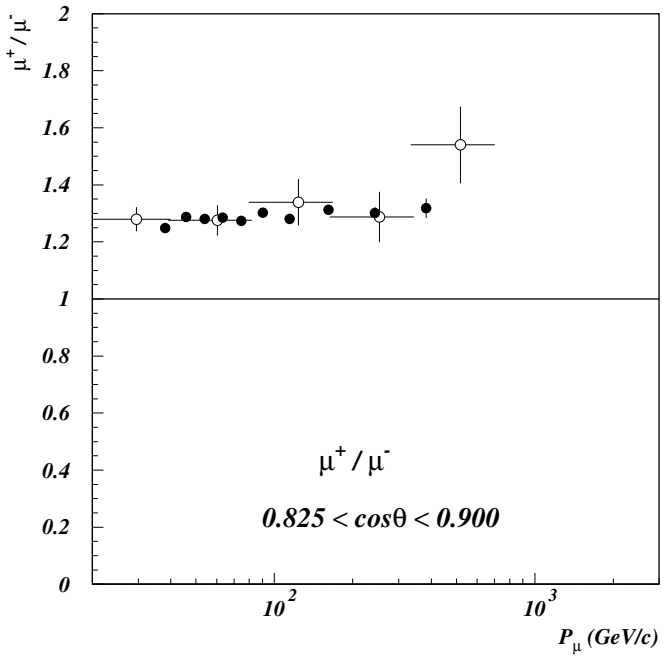

Figure 150: Muon fluxes ratio. Flux $0.825 < cos\theta < 0.900$. Black points are data and open symbols are simulation.

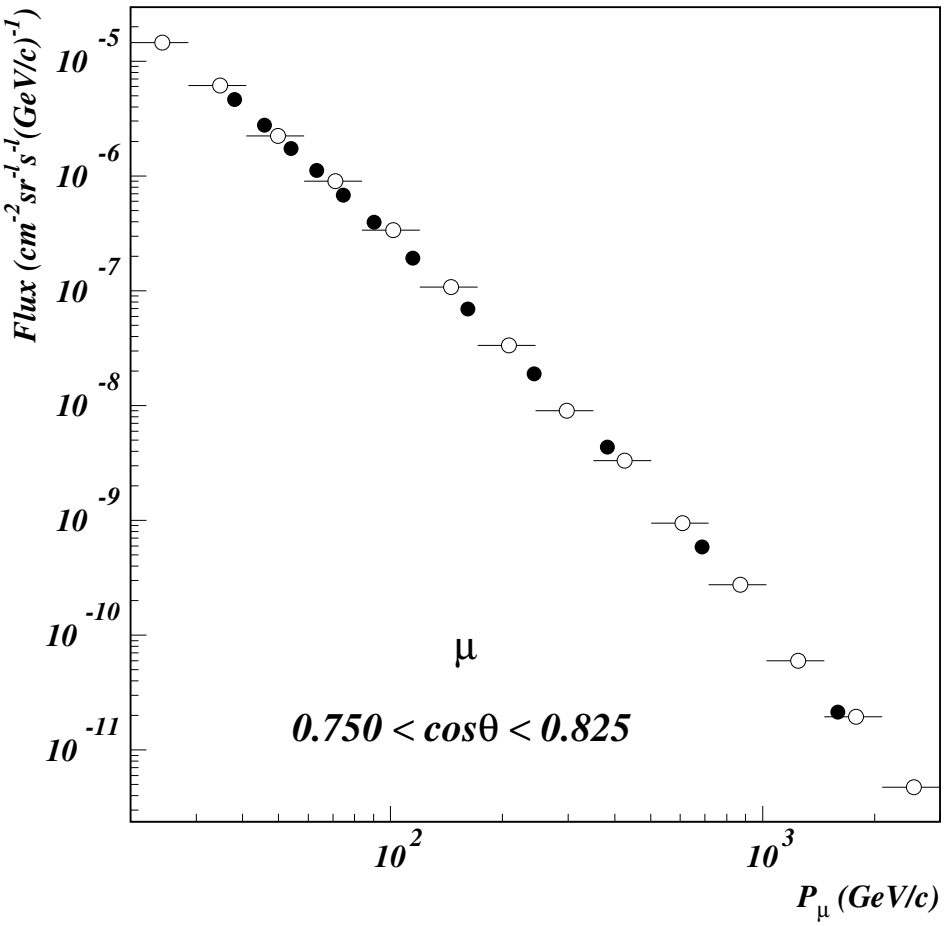

Figure 151: Muon fluxes at sea level. Flux $0.750 < cos\theta < 0.825$. Black points are data and open symbols are simulation.

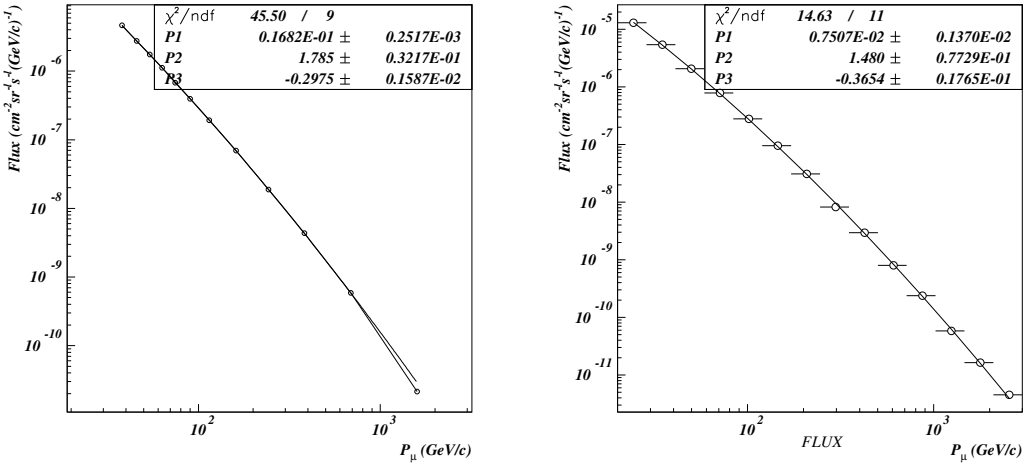

Figure 152: Muon fluxes at sea level. Flux $0.750 < cos\theta < 0.825$. Data and simulation fit

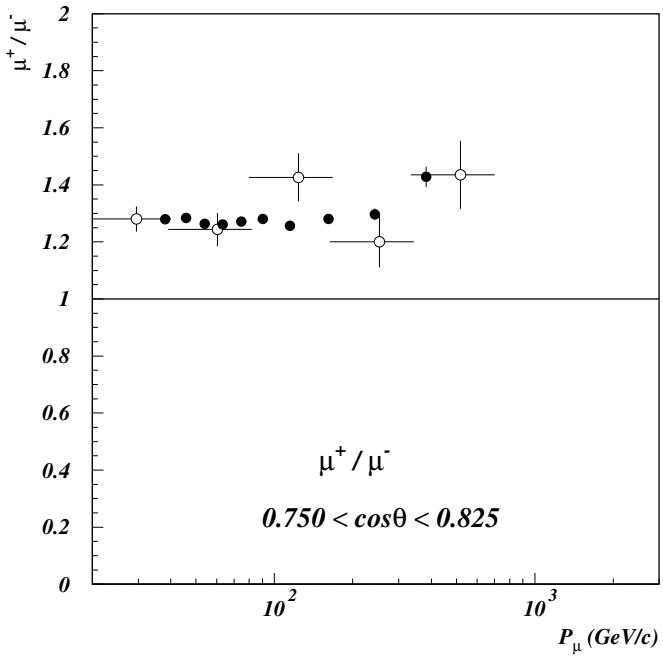

Figure 153: Muon fluxes ratio. Flux $0.750 < cos\theta < 0.825$. Black points are data and open symbols are simulation.

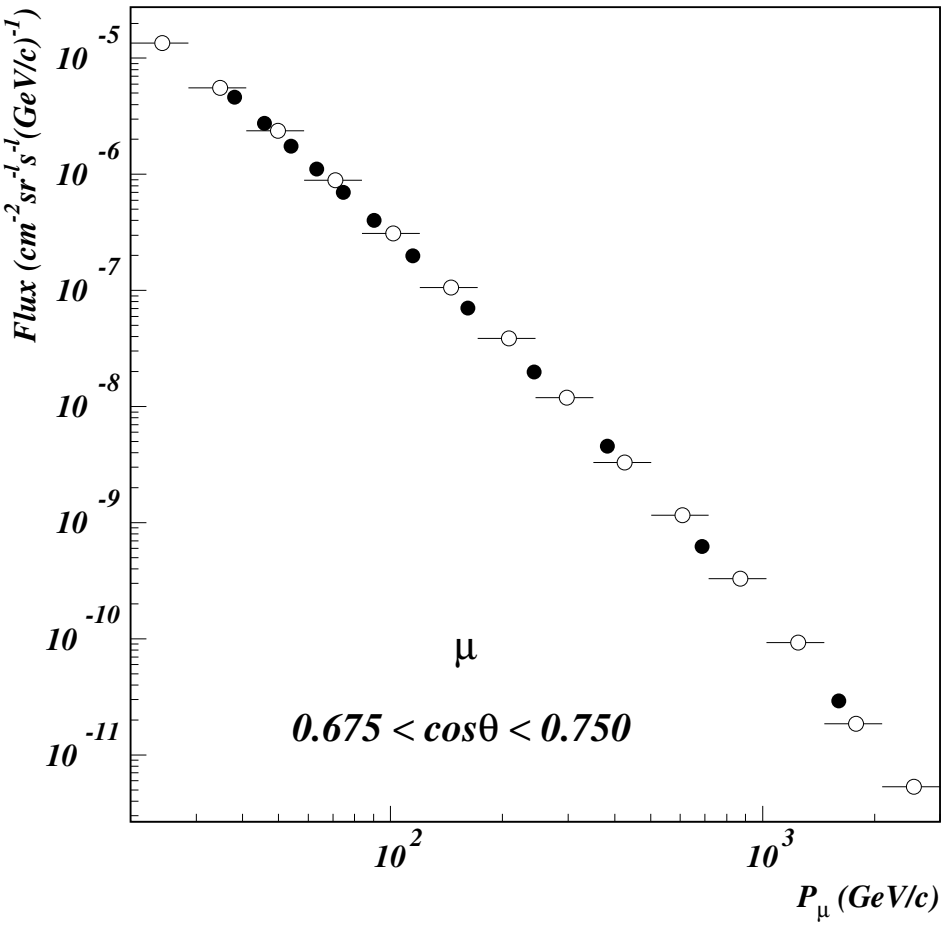

Figure 154: Muon fluxes at sea level. Flux $0.675 < cos\theta < 0.750$. Black points are data and open symbols are simulation.

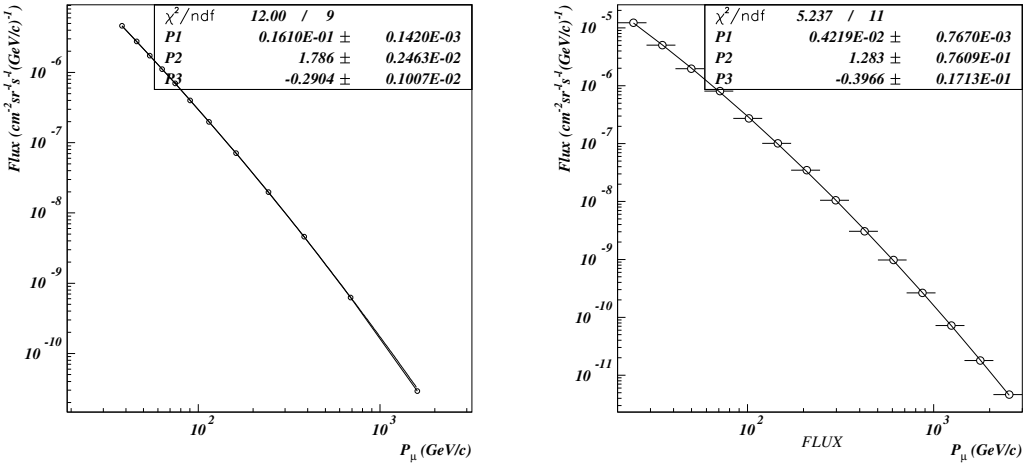

Figure 155: Muon fluxes at sea level. Flux $0.675 < cos\theta < 0.750$. Data and simulation fit

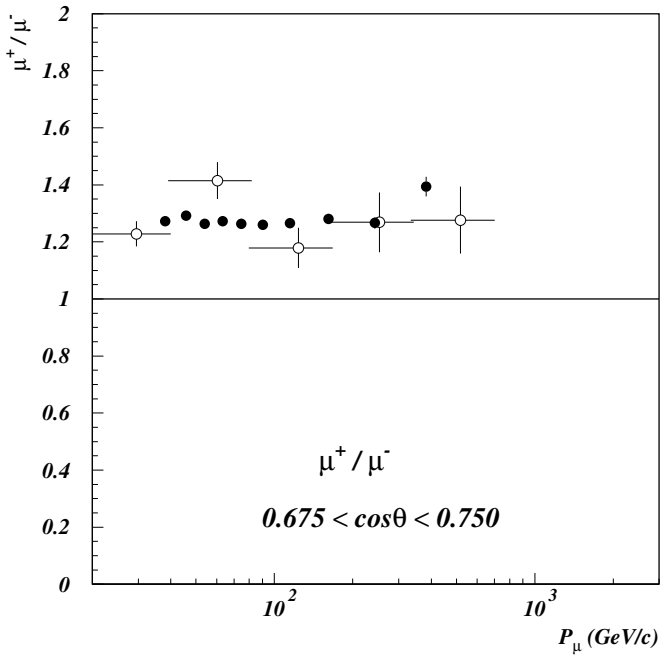

Figure 156: Muon fluxes ratio. Flux $0.675 < cos\theta < 0.750$. Black points are data and open symbols are simulation.

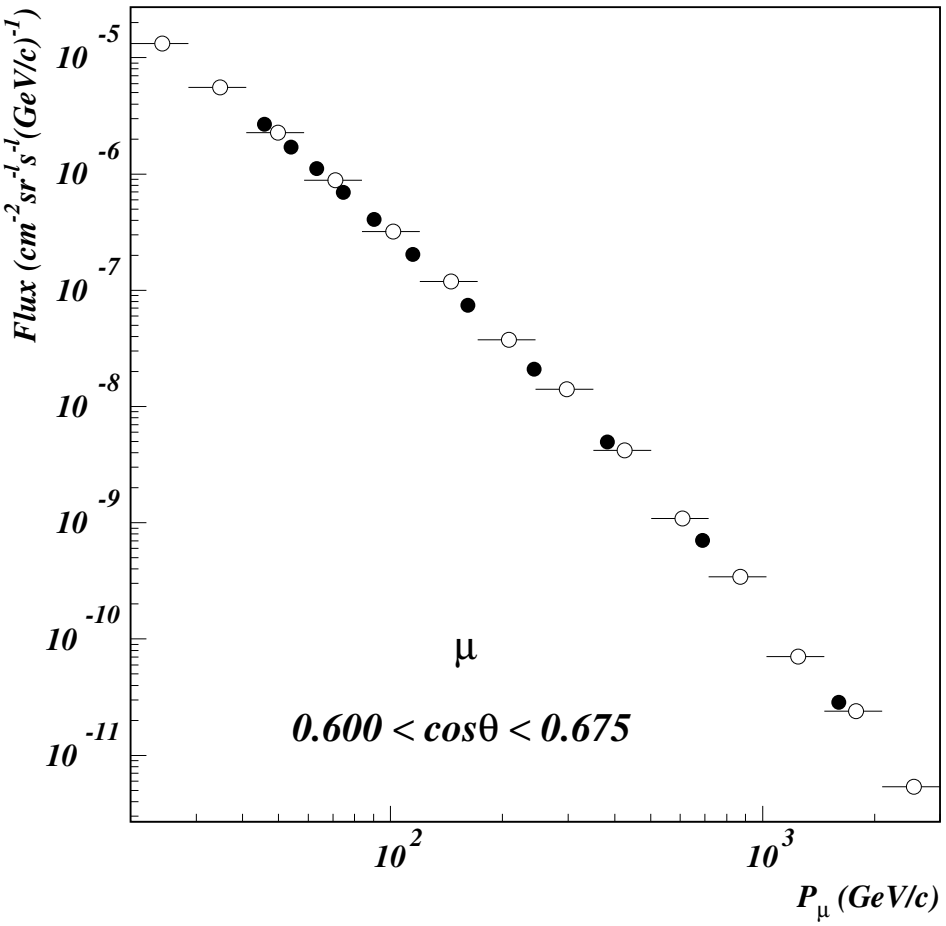

Figure 157: Muon fluxes at sea level. Flux $0.600 < cos\theta < 0.675$. Black points are data and open symbols are simulation.

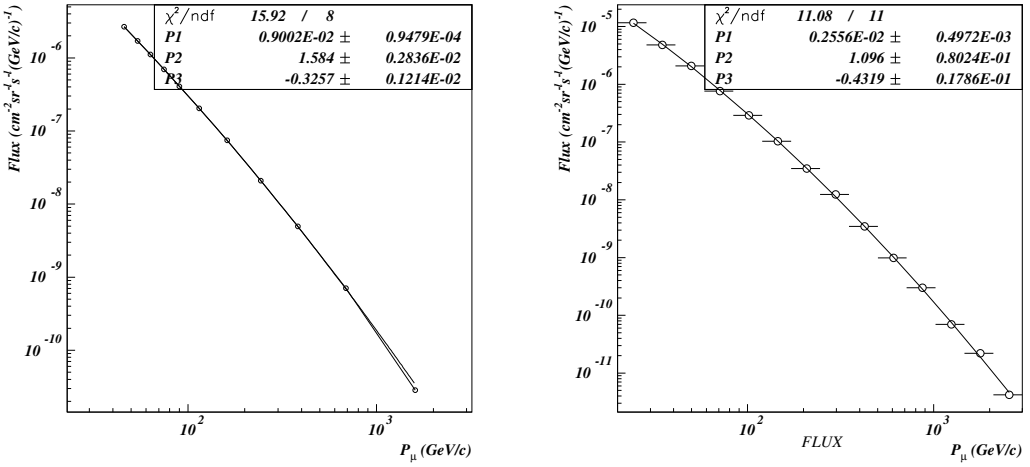

Figure 158: Muon fluxes at sea level. Flux $0.600 < cos\theta < 0.675$. Data and simulation fit

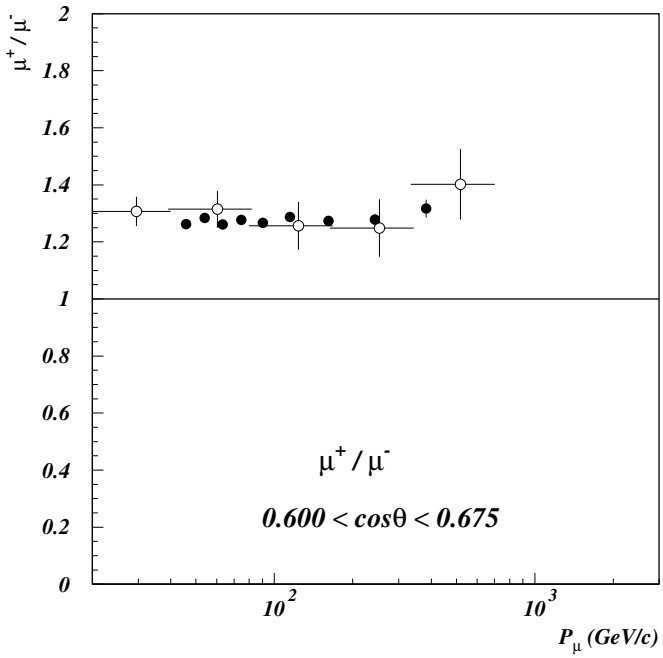

Figure 159: Muon fluxes ratio. Flux $0.600 < cos\theta < 0.675$. Black points are data and open symbols are simulation.

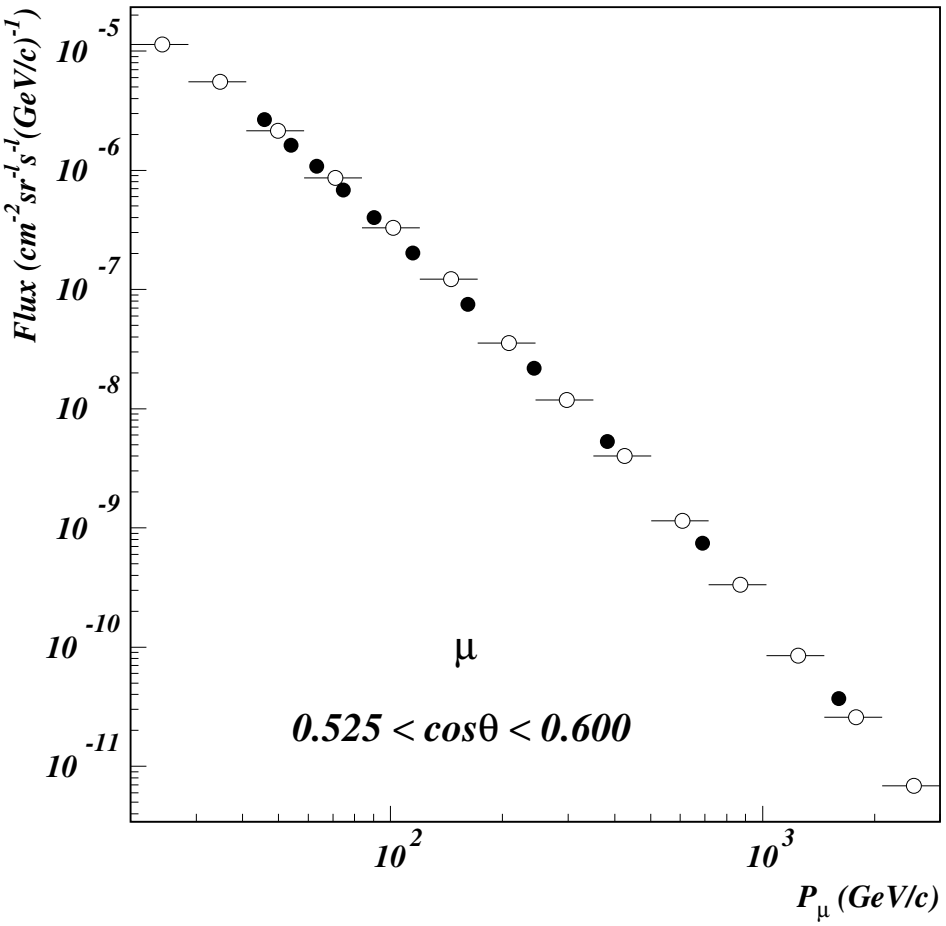

Figure 160: Muon fluxes at sea level. Flux $0.525 < cos\theta < 0.600$. Black points are data and open symbols are simulation.

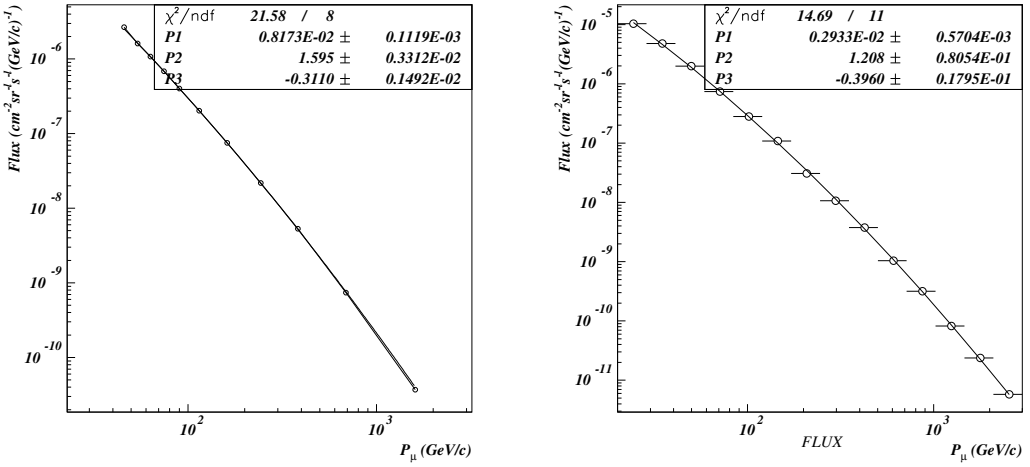

Figure 161: Muon fluxes at sea level. Flux $0.525 < cos\theta < 0.600$. Data and simulation fit

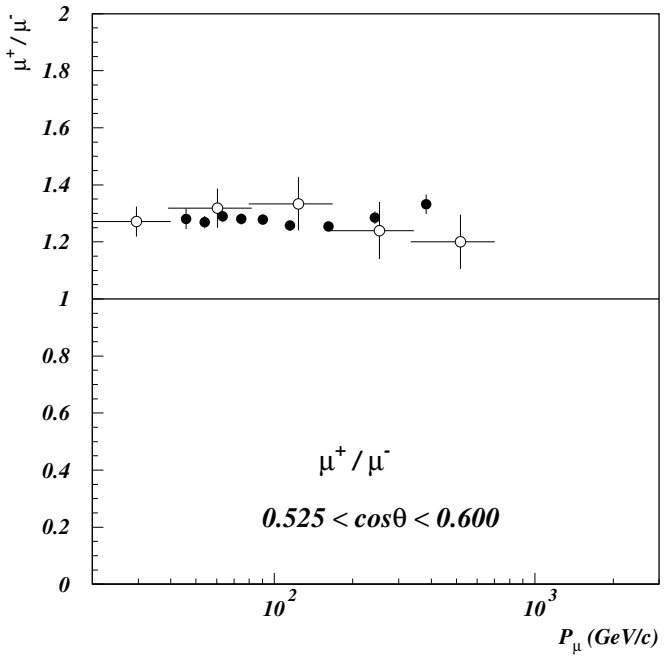

Figure 162: Muon fluxes ratio. Flux $0.525 < cos\theta < 0.600$. Black points are data and open symbols are simulation.

Conclusions

A complete calculation of particle fluxes in the atmosphere requires to take into account a lot of parameters and everyone of them has a weight in the final result. Therefore a comparison of simulated data with experiment is a rather difficult job, whose results do not depend just on the quality of the particle production model.
We have to consider the primary spectrum and composition of cosmic rays, the changing conditions in the solar wind magnetic field, the effects of geomagnetic cut-off on the primary spectrum, the Earth's atmosphere model at various depths, the three-dimensional development of the shower in the atmosphere and the bending due to the Earth's geomagnetic field.
For this reason the simulations and comparisons with experimental data used for this work have been chosen in different geographical location (different geomagnetic cut-off), different years (different solar modulation conditions) and different altitude in the atmosphere (from sea level to $\sim$36 km).
We have chosen the BESS experimental data for the lower energies and the analysis of cosmic muons in the L3 detector for the high energies.
We could investigate just a few different models of the primary spectrum and a couple of atmospheric models.
This work shows that FLUKA is in general successful in reproducing the features of the measured spectra. That's often not only qualitatively true but also quantitatively. On the other hand there are cases in which the quantitative comparison is not completely successful. Before entering into a detailed list of these cases, it is worthwhile remembering how difficult is to disentangle the effects due to the choice of primary model and those due to the hadronic physics model. This prevents us from taking strong conclusions in all cases.
Among the problematic cases we remark that the simulations presented for the BESS experiment data set show a lack of muon production: up to 30% for the lowest energies (below 1 GeV) and higher rigidity cut-off.
We have discarded the NASA Spectrum, since it is considered too high in normalization (see Section 3.3.1). The AMS-BESS fit 2001 looks closer to experimental data than the PrimaryCR fit 2005 almost in every simulation setup (Lynn Lake, Mt. Norikura and Ft. Sumner BESS balloon flight as well).
Regarding the atmospheric model, we decided to adopt the NRLMSISE-00 Model 2001, taking into account the local and seasonal variability of the atmosphere.
The simulation at Mt. Norikura presents a good shape reproduction but looks better at higher energies.

The muon simulation at high altitude (balloon flight) and comparison with data fulfill the expectations: presents a lack of muon production within 10%. In the high energy range (20 GeV - 3 TeV), the muon simulation obtained using the High Energy All-nucleon Spectrum and its comparison with L3+Cosmic data exhibits a good agreement (<10%) over the all energy range and for every $cos\theta$ value.

As a general final remark, we can say that the shape of the muon fluxes is close to the experimental data shape for different solar modulation condition and for high and low energy cut-off (Tsukuba vertical rigidity cut-off is 11.4 GV and Lynn Lake one is 0.4 GV) but the uncertainty on primary spectrum and his absolute normalization looks to be significant. In some cases these uncertainties are probably more important than those of the interaction model.

From data/simulation ratio for the BESS muon fluxes we can get a measurement of the reliability of the complete package (hadronic model plus primary spectrum, atmosphere...). We notice how this ratio exhibits a power low dependence with respect to the entire range of the secondary muon momentum, independently of the atmospheric model, interaction model or primary spectrum used in different simulation setups and data taking.
This is suggestive of a possible systematics in the component of the simulation package. Our conclusion is that such a power low scaling over the entire range of particle production, points out that the most probable candidate for the mismatches between simulation and data, especially at low energy, is the model of primary cosmic ray spectrum.
The improvement of this element of the cosmic ray FLUKA simulation package will be the next important goal of the collaboration.

Of course, there are other data concerning particles in atmosphere that could be considered, like the gamma ray fluxes in atmosphere, the neutron fluences and atmospheric neutrinos as well. The research concerning these components is already object of study by other FLUKA collaborators.

A Fluka 2003 vs. Fluka 2005.6

During this work, a new Fluka release came out: Fluka 2005.6.
The main difference with the previous version (Fluka 2003) is the use of PEANUT for π production that is extended up to 5 GeV.
Comparisons between different versions of primary spectrum and location (geomagnetic cut-off) show that the production in Fluka 2005.6 exceed the production in Fluka 2003 of about 5% in the whole energy range.

In the following I compare the same simulation done with the two version of the code. The experimental data (black points) are from BESS experiment in Lynn Lake '97 [41] (56.5° N, 101.0° W). The vertical cutoff rigidity is 0.4 GV.
For these simulations was used the PrimaryCR fit 2005 primary spectrum.

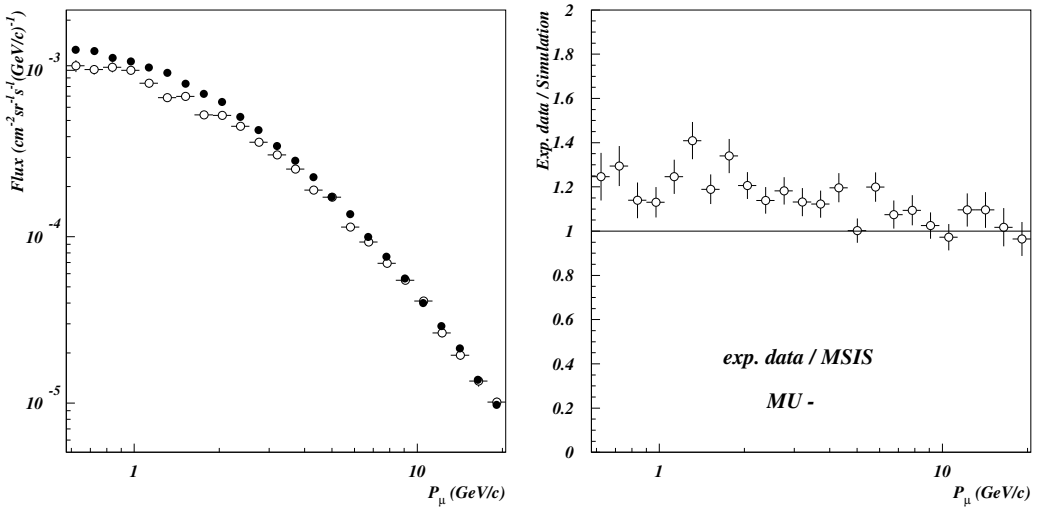

Figure 163: The μ^- flux simulated (open simbols) using the primary spectrum PrimaryCR fit 2005 and compared with experimental data (black points). Data/simulation ratio on the right. NRLMSISE-00 Model 2001 for the atmosphere. BESS Lynn Lake experiment ('97-'98-'99). Fluka 2003.

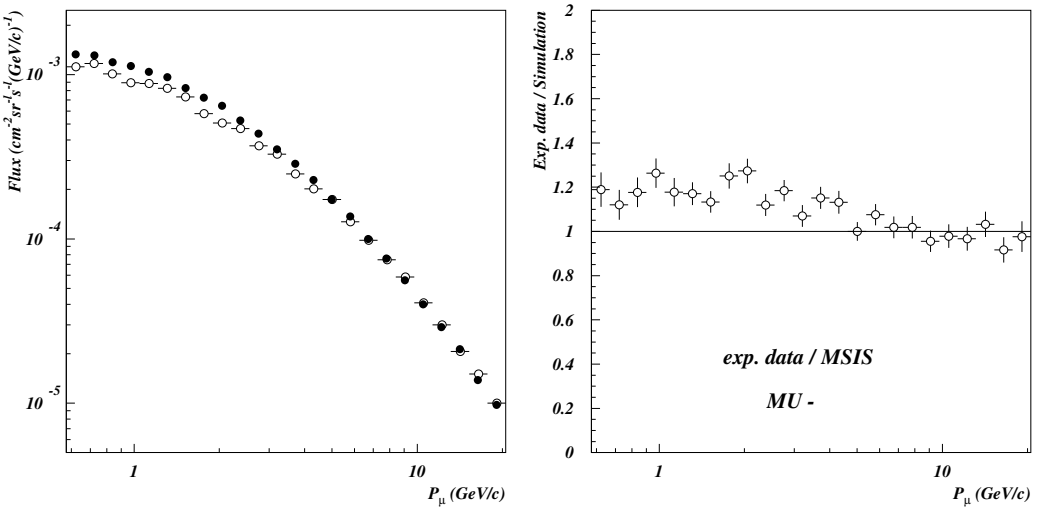

Figure 164: The μ^- flux simulated (open simbols) using the primary spectrum PrimaryCR fit 2005 and compared with experimental data (black points). Data/simulation ratio on the right. NRLMSISE-00 Model 2001 for the atmosphere. BESS Lynn Lake experiment ('97-'98-'99). Fluka 2005.6.

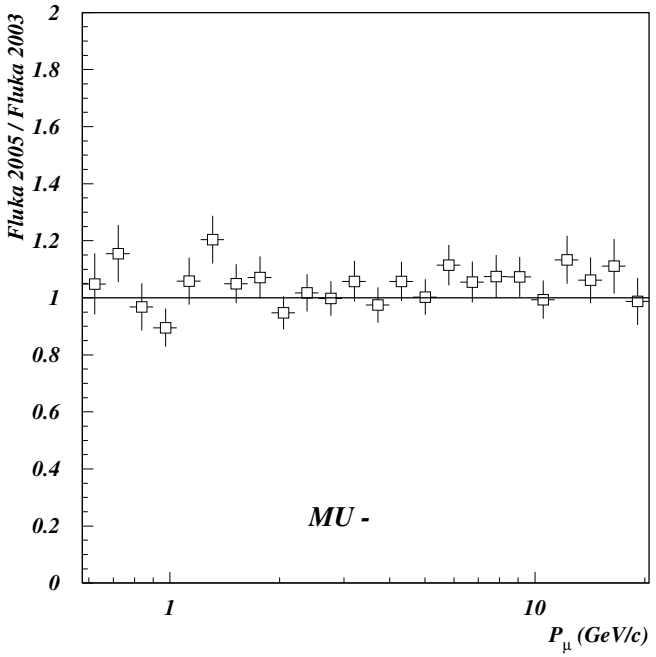

Figure 165: Comparison between Fluka 2003 and Fluka 2005 for negative muons

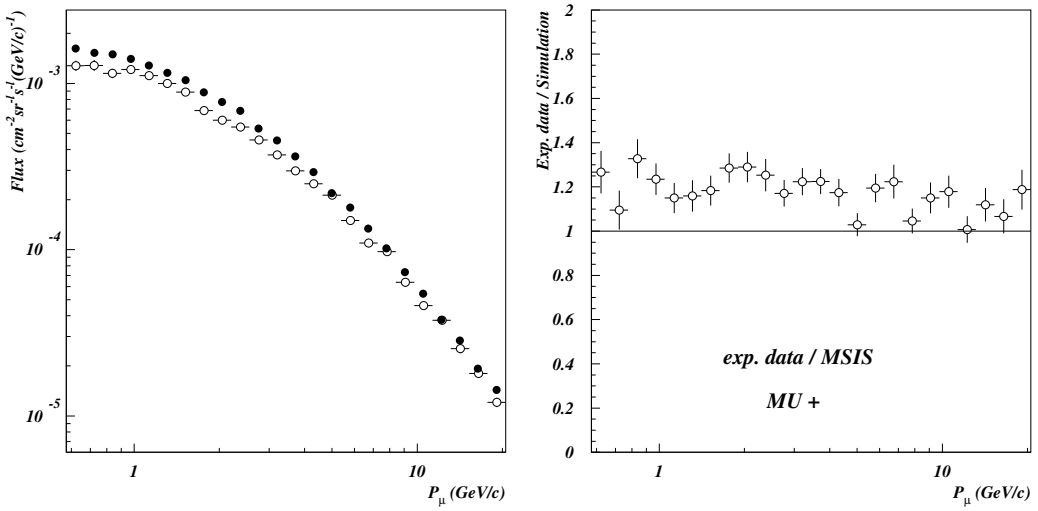

Figure 166: The μ^+ flux simulated (open simbols) using the primary spectrum PrimaryCR fit 2005 and compared with experimental data (black points). Data/simulation ratio on the right. NRLMSISE-00 Model 2001 for the atmosphere. BESS Lynn Lake experiment ('97-'98-'99). Fluka 2003.

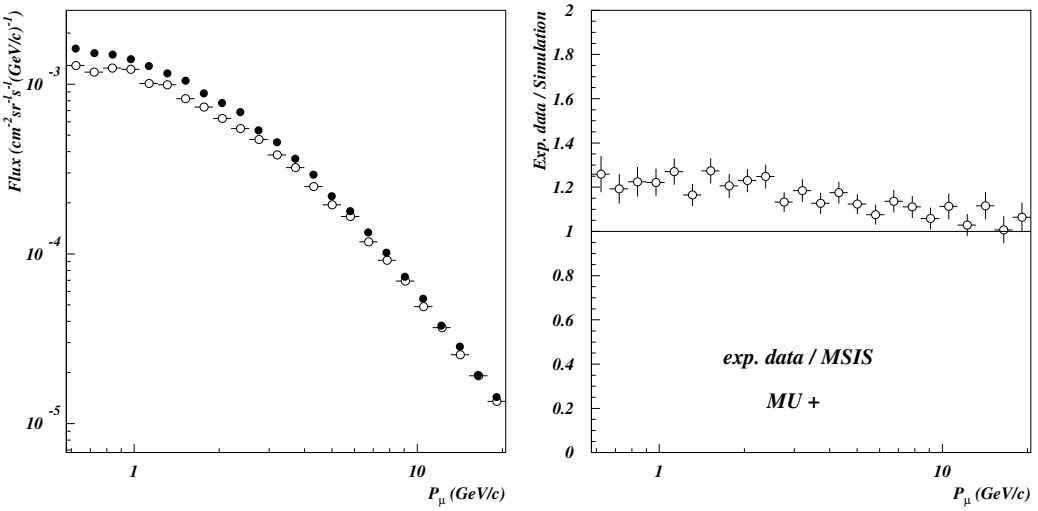

Figure 167: The μ^+ flux simulated (open simbols) using the primary spectrum PrimaryCR fit 2005 and compared with experimental data (black points). Data/simulation ratio on the right. NRLMSISE-00 Model 2001 for the atmosphere. BESS Lynn Lake experiment ('97-'98-'99). Fluka 2005.6.

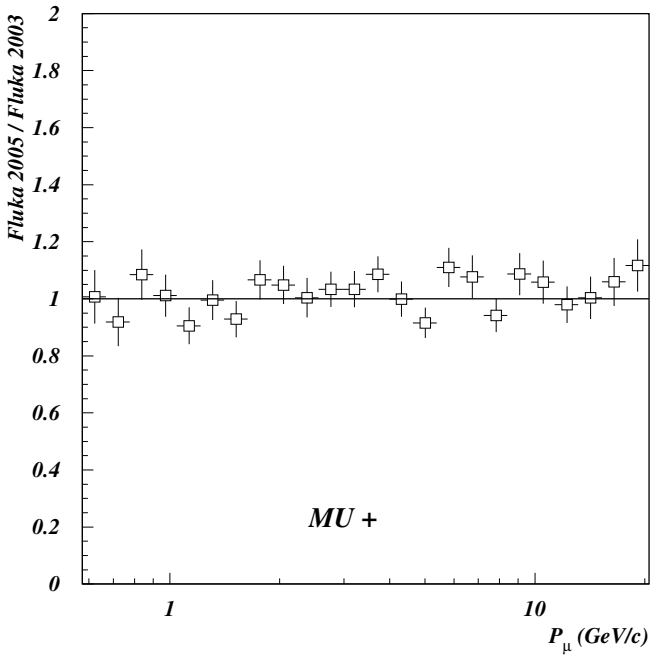

Figure 168: Comparison between Fluka 2003 and Fluka 2005 for positive muons

References

[1] "Cosmic Rays and Particle Physics".
Gaisser, T.K.
Cambridge University Press 1990

[2] "Semi-analytic approximations for production of atmospheric muons and neutrinos".
Gaisser, T.K.
Astropart. Phys.; Volume 16, Issue 3 , January 2002, Pages 285-294.

[3] "Atmospheric Neutrino Fluxes"
Thomas K. Gaisser
arXiv:astro-ph/0502380 v1 18 Feb 2005.

[4] "A new calculation of atmospheric neutrino fluxes"
Perkins, Donald Hill
Nucl. Phys., Dec 1993? . - 18 p

[5] "Review of Sources of Atmospheric Neutrinos" Nucl. Phys. B - Proceedings Supplements Volume: 91, Issue: 1-3, January, 2000, pp. 159-166 Lipari, Paolo.

[6] "Summary talk on atmospheric neutrinos" Nuclear Physics B - Proceedings Supplements Volume: 100, Issue: 1-3, May, 2001, pp. 153-158 Learned, John G.; Lipari, Paolo.

[7] "The FLUKA atmospheric neutrino flux calculation" G. Battistoni, A. Ferrari, T. Montaruli, P.R. Sala Astroparticle Physics, Volume 19, Issue 2 , May 2003, Pages 269-290.

[8] "A 3-dimensional calculation of the atmospheric neutrino fluxes" G. Battistoni, A. Ferrari, P. Lipari, T. Montaruli, P.R. Sala, T. Rancati. Astropart. Phys., Volume 12, Issue 4 , January 2000, Pages 315-333.

[9] "Hadronic interactions for atmospheric cascades" R. Engel, T.K. Gaisser, T. Stanev (Bartol Research Inst.) , P. Lipari (INFN, Rome & Rome U.) . Aug 2001. 4pp. Prepared for 27th International Cosmic Ray Conference (ICRC 2001), Hamburg, Germany, 7-15 Aug 2001. Published in Hamburg 2001, Cosmic ray 1381-1384.

[10] "A Monte Carlo simulation of cosmic rays interactions with Earth's atmosphere" Nuclear Physics B - Proceedings Supplements Volume: 110, July, 2002, pp. 182-185 Zuccon, P.

[11] "Atmospheric production of energetic protons, electrons and positrons observed in near Earth orbit" Astroparticle Physics Volume: 20, Issue: 2, November, 2003, pp. 221-234 Zuccon, P.; Bertucci, B.; Alpat, B.; Ambrosi, G.; Battiston, R.; Battistoni, G.; Burger, W.J.; et al.

[12] "Comparison of the FLUKA calculations with CAPRICE94 data on muons in atmosphere" G. Battistoni, A. Ferrari, T. Montaruli, P.R. Sala Astroparticle Physics - Vol: 17 Issue: 4, July, 2002; pp: 477-488.

[13] J.A. Simpson, Ann. Rev. Nucl. and Part. Sci. 33, 323 (1983).

[14] M. Boezio et al., Astrophys. J. 532, 653 (1999).

[15] W. Menn et al., Astrophys. J. 533, 281 (2000).

[16] R. Bellotti et al., Phys. Rev. D60, 052002 (1999).

[17] AMS Collaboration, Phys. Lett. B490, 27 (2000).

[18] T. Sanuki et al., Astrophys. J. 545, 1135 (2000).

[19] S. Haino et al., Phys. Lett. B594, 35 (2004).

[20] J.J. Engelmann et al., Astron. and Astrophys. 233, 96 (1990);
See also Cosmic Abundances of Matter (ed. C. Jake Waddington) A.I.P. Conf. Proc. No. 183 (1988), p. 111.

[21] S.W. Barwick et al., Astrophys. J. 498, 779 (1998).

[22] N.E. Yanasak et al., Astrophys. J. 563, 768 (2001).

[23] T. Hams et al., Astrophys. J. 611, 892 (2004).

[24] M. Boezio et al., Astrophys. J. 552, 635 (2000).

[25] J. Alcaraz et al., Phys. Lett. B484, 10 (2000).

[26] J.M. Clem and P.A. Evenson, Astrophys. J. 568, 216 (2002).

[27] M.A. DuVernois et al., Astrophys. J. 559, 296 (2000).

[28] M. Hof et al., Astrophys. J. 467, L33 (1996);
See also G. Basini et al., Proc. 26th Int. Cosmic Ray Conf., Salt Lake City, 3, 77 (1999).

[29] A.S. Beach et al., Phys. Rev. Lett. 87, 271101 (2001).

[30] J.W. Mitchell et al., Phys. Rev. Lett. 76, 3057 (1996).

[31] M. Boezio et al., Astrophys. J. 487, 415 (1997).

[32] S. Orito et al., Phys. Rev. Lett. 84, 1078 (2000).

[33] Y. Asaoka et al., Phys. Rev. Lett. 88, 51101 (2002).

[34] M. Sasaki et al., Nucl. Phys. B113, 202 (2002).

[35] H. Fuke et al., Phys. Rev. Lett. 95, 081101 (2005).

[36] R. Bellotti et al., Phys. Rev. D53, 35 (1996).

[37] M. Boezio et al., Phys. Rev. D62, 032007 (2000).

[38] S. Coutu et al., Phys. Rev. D62, 032001 (2000).

[39] D.H. Perkins, Astropart. Phys. 2, 249 (1994).

[40] A. Dar, Phys. Rev. Lett. 1982

[41] "Precise measurements of atmospheric muon fluxes with the BESS spectrometer" Astroparticle Physics Volume: 19, Issue: 1, April, 2003, pp. 113-126 Motoki, M.; Sanuki, T.; Orito, S.; Abe, K.; Anraku, K.; Asaoka, Y.; Fujikawa, M.; Fuke, H.; Haino, S.; et al.

[42] "Measurements of atmospheric muon spectra at mountain altitude" Physics Letters B Volume: 541, Issue: 3-4, August 15, 2002, pp. 234-242 Sanuki, T.; Fujikawa, M.; Abe, K.; Anraku, K.; Asaoka, Y.; Fuke, H.; Haino, S.; Imori, M.; Izumi, K.; et al.

[43] "Erratum to: Measurements of atmospheric muon spectra at mountain altitude: [Phys. Lett. B 541 (2002) 234]" Physics Letters B Volume: 581, Issue: 3-4, February 19, 2004, pp. 272-273 Sanuki, T.; Fujikawa, M.; Abe, K.; Anraku, K.; Asaoka, Y.; Fuke, H.; Haino, S.; Imori, M.; Izumi, K.; et al.

[44] "Measurements of proton, helium and muon spectra at small atmospheric depths with the BESS spectrometer" Physics Letters B Volume: 564, Issue: 1-2, July 3, 2003, pp. 8-20 Abe, K.; Sanuki, T.; Anraku, K.; Asaoka, Y.; Fuke, H.; Haino, S.; Ikeda, N.; Imori, M.; Izumi, K.; et al.

[45] M.A. Shea et al., in: Proceedings of 27th ICRC 2001, Hamburg, 2001, p. 4063.

[46] World Data Center for Geomagnetism, Kyoto University, Available from: http://swdcdb.kugi.kyoto-u.ac.jp/trans/index.html.

[47] S. Sagisaka, IL NUOVO CIMENT 9C, 1986, p. 809.

[48] NASA/Marshall Space Flight Center, Available from: $http://wwwssl.msfc.nasa.gov/ssl/pad/solar/sunspots.htm.$

[49] University of Chicago, Neutron Monitor Datasets, Available from: $http://ulysses.uchicago.edu/NeutronMonitor/neutron\_mon.html.$

[50] T. Sanuki et al., Astrophys. J. 545 (2000) 1135.

[51] AMS Collaboration, J. Alcaraz et al., Phys. Lett. B 490 (2000) 27.

[52] AMS Collaboration, J. Alcaraz et al., Phys. Lett. B 494 (2000) 193.

[53] M. Motoki et al., astro-ph/0205344, submitted to Astropart. Phys.

[54] S. Orito, in: J. Nishimura, K. Nakamura, A. Yamamoto, Proc. ASTROMAGWorkshop, KEK Report KEK87-19, KEK, Ibaraki, 1987, p. 111..

[55] A. Yamamoto et al., Adv. Space Res. 14 (1994) 75.

[56] Y. Asaoka et al., Nucl. Instrum. Methods A 416 (1998) 236.

[57] Y. Ajima et al., Nucl. Instrum. Methods A 443 (2000) 71.

[58] Y. Shikaze et al., Nucl. Instrum. Methods A 455 (2000) 596.

[59] J.D. Sullivan, Nucl. Instrum. Methods 95 (1971) 5.

[60] R. Brun et al., GEANt Detector Description and Simulation Tool, CERN program library, CERN, Geneva, 1994.

[61] M.P. De Pascal et al., J. Geophys. Res. 98 (1993) 3501.

[62] J. Kremer et al., Phys. Rev. Lett. 83 (1999) 4241.

[63] E.S. Seo, et al., in: Proceedings of 25th International Cosmic-Ray Conference, Durban, Vol. 3, 1997, p. 337.

[64] I.J. Engelmann, et al., Astron. Astrophys. (1996) 233.

[65] S.A. Stephens, in: Proceedings of 17th International Cosmic-Ray Conference, Paris, Vol. 4, 1981, p. 282.

[66] J.D. Sullivan, Nucl. Instrum. Methods 95 (1971) 5.

[67] S. Roeseler, et al., hep-ph/0012252, unpublished.

[68] M. Honda, et al., in: Proceedings of 27th International Cosmic-Ray Conference, Hamburg, 2001, p. 162; M. Honda, et al., private communication.

[69] 29th International Cosmic Ray Conference Pune (2005) 00, 101-106 "Cosmic Ray Observation and Results from Experiments Using LEP Detectors at CERN" P. Le Coultre, Institute of Particle Physics, ETH, CH-8093 Zurich, Switzerland; Pierre.Le.Coultre@CERN.ch.

[70] "Measurement of the Atmospheric Muon Spectrum from 20 to 3000 GeV" The L3 Collaboration arXiv:hep-ex/0408114 v1 23 Aug 2004.

[71] "L3+C: Selected Results" P. Le Coultre and the L3+C collaborationa; CERN, CH-1211 Geneva, Switzerland Nuclear Physics B - Proceedings Supplements Volume 151, Issue 1 , January 2006, Pages 314-321.

[72] "The L3+Cosmics experiment" P. Le Coultre Nuclear Physics B - Proceedings Supplements Volume 122 , July 2003, Pages 161-169 Proceedings of the 12th International Symposium on Very High Energy Cosmic Ray Interactions.

[73] B.Adeva et al., Nucl.Instr. Meth. A289 (1990) 35

[74] O. Adriani et al., Nucl.Instr.and Meth. A488 (2002) 209

[75] O. C. Allkofer, K. Carstensen and D.W. Dau, Phys. Lett. B36 (1971) 425

[76] C. A. Ayre et al., J. Phys.G1 (1975) 584

[77] T. Sanuki et al., Phys.Lett. B541 (2002) 234 [Erratum-ibid. B581 (2004) 272]

[78] T. Hebbeker and C. Timmermans, Astropart. Phys. 18 (2002) 107.

[79] R. Engel, T. K. Gaisser, P. Lipari and T. Stanev, in Proceedings of the 27th ICRC (Hamburg, 7-15 Aug, 2001) 1381.

[80] Service de Climatologie, Geneva.

[81] O. C. Allkofer, K. Carstensen and D. W. Dau, Phys. Lett. B 36 (1971) 425.

[82] C. A. Ayre et al., J. Phys. G 1 (1975) 584.

[83] B. J. Bateman et al., Phys. Lett. B 36 (1971) 144.

[84] P. J. Green et al., Phys. Rev. D 20 (1979) 1598.

[85] M. P. De Pascale et al., J. Geophys. Res. 98 (1993) 3501.

[86] CAPRICE Collaboration, J. Kremer et al., Phys. Rev. Lett. 83 (1999) 4241.

[87] CAPRICE Collaboration, M. Boezio et al., Phys. Rev. D 67 (2003) 072003.

[88] BESS Collaboration, T. Sanuki et al., Phys. Lett. B 541 (2002) 234 [Erratum-ibid. B 581 (2004) 272].

[89] BESS Collaboration, S. Haino et al., 'Measurements of primary and atmospheric cosmic-ray spectra with the BESS-TeV spectrometer' [arXiv:astro-ph/0403704].

[90] A. Fassò, A. Ferrari, J. Ranft, and P.R. Sala, *FLUKA: Status and Prospective for Hadronic Applications*, in Proceedings of the MonteCarlo 2000 Conference, Lisbon, October 23–26 2000, A. Kling, F. Barão, M. Nakagawa, L. Távora, P. Vaz eds., Springer-Verlag Berlin, 955 (2001); A. Ferrari, and P.R. Sala, *The Physics of High Energy Reactions*, in Proceedings of Workshop on Nuclear Reaction Data and Nuclear Reactors Physics, Design and Safety, A. Gandini, G. Reffo eds., Trieste, Italy, April 1996, **2**, 424 (1998).

[91] A. Rubbia "NUX- neutrino generator", 1st Workshop on Neutrino - Nucleus Interactions in the Few GeV Region (NuInt01), Tsukuba, Japan, 13-16 Dec 2001,
neutrino.kek.jp/nuint01/slide/Rubbia.1.pdf

[92] E. Gadioli, and P.E. Hodgson, *Pre-equilibrium Nuclear Reactions*, Clarendon Press, Oxford, (1992).

[93] J. J. Griffin, Phys. Rev. Lett., **17**, 438 (1966).

[94] V.F. Weisskopf, Phys. Rev., **52**, 295 (1937).

[95] E. Fermi, Prog. Theor. Phys., **5**, 1570 (1950).

[96] M. Epherre and E. Gradsztajn, J. Physique, **18**, 48 (1967).

[97] A. Ferrari, P.R. Sala, J. Ranft, and S. Roesler, Z. Phys., **C71**, 75 (1996).

[98] M.E. Grypeos, G.A. Lalazissis, S.E. Massen and C.P. Panos, J. Phys., **G17**, 1093 (1991).

[99] L.R.B. Elton, *Nuclear Sizes*, Oxford University Press, Oxford (1961).

[100] W.D. Myers, Nucl. Phys., **A204**, 465 (1973).

[101] W.D. Myers, *Droplet Model of Atomic Nuclei*, IFI/Plenum Data Company, New York (1977).

[102] C.M. Kormanyos et al., Phys. Rev., **C51**, 669 (1995).

[103] T. Ericson and W. Weise, *Pions and Nuclei*, Clarendon Press, Oxford, (1988).

[104] Phase shift solutions KH78, KH80, in *Landolt-Börnstein , new series* , **Vol. 9, part II**, Springer-Verlag, (1983).

[105] E. Oset, and L.L. Salcedo, Nucl. Phys., **A468**, 631 (1987).

[106] J.N. Ginocchio, Phys. Rev., **C17**, 195 (1978).

[107] M.J. Vicente Vacas, and E. Oset, Nucl. Phys., **A568**, 855 (1994).

[108] A. Bohr, B.R. Mottelson, *Nuclear Structure*, **Vol. 1**, W.A. Benjamin, Inc. (1969).

[109] L. Stodolski, Proc. of the *Vth Intern. Coll. on Multiparticle Reactions*, Oxford, 577 (1975).

[110] For a review of Regge theory applied to high energy scattering see P.D.B. Collins, An Introduction to Regge Theory and High Energy Physics, Cambridge University Press, Cambridge, 1977.

[111] A. Capella et al., Z. Phys. C 3 (1980) 329;
A. Capella, J. Tran, Thanh Van, Phys. Lett. B 93 (1980) 146;
A. Capella et al., Phys. Rep. 236 (1994) 225.

[112] T. Sjostrand, CERN Report CERN-TH 6488/92, 1992.

[113] S. Ritter, Comput. Phys. Commun. 31 (1984) 393;
J. Ranft, S. Ritter, Acta Phys. Pol. B 11 (1980) 259.

[114] A.B. Kaidalov, O.I. Piskunova, Z. Phys. C 30 (1986) 141; A. Capella et al., Z. Phys. C 70 (1996) 507.

[115] K. Goulianos, Phys. Rep. 101 (1983) 169.

[116] S. Roesler et al., Z. Phys. C 59 (1993) 481;
J. Ranft, S. Roesler, Z. Phys. C 62 (1994) 329.

[117] K. Hahn, J. Ranft, Phys. Rev. D 41 (1990) 1463;
F.W. Bopp et al., Phys. Rev. D 49 (1994) 3236;
P. Aurenche et al., Phys. Rev. D 45 (1992) 92.

[118] A. Kaidalov, Phys. Lett. B 117 (1982) 459;
A. Kaidalov, K.A. Ter-Martirosyan, Phys. Lett. B 117 (1982) 247.

[119] For a wide review of FLUKA benchmarks, see Proceeding of the 1st International Workshop on Space Radiation Research and 11th NASA Space Radiation Health Investigators Workshop, Arona, Italy, May 2000.

[120] T. Abbott et al., Phys. Rev. D 45 (11) (1992) 3906.

[121] T. Eichten et al., Nucl. Phys. B 44 (1972) 333.

[122] H.W. Atherton, CERN 80 07, 1980.

[123] G. Ambrosini et al., Phys. Lett. B 425 (1988) 208.

[124] J. Ranft, "Dual Parton Model at cosmic ray energies", Phys. Rev. D51, 64 (1995).

[125] A. Empl, A. Fass'o, A. Ferrari, et al., "Progress and Applications of FLUKA", Proc. ANS Radiation Protection & Shielding Division 12th Topical Meeting, Santa Fe, New Mexico, USA, April 14 18 2002, (6 pages, published in electronic format)

[126] S. Roesler, R. Engel and J. Ranft, "The Monte Carlo Event Generator DPMJET-III", Proc. Monte Carlo 2000 Conference, Lisbon, October 23 26 2000, A. Kling, F. Barão, M. Nakagawa, L. T*á*vora, P. Vazeds., Springer-Verlag Berlin, 1033 (2001).

[127] H. Sorge, H. St*ö*cker, and W. Greiner, "Poincar*é* invariant hamiltonian dynamics: modelling multihadronic interactions in a phase space approach", Ann. of Phys. 192, 266 (1989).

[128] H. Sorge, "Flavor production in Pb(160 AGeV) on Pb collisions: Effect of color ropes and hadronic rescattering", Phys. Rev. C52, 3291 (1995).

[129] "Measurement of the production cross-section of positive pions in p-Al collisions at 12.9 GeV/c"; HARP Collaboration
Nucl. Phys. B; Volume 732, Issues 1-2 , 2 January 2006, Pages 1-45.

[130] Eur. Phys. J. 45 (2006), 343 hep-ex/0606028 hep-ex/0606029

[131] "Galactic cosmic radiation model and its applications" Advances in Space Research Volume: 17, Issue: 2, 1996, pp. (2)7-(2)17 Badhwar, G. D.; O'Neill, P. M.

[132] "Primary spectrum to 1-TeV and beyond" T.K. Gaisser, T. Stanev (Bartol Research Inst.) , M. Honda (Tokyo U., ICRR), P. Lipari (Rome U. & INFN, Rome) . Aug 2001. 4pp. Prepared for 27th International Cosmic Ray Conference (ICRC 2001), Hamburg, Germany, 7-15 Aug 2001. Published in Hamburg 2001, Cosmic ray 1643-1646.

[133] "Atmospheric Neutrino Flux Calculation with FLUKA: update and first results on prompt contribution" G. Battistoni, A. Bruno, F. Cafagna, P. Desiati, J.C. Diaz-Velez, A. Ferrari, T. Montaruli, P. R. Sala, A. Tamburro 29th International Cosmic Ray Conference Pune (2005) 00, 101-106.

[134] G.D. Badhwar and P.M. O'Neill, NASA Johnson Space Center (Houston) private communication and Adv. Space. Res. Vol. 17 no.2 (1996) (2)7.

[135] W.R. Webber, R.L. Golden & S.A. Stephens, Proc. 20th Int. Cosmic Ray Conf. (Moscow) vol.. 1 (1987) 325.

[136] T.K. Gaisser, in Proceedings of Neutrino 98, Takayama, Japan, hep-ph/9811314; and hep-ph/9811315 (1998).

[137] E.S. Seo et al., Ap. J. 378 (1991) 763.

[138] O.C. Allkofer, O.C. Karstensen and W.D. Dau, Phys. Lett. B425 (1971) 28.

[139] B.C. Rastin, J. Phys. G10 (1984) 1629.

[140] R. Bellotti et al., Phys. Rev. D53 (1996) 35.

[141] M.P. De Pascale et al., J. Geophys. Res. 98 (1993) 3501.

[142] M. Boezio et al., Phys. Rev. D62 (2000) 032007; J. Kremer et al., Phys. Rev. Lett. 83 (1999) 4241.

[143] M. Motoki et al., Astropart. Phys. 19 (2003) 113.

[144] W. Menn et al., Proc. 25th Int. Cosmic Ray Conf. (Durban) vol. 3 (1997) 409.

[145] M. Boezio et al., Astrophys. J. 518 (1999) 457.

[146] M. Boezio et al., Astropart. Phys. 19 (2003) 583.

[147] R. Bellotti et al., Phys. Rev. D60 (1999) 052002.

[148] J. Alcaraz et al., Phys. Lett. B472 (2000) 215-226 and Phys. Lett. B490 (2000) 27.

[149] T. Sanuki et al., Astrophys. J. 545 (2000) 1135.

[150] J. Alcaraz et al., Phys. Lett. B494 (2000) 193.

[151] K. Abe et al., Phys. Lett. B564 (2003) 8.

[152] Engelmann et al., Astr. 148 (1985) 12.

[153] D. Muller et al., Ap. J. 374 (1991) 356 .

[154] K. Asakimori et al., Ap. J. 502 (1998) 278; M.G. Ryan et al., Phys. Rev. Lett. 28 (1972) 985.

[155] A.V. Apanasenko et al., Astropart. Phys. 16 (2001) 13; M. Furukawa et al., Proc. 28th Int. Cosmic Ray Conf. Vol. 4 (2003) 1837.

[156] I.P. Ivanenko, et al., Proc. 23rd Int. Cosmic Ray Conf. (Calgary) vol. 2 (1993) 17.

[157] Y. Kawamura et al., Phys. Rev. D40 (1989) 729.

[158] T.K. Gaisser et al., Proc 27th Int. Cosmic Ray Conf. (2001) 643-1646.

[159] S. Haino et al., astro-ph/0403704 (2004). Submitted to Astropart. Phys.

[160] H.S. Ahn et al., Proc. 28th Int. Cosmic Ray Conf. vol. 4 (2003) 1833.

[161] G. Barr, talk at Neutrino 2004 Conference (2004).

[162] M. Aglietta et al., Astroparticle Physics vol 21 n.3 (2004) 223-240.

[163] T. Montaruli, Rapporteur talk at the 28th Int. Cosmic Ray Conf. (Tsukuba, 2003).

[164] G. Battistoni et al., Astrop.Phys. 19, 269, (2003). Erratum-ibid.19, 291-294 (2003). e-Print Archive: hepph/ 0207035. G. Battistoni et al., High Energy Extension Of The Fluka Atmospheric Neutrino Flux, 28lnm ICRC, Tsukuba, Japan (2003), 1399-1402.

[165] V. Agrawal et al., Phys. Rev. D, 53, 1314, (1996).

[166] T.K. Gaisser et al., "Primary spectrum to 1 TeV and beyond" , 27th ICRC, Hamburg (2001), OG 1.01.

[167] T. Montaruli, Report On The HE Phenomena Sessions He 2, He 3.2 - 3.4: Neutrinos And Muons. Interactions, Particle Physics Aspects, Astroparticle Physics And Cosmology. Rapporteur Papers of 28th ICRC Tsukuba, Japan, 135-160 (2003). e-Print Archive: hep-ph/0311289.

[168] www.euradnews.org/euradnews/newsletter11/pages/report/nl11_report_Dosmax.htm

[169] MSIS-E-00 Atmosphere Model. Available from:
$http://uap-www.nrl.navy.mil/models\_web/msis/msis\_home.htm$
$http://nssdc.gsfc.nasa.gov/space/model/models/msis.html$
$http://nssdc.gsfc.nasa.gov/space/model/models\_home.html$

[170] Labitzke et al., 1985

[171] http://swdcwww.kugi.kyoto-u.ac.jp/igrf/index.html

[172] S. Roesler, CERN, private communication.

[173] "The influence of the geomagnetic field and of the uncertainties in the primary spectrum on the development of the muon flux in the atmosphere" P. Hansen, T.K. Gaisser, T. Stanev, S.J. Sciutto E-Print ArXiv:astro-ph/0411634v1, 23 Nov 2004.

[174] A. Fasso', A. Ferrari, P.R. Sala, invited talk in the Proceedings of the MonteCarlo 2000 Conference, Lisbon, October 23-26 2000, A. Kling, F. Barao, M. Nakagawa, L. Tavora, P. Vaz eds., Springer-Verlag Berlin;
A. Fasso', A. Ferrari, J. Ranft, P.R. Sala, FLUKA: Status and Prospective for Hadronic Applications, invited talk in the Proceedings of the MonteCarlo 2000 Conference, Lisbon, October 23-26 2000, A. Kling, F. Barao, M. Nakagawa, L. Tavora, P. Vaz eds., Springer-Verlag Berlin, p. 955-960 (2001).

[175] F. Ballarini et al., talk presented at COSPAR2002, Houston, USA (2002), proceedings.

[176] S. Roesler et al., Radiat. Prot. Dosim, 98 (2002) 367.

[177] G. Battistoni et al., Astropart. Phys. 12 (2000) 315 and Astropart. Phys. 19 (2003) 269.

[178] G. Battistoni et al., Astropart. Phys. 17 (2002) 477, also hep-ph/0107241.

[179] http://www.fluka.org/

[180] G. Barr et al., Phys. Rev. D39 (1989) 3532; V. Agrawal, T.K. Gaisser, P. Lipari and T. Stanev, Phys. Rev. D53 (1996) 1314.

[181] G.D. Badhwar and P.M. O'Neill, Adv. Space Res. Vol.17, No. 2 (1996) 7.

[182] http://ulysses.uchicago.edu/NeutronMonitor/Misc/neutron2.html

[183] http://nssdc.gsfc.nasa.gov/space/model/models/igrf.html

[184] http://spidr.ngdc.noaa.gov/spidr/

[185] H. Debrunner et al., Geopyhs. Res. 93 (1988) 7206; J. Steinacker et al., Astron. Astrophys. 224 (1989) 259.

[186] K. R. Pyle et al., Astrophys. J. 282 (1984) L107.

[187] L. J. Gleeson and W. I. Axford, Astroph. J. Lett. 149 (1967) 115.

[188] Kahler, S.W., E.W. Cliver, et al., Proc. 20th Int. Cosmic Ray Conf. Moscow, 3, 121, 1987.

[189] Kahler, S.W., E. Hildner, M.A. Van Hollebeke, Solar Phys., 57, 429, 1978.

[190] Kahler, S.W., N.R. Sheeley et al., J. Geophys. Res., 89, 9683, 1984.

[191] Reames, D.V., and Ng C. K., Astrophys. J., 504, 1002, 1998.

[192] Pallavicini, R., S. Serio, and G.S. Vaiata, Astrophys. J., 216, 108, 1977.

[193] Sheeley, N.R., et al., Solar Phys.,45, 377, 1975.

[194] Caballero-Lopez, R. A., and H. Moraal (2004), Limitations of the force field equation to describe cosmic ray modulation, J. Geophys. Res., 109, A01101, doi:10.1029/2003JA010098.